SYNTHESIS AND CHARACTERIZATION OF REDUCED GRAPHENE OXIDE / TIO_2 NANOCOMPOSITES AS HIGH PERFORMANCE PHOTOCATALYST

BETTY CHANG YEA SZE

DISSERTATION SUBMITTED IN FULFILLMENT OF
THE REQUIREMENT FOR THE DEGREE OF
MASTER OF SCIENCE

DEPARTMENT OF PHYSICS
FACULTY OF SCIENCE
UNIVERSITY OF MALAYA
KUALA LUMPUR

2013

UNIVERSITI MALAYA

ORIGINAL LITERARY WORK DECLARATION

Name of Candidate: **BETTY CHANG YEA SZE** (I.C/Passport No: **871020-52-5634**)

Registration/Matric No: **SGR100083**

Name of Degree: **Master of Science (Dissertation)**

Title of Project ~~Paper/Research Report/~~Dissertation/~~Thesis~~ (“this Work”):

SYNTHESIS AND CHARACTERIZATION OF REDUCED GRAPHENE OXIDE / TIO_2 NANOCOMPOSITES AS HIGH PERFORMANCE PHOTOCATALYST

Field of Study: **Low Dimensional Materials**

I do solemnly and sincerely declare that:

(1) I am the sole author/writer of this Work;
(2) This Work is original;
(3) Any use of any work in which copyright exists was done by way of fair dealing and for permitted purposes and any excerpt or extract from, or reference to or reproduction of any copyright work has been disclosed expressly and sufficiently and the title of the Work and its authorship have been acknowledged in this Work;
(4) I do not have any actual knowledge nor do I ought reasonably to know that the making of this work constitutes an infringement of any copyright work;
(5) I hereby assign all and every rights in the copyright to this Work to the University of Malaya (“UM”), who henceforth shall be owner of the copyright in this Work and that any reproduction or use in any form or by any means whatsoever is prohibited without the written consent of UM having been first had and obtained;
(6) I am fully aware that if in the course of making this Work I have infringed any copyright whether intentionally or otherwise, I may be subject to legal action or any other action as may be determined by UM.

Candidate’s Signature: Date: 22 July 2013

Subscribed and solemnly declared before,

Witness’s Signature: Date: 22 July 2013

Name:
Designation:

ABSTRACT

A simple single stage approach, based on the hydrothermal technique, has been introduced to synthesize reduced graphene oxide-titanium dioxide (RGO/TiO_2) nanocomposites. The titanium dioxide (TiO_2) nanoparticles are formed at the same time as the graphene oxide (GO) is reduced to graphene. The triethanolamine (TEA) used in the process has two roles. It acts as a reducing agent for the GO as well as capping agent allowing the formation of titanium dioxide nanoparticles with a narrow size distribution (~20 nm). Transmission Electron Microscopy (TEM) micrographs show that the nanoparticles are uniformly distributed on the reduced graphene oxide (RGO) nanosheet. Thermogravimetric Analysis (TGA) analysis shows the nanocomposites have an enhanced thermal stability over the original components. The potential application for this technology was demonstrated by the use of RGO/TiO_2 nanocomposites in the photodegradation of methylene blue (MB). A significant enhancement in the photodegradation rate of MB under natural solar light was observed with the as-prepared RGO/TiO_2, compared to the commercial P25 and pure TiO_2 synthesized using the same method. This is due to the excellent adsorptivity of dyes performed by RGO (~8 times more powerful) and also because of the reduced electron-hole pair recombination demonstrated by the as-prepared RGO/TiO_2. Besides, the nanocomposites exhibit high recyclability. Overall, this work could provide new insights into the fabrication of a TiO_2-carbon composite as high performance photocatalysts and facilitate their application in the environmental protection issues.

ABSTRAK

Pendekatan peringkat tunggal dan mudah berdasarkan teknik hidroterma telah diperkenalkan untuk mensintesis graphene-titanium dioksida (RGO/TiO_2) komposit nano. Partikel nano titanium dioksida (TiO_2) terbentuk secara serentak dengan proses penurunan graphene oksida (GO) kepada graphene. Trietanolamina memainkan dua peranan dalam proses ini, iaitu bertindak sebagai agen penurunan bagi GO serta ejen pengehad yang membenarkan pembentukan partikel nano titanium dioksida dengan taburan saiz yang kecil (~20 nm). Mikrograf elektron mikroskop transmisi (TEM) menunjukkan bahawa partikel nano yang terbentuk di atas lapisan graphene menunjukkan sebaran yang seragam. Analisis termogravimetri (TGA) menunjukkan bahawa komposit nano ini mempunyai kestabilan terma yang lebih tinggi berbanding dengan komponen asalnya. Aplikasi bagi teknologi ini ialah penggunaan komposit nano RGO/TiO_2 dalam degradasi metilena biru (MB) di bawah sinaran matahari. Peningkatan ketara dalam kadar degradasi MB di bawah cahaya matahari telah dikesan dengan menggunakan RGO/TiO_2 yang disediakan, berbanding dengan titanium oksida komersial (P25) dan TiO_2 tulen yang disintesis menggunakan kaedah yang sama. Ini disebabkan penyerapan tinggi pewarna (~8 kali lebih kuat) oleh RGO, di samping pengurangan penggabungan semula pasangan elektron-lohong yang ditunjukkan daripada RGO/TiO_2 yang disediakan. Selain itu, RGO/TiO_2 juga mempunyai potensi yang tinggi untuk dikitar semula. Secara keseluruhannya, penyelidikan ini boleh memberi pemahaman baru dalam penyediaan komposit TiO_2-karbon sebagai fotomangkin berprestasi tinggi dan membuka peluang untuk mengaplikasikan teknologi ini dalam isu-isu perlindungan alam sekitar.

ACKNOWLEDGEMENT

Apart from the efforts of myself, the success of any project depends largely on the encouragement and guidelines of many others. I take this opportunity to express my gratitude to the people who have been instrumental in the successful completion of this project. I would like to show my greatest appreciation to Dr. Huang Nay Ming. I can't say thank you enough for his tremendous support and help. I feel motivated and encouraged every time I have a discussion with him. To me, he is more than a supervisor but also as a friend who is concerned of my personal well-being. Without his encouragement and guidance, I would not have reached this far and this project would not have materialized.

Besides that, I would like to extend my thanks to Prof. Datin Dr. Saadah Binti Abdul Rahman, the leader of Low Dimensional Materials Research Centre (LDMRC) for her encouragement and guidance throughout the course of study. Also, I want to gratefully acknowledge Dr. Lim Hong Ngee (UPM) for her kind advice and motivation.

Deepest gratitude is also due to the members of LDMRC, especially Mr. Mohamad Aruf and Mdm. Norlela for their valuable assistance in the project work. I would also like to express my sincere thanks to all my graduate friends, especially my group members, Dr. Vijay Kumar Shankarayya Wadi, Mr. An’ Amt Mohd Nor, Miss Marlinda Abdul Rahman, Mdm. Norazriena Yusoff, Mr. Gregory Thien Soon How, and Miss Nor Ily Syuhada for sharing the literature and invaluable assistance.

Moreover, I would also like to convey thanks to the High Impact Research Grant (UM.C/625/1/HIR/030) from the University of Malaya, the High Impact Research Grant (UM.C/625/1/HIR/MOHE/05) from the Ministry of Higher Education Malaysia, University of Malaya Research Grant (RG096-10AFR) and the Postgraduate Research Grant (UM.C/241/9) from the University of Malaya for providing the financial means and laboratory facilities. Apart from that, I am also grateful to The Bright Sparks Unit of University of Malaya for providing me with the research incentives.

Finally, I am forever indebted to my beloved parents, Mr. Chang Iue Shi and Mdm. Tang Kien Kuin, and also my families especially, Mdm. Ngoi Ai Sing, Mr. Joseph Kong Wei Hui, Mdm. Audrey Chang Yea Huey, Miss Flora Chang Yea Ning, and Miss Daphne Chang Yea Chen for their understanding, endless patience and encouragement when it was most required. I would also wish to avail myself of this opportunity, to express a sense of love and gratitude to my best friends especially, Miss Jennie Ting Yienn, Mr. Roy Ling How Gin, Mr. Ngu Leong Cheng, and Miss Elaine Cheam Yee Ping for their manual support, understanding, strength, help and for everything.

LIST OF PUBLICATIONS

1. **Chang, B. Y. S.**, Huang, N. M., An'amt, M. N., Marlinda, A. R., Norazriena Y., Muhamad M. R., et al. (2012). Facile hydrothermal preparation of titanium dioxide decorated reduced graphene oxide nanocomposite. *International Journal of Nanomedicine*, *7*(1), 3379-3387.

2. Marlinda, A. R., Huang, N. M., Muhamad, M. R., An'amt, M. N., **Chang, B. Y. S.**, Yusoff, N., et al. (2012). Highly efficient preparation of ZnO nanorods decorated reduced graphene oxide nanocomposites. *Materials Letters*, *80*(0), 9-12.

TABLE OF CONTENTS

LIST OF FIGURES

LIST OF TABLES

LIST OF ABBREVIATIONS

RGO/TiO_2	reduced graphene oxide-titanium dioxide nanocomposites
TiO_2	titanium dioxide
GO	graphene oxide
TEA	triethanolamine
TEM	Transmission Electron Microscopy
RGO	reduced graphene oxide
TGA	Thermogravimetric Analysis
MB	methylene blue
CNT	carbon nanotubes
MNT	molecular nanotechnology
nm	nanometers
TCS	TiO_2 clear sol
TTIP	titanium isopropoxide
HOPG	highly oriented pyrolytic graphite
CVD	chemical vapor deposition
SiC	silicon carbide
CMOS	complementary metal-oxide-semiconductor
DMF	*N*,*N*-dimethylformamide
NMP	*N*-methyl-pyrrolidone
ZnO	Zinc Oxide
NiO	Nickel Oxide
VB	valence band
CB	conduction band

HF	hydrogen fluoride
RGO	reduced graphene oxide
H_2SO_4	sulfuric acid
H_3PO_4	phosphoric acid
H_2O_2	hydrogen peroxide
UV-Vis	Ultraviolet-Visible
XPS	X-ray Photoelectron Spectroscopy
PL	Photoluminescence
XRD	X-Ray Diffraction
TGA	Thermogravimetric Analysis
CV	Cyclic Voltammetry
SEM	Scanning Electron Microscopy
FESEM	Field Emission Scanning Electron Microscopy
FE	Field Emission
NIR	near-infrared
EM	electromagnetic
CCD	charge-coupled device
UHV	ultra-high vacuum
RSF	relative sensitivity factor
UHV	Ultra-high vacuum
CMA	Cylindrical Mirror Analyzer
HRTEM	High Resolution Transmission Electron Microscopy
GCE	glassy carbon electrode
FWHM	Full width at half maximum

CHAPTER 1 : INTRODUCTION

1.1 Background of Research

The term "nanotechnology" has evolved over the years via terminology drift to mean "anything smaller than microtechnology," such as nano powders, and other things that are nanoscale in size. Nanotechnology basically refers to the engineering of functional systems at the molecular scale. This evolved version of the term is more properly labeled "nanoscale bulk technology," while the original meaning is now more properly labeled "molecular nanotechnology" (MNT), or "nanoscale engineering," or "molecular mechanics," or "molecular machine systems," or "molecular manufacturing." In 2003, Dr. K. Eric Drexler, the Chairman of the Foresight Institute has suggested an alternate term to represent the original meaning of nanotechnology, namely zettatechnology.

Development of nanotechnology was encouraged by refinement of tools to view the nanoworld, such as more sophisticated electron microscopy and scanning tunneling microscopy. The ability to see nano-sized materials has opened up a world of possibilities in a variety of industries and scientific endeavors. As nanotechnology is a set of techniques which allows manipulation of properties at a very small scale, it can be applied into various areas namely, drug delivery, fabrics making, synthesis of nanomaterials, and etcetera.

Over the past decades, nanomaterials developed by the advancement in nanotechnology have been the subject of enormous interest. Due to their extremely small feature size, nanomaterials have the potential for wide-ranging industrial, biomedical and electronic applications. As a result of recent improvement in technologies to see and manipulate these materials, the field of nanomaterials has attracted a huge amount of funding from the government and private enterprises. In addition, academic researchers within the field have also formed many collaborations and partnerships to excel into this area.

Nanomaterials can be composed of metals, ceramics, composite materials, or polymer materials. Nanomaterials are defined by their characteristic of having a very small feature size in the range of 1-100 nanometers (nm). The unit of nanometer derives its prefix nano from a Greek word meaning dwarf or extremely small. The nanoworld lies midway between the scale of atomic and quantum phenomena, and the scale of bulk materials. At nanoscale level, some material properties are affected by the laws of atomic physics, and thus behaving differently from the traditional bulk materials.

Nanomaterials are a bridge between bulk materials and atomic or molecular structures. A bulk material possesses constant physical properties regardless of its size but at the nanoscale level, size-dependent properties are often observed. As the size of the material approaches the nanoscale and as the percentage of atoms at the surface of a material becomes significant, the properties of the material are altered too. For bulk materials larger than one micrometer, the percentage of atoms at the surface is insignificant in relation to the number of atoms in bulk material. The interesting and sometimes unexpected properties of nanomaterials are therefore mainly due to the large surface area of the material, which dominates the contributions made by the small bulk of the material. These size-dependent properties include the following; quantum confinement in semiconductor particles, surface plasmon resonance in some metal particles, and superparamagnetism in magnetic materials.

One of the most important nanomaterials is the nanocomposites. A nanocomposite is a multiphase solid material in which one of the phases has one, two or three dimensions of less than 100 nanometers (nm). Not only that, a nanocomposite can also be classified as structures having nanoscale repeat distances between the different phases that make up the material. This definition includes colloids, gels, porous media, and copolymers, but it is more commonly refers to solid combination of a bulk matrix and nano-dimensional phase(s) differing in properties due to dissimilarities in terms of structure and chemistry. The mechanical, thermal, electrical, optical, catalytic, and electrochemical properties of the nanocomposites often differ markedly from that of the component materials. Basically, the reason why nanocomposites are attracting enormous interest is because they demonstrate combination of properties from the individual components. This research work focuses on the synthesis of graphene/titanium dioxide nanocomposites and hence it is essential to look into the properties of graphene and titanium dioxide respectively.

1.1.1 Background of Graphene and Titanium Dioxide

Graphene is a single layer carbon atoms arranged in a closely packed honeycomb of two-dimensional crystalline lattice. It is first discovered in 2004 by K. S. Novoselov and A. K. Geim (Novoselov et al., 2004). Since then, graphene has been investigated extensively due to its unique properties in terms of physical, chemical and mechanical properties (Aleiner & Efetov, 2006; Jannik et al., 2007; Novoselov et al., 2005; Schedin et al., 2007; Y. Zhang, Tan, Stormer, & Kim, 2005). Its electron is in high mobility and the charge carriers in graphene crystals mimic relativistic particles with no rest mass which is eventually described as massless Dirac fermions. This makes graphene a promising candidature for future electronic materials, sensors, composites, solar cell, gas storage media and supercapasitors.

There are several methods to synthesize graphene but in this case, chemical method was chosen. Chemical exfoliation from bulk graphite, is suggested to be a more effective way to produce large quantity but low cost graphene. This method basically involves the oxidation of graphite which eventually produced graphite oxide. The graphite oxide was then exfoliated to form graphene oxide and lastly underwent reduction to obtain graphene.

Titanium dioxide, TiO_2 which is also called Titania is a well-known functional material which can be applied as pigments, cosmetics, photocatalyst, sensor material, and electrode of photovoltaic cell (X. Chen & Mao, 2007). It is widely used in industrial applications due to its nontoxicity, low cost, and chemical stability (Fox & Dulay, 1993; Hoffmann, Martin, Choi, & Bahnemann, 1995). TiO_2 has been shown to be effective in the destruction of micro-organisms such as bacteria and viruses, the photosplitting of water to yield hydrogen gas, the fixation of nitrogen, the cleanup of oil spills, and the control of odours which makes it a promising candidate to be applied as environmentally benign photocatalyst.

About 15% of the total world production of dyes is lost during the dyeing process and released together in the textile effluents (Lachheb et al., 2002). The release of the coloured waste waters into the ecosystem leads to non-aesthetic pollution, eutrophication, and perturbations in the aquatic life. Photocatalysis appears as an emerging destructive technology to effectively mineralize the organic pollutants. It has been reported that carbon nanosheets/TiO_2 nanocomposites which are formed by simple reassembling of delaminated GO layers with TiO_2 clear sol (TCS), exhibit combined properties of carbon (adsorption) and TiO_2 (photoactivity) (Y.-J. Liu, Wang, Aizawa, Peng, & Hirotsu, 2009). Therefore, the combination of TiO_2 and graphene is promising to simultaneously exhibit excellent adsorptivity, transparency, conductivity, and controllability, which ultimately facilitate effective photodegradation of pollutants.

1.2 Research Problems and Motivations

The presence of the metal oxide particles like TiO_2 (Paek, Yoo, & Honma, 2008; Shen et al., 2010; J. F. Shen et al., 2011) often results in the changes in the Van der

Waals interactions in graphene, which eventually leads to the restacking of the graphene sheets. Hence, it is of great importance to develop a convenient and effective processing method for fabrication of graphene nanocomposites which coherently prevent the restacking of the graphene sheets. Recently, graphene-TiO_2 nanocomposites have been synthesized using technologies such as atomic layer deposition (Meng, Geng, Liu, Li, & Sun, 2011) and electron beam irradiation (H. J. Zhang et al., 2011). Although it is successful, these methods are probably not commercially viable. Other reported problems in the formation of graphene nanocomposites is the lack of discrete nanocrystalline TiO_2 particles before calcinations steps (Guo et al., 2011) and the agglomeration of the TiO_2 particles (Williams, Seger, & Kamat, 2008; H. Zhang et al., 2010).

It is also essential to produce TiO_2-C composite possessing photocatalytic activity well beyond commercial P25 with controllability and reproducibility, which is potent in environment remediation. Liang et al reported that a TiO_2-RGO composite prepared by growing TiO_2 nanocrystals on GO through hydrolysis followed by hydrothermal treatment exhibited high efficiency in the photocatalytic degradation of rhodamine B, and there existed strong interactions between TiO_2 and the graphene sheets (Liang, Wang, Casalongue, Chen, & Dai, 2010). On the other hand, Fan et al have studied the photocatalytic behaviors of the P25-RGO composites synthesized by different methods namely, chemical reduction using hydrazine, UV-assisted photoreduction, sol-gel methods, and hydrothermal method. The composite prepared by the hydrothermal method is the most efficient photocatalyst for the evolution of H_2. They added that the P25-RGO composite is more effective than bare P25 and P25-CNT composite for the evolution of H_2 (Fan, Lai, Zhang, & Wang, 2011).

1.3 Significance and Implications of the Research

In this work, one-step hydrothermal route for the preparation of graphene/TiO_2 nanocomposites using GO and titanium isopropoxide (TTIP) as starting materials with addition of TEA is reported. Hydrothermal technique was chosen because it is a “soft solution chemical processing” technique, which provides an easier way to control particle size, particle morphology, microstructures, phase composition and surface chemical properties. This one-step hydrothermal method is convenient, safe, and with the addition of TEA to the solution, the process provides a route to manufacture graphene-TiO_2 nanocomposites where the TiO_2 nanoparticles are discrete without any agglomeration of the particles. Moreover, the nanocomposites produced were tested for their photocatalytic activity and they displayed excellent photocatalysis to MB degradation under natural solar light irradiation. This is because they displayed excellent performance in all of the three important aspects namely, increased adsorptivity, expanded light absorption, and reduced electron-hole recombination. Hence, this study is able to provide insights into the means to control the properties of graphene-TiO_2 nanocomposites and thus promote their practical application in addressing various environmental issues.

The main objective of this work is to synthesize and characterize graphene/TiO_2 nanocomposites. The optimum parameter for the formation of graphene/TiO_2 nanocomposites needs to be identified. The study of the structure, morphology, and charge carrier dynamics of the as-prepared graphene/TiO_2 nanocomposites is also critical. Another focus of this research is to evaluate the efficiency of graphene/TiO_2 nanocomposites as photocatalyst.

1.4 Structure of Thesis

A brief overview of the chapters following the present one is given next.

Chapter 2: Literature Review

This chapter outlines the literature review of my research. It begins with the background of both graphene and TiO_2. The reasons why graphene and TiO_2 are both being selected as the candidate materials of this work are discussed. Apart from that, the unique properties demonstrated by graphene/TiO_2 nanocomposites in a specific application are presented. Lastly, this chapter ends with a proposed synthesis method to prepare graphene/TiO_2 nanocomposites.

Chapter 3: Experimental Details

In this chapter, sources of materials used are introduced. Next, the synthesis method of GO are presented. The preparation of RGO/TiO_2 nanocomposites through a one-step hydrothermal process is then described. Details of the various characterization methods involved are explained. Lastly, the steps included in the electrochemical and photocatalytic measurements of the synthesized RGO/TiO_2 are demonstrated.

Chapter 4: Results and Discussion

This chapter focuses on discussing the important results obtained from different analytical techniques being utilized which are basically being divided into three categories namely, structural, morphological and optical characterization. The effect of TEA and reaction temperature on the formation of RGO/TiO_2 nanocomposites is studied. A plausible mechanism of formation of RGO/TiO_2 is proposed. Moreover, the effect of hydrothermal temperature on the performance of RGO/TiO_2 as a detector for mercury ions and as a photocatalyst for MB photodegradation are investigated and compared.

Chapter 5: Conclusion and Future Works

This chapter concludes with a review on the objectives of this work. The objectives have been achieved and correlated with the results and discussions presented in the previous chapter. Furthermore, simple and brief description about this work is made, pointing out its influence in the scientific community. Suggestions for future research are given at the end of this chapter.

CHAPTER 2 : LITERATURE REVIEW

2.1 Introduction

In this chapter, research background and the purpose of this study will be introduced. It starts with the history of graphene, followed by its unique properties and synthesis methods. The special properties together with the synthesis methods of TiO_2 are presented next. Details of the photocatalytic degradation pathway of MB and how RGO/TiO_2 can help in the photodegradation are presented. The challenges in the fabrication of RGO/TiO_2 nanocomposites are addressed. Finally, a technique based on the hydrothermal process is proposed and the advantages provided by this hydrothermal process are explained as well.

2.2 Graphene

2.2.1 Properties of Graphene

Graphene is a monocrystalline graphitic films a few atoms thick and is stable under ambient conditions. Although Novoselov et al. was accredited for discovering graphene in 2004 when they extracted single-atomic-thick crystallites from highly oriented pyrolytic graphite (HOPG) by mechanical exfoliation method using ‘Scotch tape’, the term firstly appeared in 1987 by Mouras et al. referring to the single sheet of graphite within the graphite intercalation compounds (Mouras, Hamm, Djurado, & J.-C., 1987). It is also used to describe 1D carbon nanotubes (CNT) (Saito, Fujita, Dresselhaus, & Dresselhaus, 1992) and 3D epitaxial graphite (Forbeaux, Themlin, & Debever, 1998).

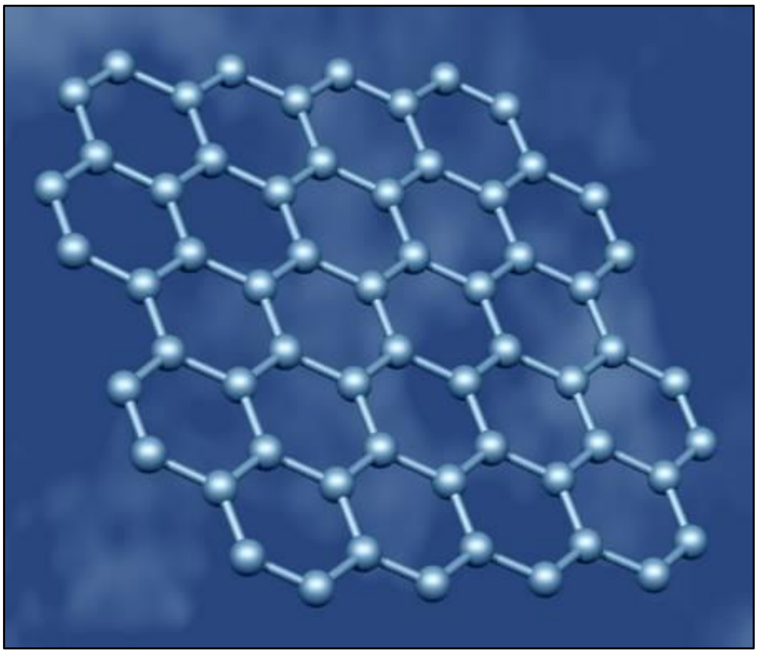

Figure 2.1: Graphene structure of single two-dimensional hexagonal sheet of carbon atoms (Andrei, 2011).

The concept of graphene can be dated back to 1947 when P.R. Wallace firstly theoretically explored it (Wallace, 1947). In 1984 Mele, E.J. et al. pointed out the emergent massless Dirac equation to describe the electrons around the Fermi level (DiVincenzo & Mele, 1984). Nevertheless, before Geim's group observed the single atomic layer graphene in 2004 (Novoselov et al., 2004), theorists such as Landau (1937) and Peierls (1935) argued that the true 2D crystal could not exist as it was thermodynamically unstable and the atomic monolayer tended to roll or fold in order to achieve the lowest potential energy state. Later research discovered that the reason why the atomic layer graphene could be observed was the existing of the intrinsic ripple (Fasolino, Los, & Katsnelson, 2007), which is believed to prevent graphene from rolling and to help suppress the thermal fluctuation.

The physical dimension of the films thickness ensures the electronic structure of the material is two-dimensional. Moreover, there is a small overlap between valence and conductance bands and graphene exhibits semimetal behavior. With the addition of a gate electrode, electrons and holes concentrations in the channel can be as high as 10^{13} cm^{-3} with room-temperature mobilities in the order of 10,000 $cm^2V^{-1}s^{-1}$. These results makes graphene an ideal candidate for the next generation of electronic devices (Novoselov et al., 2004). Apart from its unique electronic properties, the 2D planar structure material exhibits some other excellent attributes, for instance, the large theoretical specific surface area (McAllister et al., 2007) and the high transparency due to its one-atom thickness (Nair et al., 2008). In addition, the surface properties of graphene can be adjusted via chemical modification, which in turn facilitates its use in composite materials (Bekyarova et al., 2009; Williams et al., 2008). In addition, the mechanical and thermal properties of graphene are extremely good and so has potential application over a wide variety of uses such as composite materials, fuel cells, batteries, chemical detectors and solar cells (Balandin et al., 2008; Ishigami, Chen, Cullen, Fuhrer, & Williams, 2007; Konatham & Striolo, 2008; Meyer et al., 2007; Z. H. Ni et al., 2007; Sykes, 2009).

2.2.2 Synthesis Methods of Graphene

The main synthesis techniques of graphene can be categorized into four routes namely, (i) mechanical peeling; (ii) substrate-based methods, e.g. epitaxial growth and chemical vapor deposition (CVD); (iii) direct exfoliation of graphite in selected solvents; and (iv) solution-based reduction of graphene oxide.

Monolayer graphene was firstly obtained by micromechanical cleavage of bulk graphite in 2004 (Novoselov et al., 2004). It is also known as the ‘Scotch tape’ or peel-off method. After fine-tuning, this method yielded high-quality graphene crystallites up to 100 µm in size, which is sufficient for an in-depth study of its properties. Researchers had also attempted repeated peeling of HOPG with adhesive tape until the thinnest flakes were obtained (Novoselov et al., 2004). Nonetheless, the mechanical methods are extremely tedious and capable only of a low throughput; in which it is only suitable for fundamental study in laboratory.

As one of the substrate-based methods, the epitaxial growth of graphene involved the heating of silicon carbide (SiC) in a vacuum to allow the uppermost silicon atoms to escape, leaving behind carbon atoms to reconstruct into hexagonal graphene (Berger et al., 2006). Another substrate-based method namely CVD can be used to obtain graphene through the saturation of carbon on the transition metal after exposure to a hydrocarbon gas at a high temperature (Eizenberg & Blakely, 1979; K. S. Kim et al., 2009; Reina et al., 2008; Sutter, Flege, & Sutter, 2008). Typically, nickel films are used together with methane gas. Upon cooling the substrate, the solubility of carbon in the transition metal decreased and a thin film of carbon precipitated from the surface. The main advantage of substrate-based methods is their high compatibility with the current complementary metal-oxide-semiconductor (CMOS) technology. Nonetheless, the graphene produced through this method usually consists of several layers and the overall quality depends highly on the type of substrate materials used (Berger et al., 2006; Forbeaux et al., 1998; Sutter et al., 2008). Moreover, the complexity of the processes, including the proper selection of catalytic surfaces, deposition of an insulating support on top of graphene and chemical removal of the primary metallic substrate, make the costs of production extremely high.

Apart from that, graphene can also be obtained via ultrasonication of natural graphite in several selected organic solvents, such as *N*,*N*-dimethylformamide (DMF) and *N*-methyl-pyrrolidone (NMP) (Hernandez et al., 2008). It was proposed that the energy required to exfoliate graphene was balanced by the solvent-graphene interaction for solvents whose surface energies are compatible to that of graphene. The graphene dispersion can be prepared through repeated ultrasonication and centrifugation, but it is still a challenge to improve the monolayer yield and dispersion concentration.

Chemical exfoliation from bulk graphite on the other hand, is suggested to be a more effective way to produce large quantity but low cost graphene (D. Li, Muller, Gilje, Kaner, & Wallace, 2008; Stankovich et al., 2006; Stankovich et al., 2007). This method involves the oxidation of graphite and/or thermal expansion of graphite oxide/expandable graphite (Schniepp et al., 2006; Stankovich et al., 2007). Graphite oxide is a lamellar solid obtained from oxidation of neutral graphite sheets. Graphite oxide consists of graphite sheets which are covalently bonded to oxygen containing functional groups. Such oxygen-containing groups are like hydroxyl, epoxide and carboxyl groups. Hydroxy and epoxide groups bond to the basal planes while carboxyl groups bond to the edges of the graphite sheets. This makes graphite oxide platelets strongly hydrophilic and therefore can disperse well in water resulting in colloidal dispersions of negatively charged GO sheets. Negative charges originate on graphite oxide layers are due to the dissociation of the acidic groups present at the edges of graphite oxide sheets. Besides the electrons, the protons of the acidic groups are also exchangeable for other cations. As in the case of clays and other layered solids, the interlamellar space and the ion exchange property of graphite oxide has been utilized to synthesize graphite based materials such as graphite-polymer, nanoporous graphite, graphite–metal, graphite–metal oxide nanoparticle composites and battery electrode materials. The development of this new class of composite materials has been demonstrated to be able to enhance the properties and functionalities of the graphene produced especially in terms of electrical conductivity.

During the oxidation process, oxygen-containing functional groups are introduced to the natural graphite. This then reduces the interlayer interactions and thereby causing the d-spacing of graphite oxide to increase. This will eventually promote complete exfoliation of single graphite oxide layers in some specific conditions. Graphite oxide is then reacted with metal compounds to produce graphite-metal oxide composite. In order to modify their transport properties, chemical reduction of the graphite oxide will then take place by using reductants such as hydrazine and hydroquinone. The number of layers, quality and quantity of graphene produced is greatly affected by the reducing agents used. The selective production of high-quality graphene with a selected number of layers in a large quantity is the main challenge. The number of layers of graphene produced will determine its strength of conductivity.

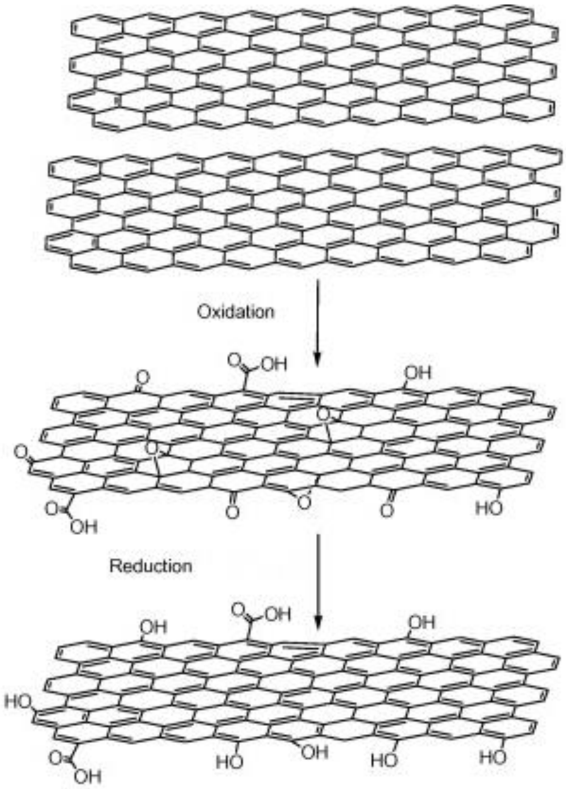

Figure 2.2: Chemical exfoliation pathway for the synthesis of graphene.

2.3 TiO_2

2.3.1 Properties of TiO_2

TiO_2 is traditionally used as white pigment. It is contained in a wide assortment of products, including paints, papers, inks, plastics, cosmetics, foods, pharmaceuticals, and etc. Nanocrystalline TiO_2 is a promising candidate for solar energy conversion applications such as photocatalysts, photochromics, and photovoltaics because of its unique optical and electrical properties (Lee et al., 2010). It is widely used in applications such as hydrogen production (Sato & White, 1980; W.S. Hong, J.H. Park, & Han, 2009), gas sensors (Chi-Hwan Han, Dae-Woong Hong, Sang-Do Han, Jihye Gwak, & Singh, 2007; Park et al., 2010), photocatalytic activities (L. Chen et al., 2009; Yazawa, Machida, Kubo, & Jin, 2009) and dye-sensitized solar cells (Dhas et al., 2011; Rahman, Tajabadi, Shooshtari, & Taghavinia, 2011) because of its relative high efficiency and high stability.

Figure 2.3: Image of TiO_2 powder (B. Mills, 2010).

The microbiocidal effects of TiO_2 photocatalytic reactions (Sikong, Kongreong, Kantachote, & Sutthisripok, 2010) clearly has pharmacological applications and TiO_2 photocatalytic reactions have been used to kill a wide spectrum of organisms including bacteria (Huang et al., 1999), viruses (Gerrity, H. Ryu, J. Crittenden, & Abbaszadegan, 2008), fungi (Mitoraj et al., 2007), cancer cells (A. P. Zhang & Sun, 2004) and algal toxins (Srinivasan & Somasundaram, 2003). In addition, antibacterial activity against four common human pathogens namely *Escherichia coli***,** *Pseudomonas aeruginosa***,** *Klebsiellapneumoniae* and *Staphylococcus aureus* has also been demonstrated (Desai & Kowshik, 2009). In addition, the oxidizing power of TiO_2 when under irradiation of UV light in either water and oxygen rich environment means that irradiated TiO_2 can be used in waste processing because of its ability to decompose and/or oxidize most of organic and/or inorganic compounds (Q. Li et al., 2008; Trapalis et al., 2003). Interestingly, the high chemical stability and nontoxicity also makes TiO_2 biocompatible and is used in many cosmetic products and as an alternative material for improving antimicrobial properties. For example TiO_2 nanoparticles have been added to dental acrylic resins to improve the colour (Acosta-Torres et al., 2011).

TiO_2 is known to be the most promising candidate for the degradation of environmental contaminants due its high photocatalytic activity (Gaya & Abdullah, 2008; Ni, Leung, Leung, & Sumathy, 2007). Besides, its biological and chemical inertness, strong oxidizing power, cost effectiveness, and long term stability against photocorrosion and chemical corrosion further supports the widespread use of TiO_2 as environmental photocatalyst (Hoffmann et al., 1995). TiO_2 exists in three types of phase structures namely, anatase, rutile and brookite. Anatase, the metastable phase exhibits the greatest photocatalytic activity due to its low combination rate of photogenerated electrons and holes. In the past 30 years, various factors which influence the efficiency of organic photodegradation of TiO_2 have been reported. The main focus has been the physical properties of TiO_2, namely crystal phases, crystal facets, crystallinity, specific surface area, particle size, porosity, and morphology (Dong et al., 2007; Michio Inagaki, Nonaka, Tryba, & Morawski, 2006; Kominami, Murakami, Kato, Kera, & Ohtani, 2002; Ohno, Sarukawa, & Matsumura, 2002; Sclafani, Palmisano, & Schiavello, 1990; Serpone, Lawless, Khairutdinov, & Pelizzetti, 1995; Y. Xu et al., 2007). Nonetheless, it is often difficult to determine the exact contribution of each factor to the photoactivity of TiO_2. As an example, crystallinity and specific surface area normally appear as two conflicting intrinsic properties for TiO_2 nanoparticles (G. Liu et al., 2006). Having said that, anatase TiO_2 with high BET specific surface area, good crystallization and relative small crystallite size is favorable to improve the photocatalytic activity by creating more reactive sites on the surface of the photocatalyst.

2.3.2 Synthesis Methods of TiO_2

A number of methods have been used to prepare TiO_2 nanoparticles, such as chemical precipitation (Scolan & Sanchez, 1998), microemulsion-mediated hydrothermal (Wu et al., 1999), hydrothermal crystallization (Wu et al., 2002; S. Yang & Gao, 2005; H. Y. Zhu et al., 2005), and sol–gel (C.-C. Wang & Ying, 1999). Sol–gel is one of the most successful techniques to synthesize nano-sized metallic oxide materials with high photocatalytic activities. By tailoring the chemical structure of primary precursor and controlling the processing variables, nanocrystalline products with very high level of chemical purity can be obtained. In sol–gel processes, TiO_2 is usually prepared by hydrolysis and polycondensation reactions of titanium alkoxides, $Ti(OR)_n$ to form oxopolymers which are then transformed into an oxide network. Some of the chelating reagents such as diol, carboxylic acid, or diketonate compounds are added to control the hydrolysis process with the objective of obtaining homogeneous titanium oxide network (Wu et al., 2002). Condensation is usually accomplished by gelation and calcination. Condensation causes the constitute particles of the gel to come together, forming into a compact mass, thus building up the metal oxide crystal. Calcination, on the other hand, is especially essential for removing the organic molecules from the final products and completing the crystallization process. Nevertheless, high temperature calcination usually results in aggregation and/or phase transformation which eventually affects the microstructures as well as the properties of TiO_2 nanoparticles (Su, Hong, & Tseng, 2004).

The hydrothermal synthesis route represents an alternative to calcination for promoting crystallization at milder temperatures. Chemical reactions occur in an aqueous medium under heating and high pressure. Generally in hydrothermal synthesis, a reduced agglomeration of particles is achieved and crystallization can occur without extensive particle growth. Hydrothermal method is a ‘‘soft solution chemical processing’’ which provides an easy route to prepare a well-crystalline oxide under moderate reaction condition, for instance, low temperature and short reaction time (Pookmanee, Rujijanagul, Ananta, Heimann, & Phanichphant, 2004). Due to the potential to yield high-purity and homogeneous fine crystalline powders, hydrothermal process has gained considerable popularity in preparing ceramic samples with controlled particle size and morphology.

2.4 Graphene/TiO_2 Nanocomposites

2.4.1 Synthesis Methods of Graphene/TiO_2 Nanocomposites

The challenge, when developing convenient and effective processing technologies for the fabrication of graphene nanocomposites is the prevention of the restacking and/or agglomeration of the graphene sheets caused by the changes in the Van der Waals interactions due to the presence of the metal oxide particles like TiO_2 (Paek et al., 2008; Shen et al., 2010). Recently, graphene-TiO_2 nanocomposites have been synthesized using technologies such as atomic layer deposition (Meng et al., 2011) and electron beam irradiation (H. J. Zhang et al., 2011). Although successful, these methods are probably not commercially viable since the processes require six-step sequence with heat treatment at various temperatures (Meng et al., 2011) or pretreated graphene (H. J. Zhang et al., 2011) as a raw material. Furthermore, other reported techniques that use hazardous chemicals, such as hydrazine hydrate, create dangerous by-products such as hydrogen fluoride (HF) (Lambert et al., 2009). Other reported problems in the formation of graphene nanocomposites include the lack of discrete nanocrystalline TiO2 particles before calcination (Guo et al., 2011) and agglomeration of the TiO_2 particles (Williams et al., 2008; H. Zhang et al., 2010).

In this study, one-step hydrothermal route for the preparation of graphene/TiO_2 nanocomposites using GO and TTIP as starting materials with addition of TEA is demonstrated (Chang BYS et al., 2012). Hydrothermal technique was chosen because it is a “soft solution chemical processing” technique, which provides an easier way to control particle size, particle morphology, microstructures, phase composition and surface chemical properties by adjusting experimental parameters such as temperature, pressure, duration of process and pH value of solution (Byrappa & Yoshimura, 2001; Kolen'ko et al., 2004; Su et al., 2006).

Many papers have been published on the synthesis of crystalline TiO_2 nanoparticles using the hydrothermal route. In the water-based routes, additives are used to induce peptization (Grätzel, 2001; So, Park, Kim, & Moon, 1997; Su et al., 2006; J. Yang, Mei, & Ferreira, 2001) prior to hydrothermal treatment. This is done in order to control the particle size alternatively hydrothermal treatment is carried out at temperatures above 150 ℃ (Grätzel, 2001; O'Regan & Gratzel, 1991). This one-step hydrothermal method is convenient, safe, and with the addition of TEA to the solution, the process provides a route to manufacture graphene-TiO_2 nanocomposites where the TiO_2 nanoparticles are discrete with no agglomeration of the particles. Whilst others have also reported a single-step hydrothermal technique, it is not similar to the one used in this thesis. Shen et al (J. Shen et al., 2011) reported an “intrinsically pure process” as it utilizes only water and glucose. However, their prior-hydrothermal sample contained ammonium chloride, ethanol, glucose and ammonium hydroxide (J. Shen et al., 2011). In the method reported here, only TEA and ethanol were added. Other reported one-step hydrothermal processing studies used ultrasonication to obtain a well-dispersed suspension of GO and TiO_2. This step was omitted in the current work. In addition, the influence of the hydrothermal temperature on the crystallinity, size distribution, thermal stability, and electrochemical performance of reduced GO (RGO)/TiO_2 nanocomposites is reported too. To the best of my knowledge, the effect of TEA and reaction temperature on the formation of RGO/TiO_2 nanocomposites has not been previously reported and hence, contributes to the novelty of this research.

Herein, a facile one-step hydrothermal approach to synthesize RGO/TiO_2 nanocomposites has been demonstrated (Chang BYS et al., 2012). The TiO_2 nanoparticles appeared to be discrete with no agglomeration of the particles on the RGO sheet. Furthermore, the photocatalytic activity of the RGO/ TiO_2 nanocomposites synthesized at different hydrothermal temperature has also been studied. The experiments were carried out in MB solution under the irradiation of natural sunlight. It is found that the nanocomposites produced displayed excellent performance in all of the three important aspects, namely increased adsorptivity, expanded light absorption, and reduced electron-hole recombination hence, exhibit excellent photocatalysis to MB degradation under natural solar light irradiation. To the best of our knowledge, the photodegration of MB by RGO/TiO_2 using natural sunlight as the source of light and the effect of reaction temperature on the photocatalytic activity of RGO/TiO_2 nanocomposites have not been reported before. Thus, this is another novelty of the research.

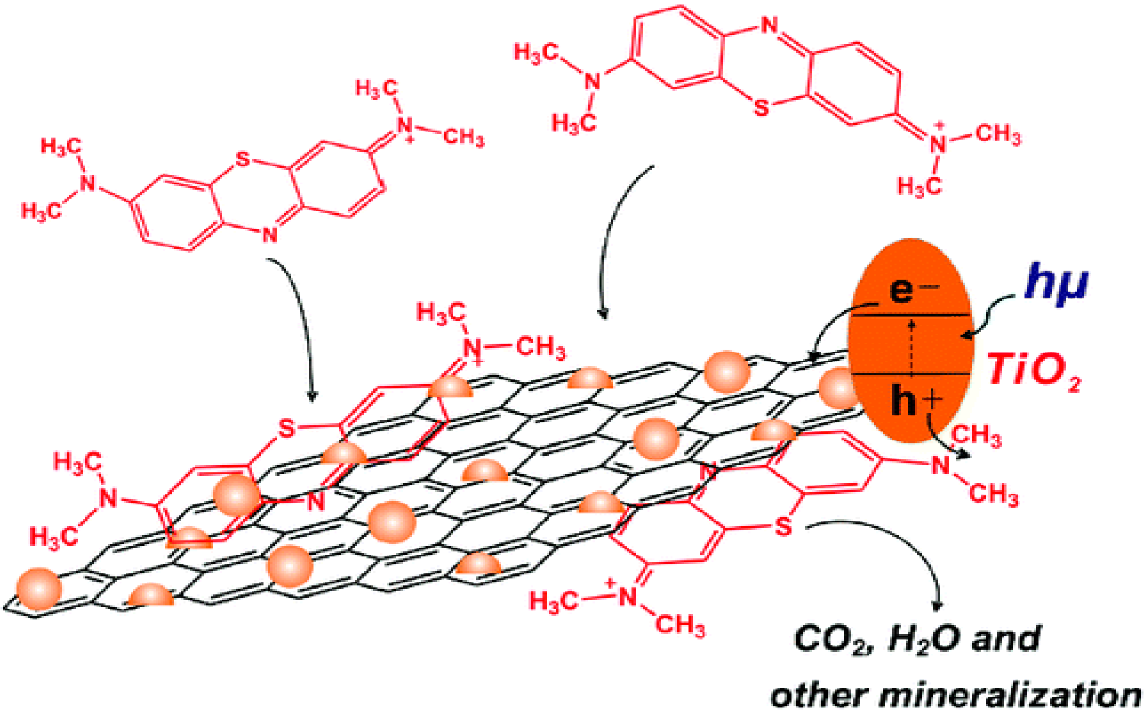

Figure 2.4: Photodegradation process of MB over Graphene/TiO_2 (H. Zhang et al., 2010).

2.4.2 Graphene/TiO_2 Nanocomposites as Photocatalyst

About 15% of the total world production of dyes is lost during the dying process and released together in the textile effluents (Lachheb et al., 2002). The release of the coloured waste waters into the ecosystem leads to non-aesthetic pollution, eutrophication, and perturbations in the aquatic life. Photocatalysis appears as an emerging destructive technology to effectively mineralize the organic pollutants. Photocatalysis potentially can be a good solution for many of the environmental challenges facing the modern world because it provides a simple way with the utilization of light to induce chemical transformations. Thus, photodegradation of organic pollutants has attracted massive attention during the past decades (Hoffmann et al., 1995). Semiconductor photocatalysts are particularly interesting due to their unique optical and electric properties in environmental applications, for instance, air purification, water disinfection, hazardous waste remediation, and water purification (Fujishima, Rao, & Tryk, 2000; F. B. Li & Li, 2002; F. B. Li, Li, & Hou, 2004; Linsebigler, Lu, & Yates, 1995; Tada, Yamamoto, & Ito, 1999).

Early investigations in photocatalysis were devoted to the study of semiconductors based on metal oxides, like Zinc Oxide (ZnO) (Muller & Steinbach, 1970) and Nickel Oxide (NiO) (Steinbach, 1969). Among various semiconductors, Titanium Dioxide (TiO_2) is known to be the most promising candidate for the degradation of environmental contaminants due its high photocatalytic activity (Gaya & Abdullah, 2008; M. Ni et al., 2007). The publication in 1971 of the work by Formenti et al. (Formenti, Juillet, Meriaudeau, & Teichner, 1971), followed one year later by A. Fujishima and K. Honda's (Fujishima & Honda, 1972) renowned article prompted a true revolution based on the extensive use of TiO_2 as a photocatalyst. The relatively high quantum yield and elevated stability of TiO_2 are the key reasons for the preponderance of this semiconductor, which has become a virtual synonym for photocatalyst.

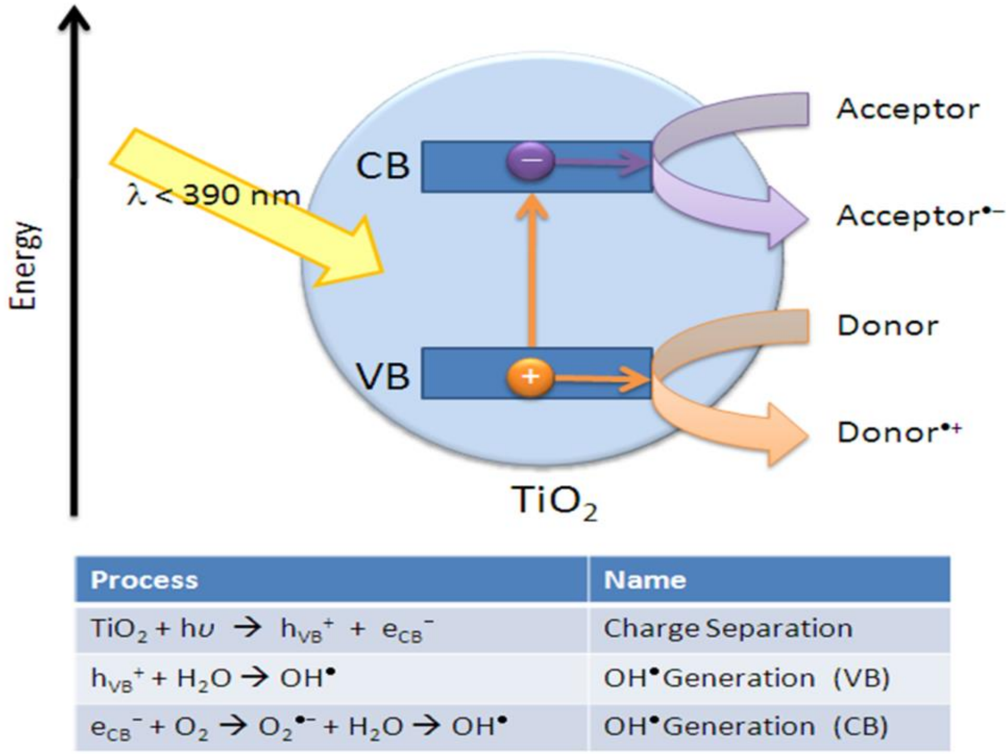

Process	Name
$TiO_2 + h\upsilon \rightarrow h_{VB}^+ + e_{CB}^-$	Charge Separation
$h_{VB}^+ + H_2O \rightarrow OH^\bullet$	$OH^\bullet$ Generation (VB)
$e_{CB}^- + O_2 \rightarrow O_2^{\bullet-} + H_2O \rightarrow OH^\bullet$	$OH^\bullet$ Generation (CB)

Figure 2.5: Pictorial diagram showing the main events of photocatalysis over TiO_2 (Seery, 2009).

The initial step of photocatalysis is the absorption of photons of wavelength adequate to match energy levels of the photoactive material. In the case of semiconductors like TiO_2, illumination induces electron promotion from the valence to the conduction band if the energy of the photons exceeds the band width (Carp, Huisman, & Reller, 2004; Fujishima et al., 2000; J.-M. Herrmann, 1999; Hoffmann et al., 1995; Linsebigler et al., 1995; A. Mills & Le Hunte, 1997). This process leaves an unoccupied state or electron hole in the valence band, which can be conveniently described as a particle in its own right. Most of these electron–hole pairs recombine, releasing the absorbed energy as light or, more frequently, as heat. However, a small percentage of these carriers migrate to the surface where they can be captured by adsorbed molecules to start the catalytic cycle (Carp et al., 2004; Fujishima et al., 2000;

J.-M. Herrmann, 1999; Hoffmann et al., 1995; Linsebigler et al., 1995; A. Mills & Le Hunte, 1997). A generic scheme of these processes can be seen in **Figure 2.5**. Conduction band electrons can reduce electron acceptors, like oxygen molecules or H^+. On the other hand, valence band holes are oxidants that are able to attack donor species such as organic molecules or OH^- groups.

Photoactivity is determined by the interplay between surface and electronic characteristics, and is often estimated by quantum yield. This parameter is defined as the ratio between the rate of photoinduced events and the flux of absorbed photon (Carp et al., 2004; Fujishima et al., 2000; J.-M. Herrmann, 1999; Hoffmann et al., 1995; Linsebigler et al., 1995; A. Mills & Le Hunte, 1997). Nonetheless, an accurate estimation of absorbed photons in real systems is often impossible to obtain as a result of extensive light scattering. Consequently, for practical reasons, many studies assume that all the radiation is absorbed and an alternative performance index, the photonic efficiency, is defined as the quotient between the rate of the photocatalytic events and the photon flux (Carp et al., 2004; Fujishima et al., 2000; J.-M. Herrmann, 1999; Hoffmann et al., 1995; Linsebigler et al., 1995; A. Mills & Le Hunte, 1997).

Heterogeneous photocatalysis appears to be a method which can simultaneously leading to the oxidation of the dye, together with the total mineralization of most of the organic pollutants (Helz, Zepp, & Crosby, 1994; J. M. Herrmann, 1999; Herrmann, Guillard, & Pichat, 1993; Legrini, Oliveros, & Braun, 1993; Ollis & Al-Ekabi, 1993; Schiavello, 1988; Serpone & Pelizzetti, 1989). The proposed photocatalytic degradation pathway of methylene blue by TiO_2 in water is shown below.

1. Absorption of efficient photons ($h\nu \geqslant E_G = 3.2$ eV) by titanium dioxide

$(TiO_2) + h\nu \rightarrow e^-_{CB} + h^+_{VB}$ (1)

2. Oxygen ionosorption (first step of oxygen reduction; oxygen's oxidation state changes from 0 to −1/2)

$(O2)_{ads} + e^-_{CB} \rightarrow O_2^{\bullet-}$ (2)

3. Neutralization of OH– groups by photoholes which produces OH◦ radicals

$(H_2O \Leftrightarrow H^+ + OH^-)_{ads} + h^+_{VB} \rightarrow H^+ + OH^{\bullet}$ (3)

4. Neutralization of $O_2^{\circ-}$ by protons

$O_2^{\circ-} + H^+ \rightarrow HO_2^{\circ}$ (4)

5. Transient hydrogen peroxide formation and dismutation of oxygen

$2HO_2^{\circ-} \rightarrow H_2O_2 + O_2$ (5)

6. Decomposition of H_2O_2 and second reduction of oxygen

$H_2O_2 + e^- \rightarrow OH^{\circ} + OH^-$ (6)

7. Oxidation of the organic reactant via successive attacks by OH• radicals

$R + OH^{\circ} \rightarrow R'^{\bullet} + H_2O$ (7)

8. Direct oxidation by reaction with holes

$R + h^+ \rightarrow R^{+\circ} \rightarrow$ degradation products (8)

As an example of the last process, holes can react directly with carboxylic acids generating CO_2

$RCOO^- + h^+ \rightarrow R^{\bullet} + CO_2$ (9)

Currently, TiO_2 is by far the most widely used photocatalyst because it comprises the best balance of properties among the known or assayed semiconductors. Nevertheless, it still presents some disadvantages such as limited activity and reduced sensitivity to sunlight. Hence, in the last few years significant effort has been devoted to the search for new materials that may overcome the limitations of TiO_2. One of the approaches is to combine graphene and TiO_2 to form graphene/TiO_2 nanocomposites. The integration of graphene with inorganic nanoparticles allows the properties of the nanocomposite to be engineered for specific applications as they are able to exhibit properties that are not found in the individual components (Kong, Geng, & Jung, 2009; Scheuermann, Rumi, Steurer, Bannwarth, & Mulhaupt, 2009; X. Yang et al., 2009; Yoo et al., 2009; Yuge et al., 2008; Y. Zhang et al., 2005; Zhao, Pei, Ren, Gao, & Cheng, 2010; J. Zhu, 2008).

Titanium dioxide (titania) is the most attractive photocatalyst, because it is nontoxic, chemically stable, and relatively cheap. The well-known drawback in the use of TiO_2 in the advanced oxidation photocatalytic process is the recombination of electron (e^-) and hole (h^+) pairs. Under UV irradiation, electron-hole pairs are formed in which electrons are excited from the valence band (VB) to the conduction band (CB) of TiO_2. These electron-hole pairs took part in the photocatalytic activity of TiO_2. Nonetheless, the photogenerated electron-hole pairs have a flash recombination time of 10^{-9} s, while the time for chemical interaction of TiO_2 with adsorbed pollutant is in the range of 10^{-8} – 10^{-3} s (Hoffmann et al., 1995; Woan, Pyrgiotakis, & Sigmund, 2009). The discrepancy of these two limits the efficiency of the photocatalysis.

The reported attempts to avoid the recombination of electron-hole pairs and extend the photoresponse into visible range, is based on the doping of titanium dioxide with noble metals, such as Pt (S. Kim, Hwang, & Choi, 2005), Au (Subramanian, Wolf, & Kamat, 2002), and Ag (Sobana, Muruganadham, & Swaminathan, 2006). Other efforts reported are, for example, Bi_2S_3/TiO_2 and CdS/TiO_2 heterojunction photocatalyst (Bessekhouad, Robert, & Weber, 2004). Some of the pairings that have been synthesized, for instance, titanium dioxide with CdS, causes environmental problems with the release of cadmium in solution. This approach also proved to be less suitable because it is very difficult to determine the exact concentration of the metal. Moreover, the interaction between the used metals and disassembly agent (pollutants) reduces photocatalytic efficiency.

Besides, preparing TiO_2-C composites is another endeavour made to enhance the photoactivity (Shanmugam, Gabashvili, Jacob, Yu, & Gedanken, 2006; L. Yang, Luo, Liu, & Cai, 2008; H. Yu, Quan, Chen, & Zhao, 2007). The TiO_2-C composites can be generally categorized into three types; TiO_2-mounted activated carbon, carbon-doped TiO_2, and carbon-coated TiO_2. Each of them gives good photocatalytic activity (M. Inagaki, Kojin, Tryba, & Toyoda, 2005; L. Yang et al., 2008). Nonetheless, there are several factors hindering further promotion of efficiency of the present TiO_2-C composites, for examples, the marked decrease of the adsorptivity during photodegradation, the weakening of light intensity arriving the catalysts' surface, and the lack of reproducibility due to the preparation and treatment variation (M. Inagaki et al., 2005; Woan et al., 2009). Hence, it is of great importance to obtain TiO_2-C composite possessing photocatalytic activity well beyond commercial pure P25 with controllability and reproducibility, which is potent in environment remediation. This objective can be achieved by combining titania and graphene nanosheets.

Graphene is a very attractive material for fabricating graphene containing inorganic composites due to its unique electronic property, high transparency, flexible structure, and large theoretical specific surface area. One of its many applications is the use of graphene in the preparation of highly photoactive composites materials based on titanium oxides. Graphene is the ideal nanostructure product to be paired with titanium dioxide, accentuating its capability to absorb as well as its photocatalytic activity. The electrons freed after the titanium dioxide activation are easily transported to the graphene nanosheets, greatly reducing the recombination of e^- and h^+, which then increases the process yield.

In the literature we can find some efforts to produce these composite materials. In 2008, Williams et al have showed that the photogenerated electrons from UV-irradiated TiO_2 can be transferred to graphene oxide (GO), reducing GO to RGO (Williams et al., 2008). The photogenerated elctrons could also be transported across the RGO to reduce Ag ions to Ag nanoparticle at a location distinct from the TiO_2 anchored site on RGO (Lightcap, Kosel, & Kamat, 2010). Moreover, Zhang et al have demonstrated that the TiO_2 (P25)-RGO composite acted as a highly efficient photocatalyst for the degradation of methylene blue. They further addressed that the carbon platform in P25-graphene composite plays crucial roles during the photodegradation of MB in three aspects; increase catalyst adsorptivity, extend light absorption, and suppress charge recombination (H. Zhang et al., 2010).

Nevertheless, a recent study by another group of Zhang et al pointed out that the TiO_2-RGO composite was in essence the same as the TiO_2-carbon (CNT, fullerenes, and activated carbon) composite materials on the enhancement of the photocatalytic performance in the gas-phase degradation of benzene (Y. H. Zhang, Tang, Fu, & Xu, 2010). Liang et al on the other hand, reported that a TiO_2-RGO composite prepared by growing TiO_2 nanocrystals on GO through hydrolysis followed by hydrothermal treatment exhibited high efficiency in the photocatalytic degradation of rhodamine B, and there existed strong interactions between TiO_2 and the graphene sheets (Liang et al., 2010). Fan et al have studied the photocatalytic behaviors of the P25-RGO composites synthesized by several different methods namely, chemical reduction using hydrazine, UV-assisted photoreduction, sol-gel methods, and hydrothermal method and reported that the composite prepared by the hydrothermal method is the most efficient photocatalyst for the evolution of H_2. They added that the P25-RGO composite is more effective than bare P25 and P25-CNT composite for the evolution of H_2 (Fan et al., 2011).

Therefore, the combination of TiO_2 and graphene is promising to simultaneously exhibit excellent adsorptivity, transparency, conductivity, and controllability, which ultimately facilitate effective photodegradation of pollutants.

CHAPTER 3 : EXPERIMENT DETAILS

3.1 Introduction

The chapter begins with the introduction of sources of materials used in this research. In addition, the step-by-step procedures involved in the synthesis of GO, and RGO/TiO_2 are described as well. The general characterization techniques utilized to study the structural, morphology, and optical properties of RGO/TiO_2 are subsequently briefly discussed. The procedures included in the study of the electrochemical and photocatalytic performances of RGO/TiO_2 are exhibited. The last part of this chapter presents the way dark adsorption and durability tests were carried out.

3.2 Experimental (Material Synthesis Process)

3.2.1 Raw Materials

Graphite 3061 and TTIP (99%) were purchased from Asbury Graphite Mills Inc (Asbury, NJ) and Acros Organics (Geel, Belgium), respectively; TEA and potassium permanganate ($KMnO_4$) were obtained from R&M Chemicals (Systerm, Malaysia). The other materials – sulfuric acid (H_2SO_4), phosphoric acid (H_3PO_4), hydrogen peroxide (H_2O_2), and ethanol – were purchased from Merck KGaA (Darmstadt, Germany). MB and P25 were obtained respectively from Systerm and Acros Organics. Unless otherwise specified, all the reagents and materials involved were used as received without further purification. Deionized water (resistivity $\geq$ 18MΩ) was used during the experimental process.

3.2.2 Synthesis of GO

GO was synthesized via the simplified Hummers method carried out at room temperature in which a 9:1 H_2SO_4:H_3PO_4 (360:40 mL) solution was prepared, into which 3 g of graphite was added (HN, NM, SS, I, & CH, 2011; Huang NM, 2011). $KMnO_4$ (18 g) was gradually added and the solution was left to oxidize for 3 days whilst being continuously stirred. After 3 days, the resulting solution was cooled to room temperature and poured onto ice (~400 mL) along with 27 mL of 30% H_2O_2. The solution was centrifuged (CR21GIII; Hitachi, Japan) and washed three times with 1 M hydrogen chloride and six times with water. The final solution, the GO dispersion, was light brown in colour. The concentration of this GO solution was then determined as below:

	1	**2**	**3**
Mass of petri dish (mg)	1270.20	1270.10	1270.22
Mass of petri dish + Mass of GO (mg)	1295.40	1295.10	1295.22
Mass of GO (mg)	25.20	25.00	25.00
Volume of GO (mL)	10.0	10.0	10.0
Concentration of GO (mg/mL)	2.52	2.50	2.50

Table 3.1: Calculation steps to determine the concentration of GO solution.

Hence, Concentration of GO = $\frac{2.52+2.50+2.50}{3}$

= **2.51 mg/mL**

Figure 3.1: Image of graphite 3061.

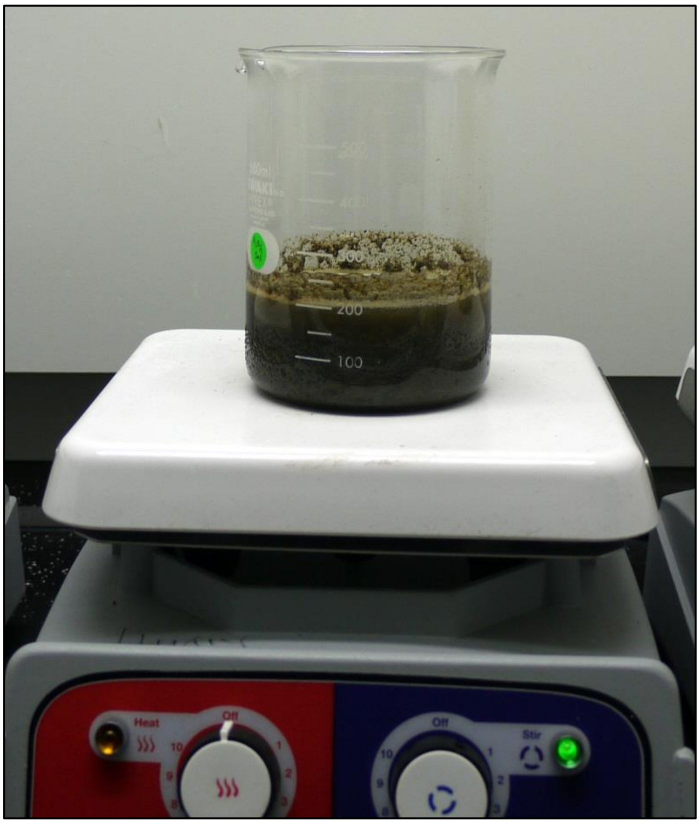

Figure 3.2: The reaction process of Simplified Hummers method.

Figure 3.3: Real image of Centrifuge CR21GIII; Hitachi, Japan.

Figure 3.4: Image of GO solution synthesized through Simplified Hummers method.

3.2.3 Synthesis of RGO/TiO_2

3.72 mL of TTIP was added into 3.32 mL of TEA in a 25 mL volumetric flask (Favorit, PLT Scientific Sdn. Bhd) producing a titanium(IV) ionic (Ti^{4+}) solution with a concentration of 0.50 M. In order to form the GO/TiO_2 solution, 10 mL of 1 mg/mL of GO solution was added into a water:ethanol mixture (1:14) mL with continuous stirring. 1 mg/mL of GO solution was obtained from the dilution of the 2.51 mg/mL GO based on the calculations shown below:

$$M_1V_1 = M_2V_2$$

$$(2.51\ \text{mg/mL})\ (V_1\ \text{mL}) = (1\ \text{mg/mL})\ (50.00\ \text{mL})$$

$$V_1 = 19.90\ \text{mL}$$

Thus, 19.90 mL of 2.51 mg/mL GO was added into 50 mL volumetric flask and topped up. Through this dilution method, 1 mg/mL GO was acquired. After that, 3 mL of Ti^{4+} solution was added and the mixture stirred for 24 hours at room temperature to obtain a homogeneous suspension. The mixture was placed in a custom made Teflon-lined autoclave and heated to 120 ℃ for 24 hours. Two other samples were prepared by an identical procedure except for the final autoclave reaction temperature (150 ℃ and 180 ℃). The samples were labeled as 120 RGO/TiO_2, 150 RGO/TiO_2, and 180 RGO/TiO_2, with the number signifying the reaction temperature. The black precipitates were washed three times with ethanol, centrifuged at 13,000 g for 10 minutes, and oven dried at 60 ℃. Pure TiO_2 samples were also prepared using the same procedure; these samples are denoted as 120 TiO_2, 150 TiO_2, and 180 TiO_2. RGO was also synthesized in the absence of titanium isopropoxide under the same conditions at 180 ℃.

Figure 3.5: Image of custom made Teflon-lined autoclave.

3.3 Characterization Methods

The bond structure and photocatalytic measurements were investigated using Ultraviolet-Visible (UV-Vis) spectroscopy with a scan rate of 240 nm/mm (Evolution 300; Thermo Fisher Scientific, Pittsburgh, PA). Micro-Raman spectroscopy was performed on a Renishaw inVia Raman microscope excited at 514 nm. X-ray Photoelectron Spectroscopy (XPS) measurement of the nanocomposite was performed by using synchrotron light at beamline no. 3.2 of Siam Photon Laboratory, Synchrotron Light Research Institute, Thailand. XPS was operated in the conditions of maximum photon energy 600 eV and kinetic energy step 0.1 eV. Photoluminescence (PL) curves were obtained by using Renishaw inVia PL microscope excited at 325 nm. The structure of the samples was investigated by X-Ray Diffraction (XRD) using Copper Kα radiation (λ= 1.5418 Å) at a scan rate of 0.02 degree s^{-1}. This was complemented by

TEM (CM12; Philips) operated at 100 kV, which allowed an image of the nanoparticles and graphene sheets to be acquired. The size distribution of the nanoparticles was then measured by ISolution, an image analysis software. The chemical stability was investigated using Thermogravimetric Analysis (TGA) (Q500; TA Instruments, New Castle, DE). The electrochemical performance was assessed using three-electrode Cyclic Voltammetry (CV) with a silver/silver chloride 3 M sodium chloride reference electrode and a platinum counter electrode (CV-50W voltammetric analyzer; Bioanalytical Systems Inc, West Lafayette, IN).

3.3.1 Field Emission Scanning Electron Microscopy

The characterization on nanostructures is very much dependent on surface morphological imaging technique. In order to view submicron to nanosize of structures, an optical microscope is no longer applicable due to the resolution limit. Scanning Electron Microscopy (SEM) is usually used to study the surface morphology of the micro/nano-structures materials. This is because electron microscope gives much better resolution and depth of focus due to the natural behavior of electron compared to photon.

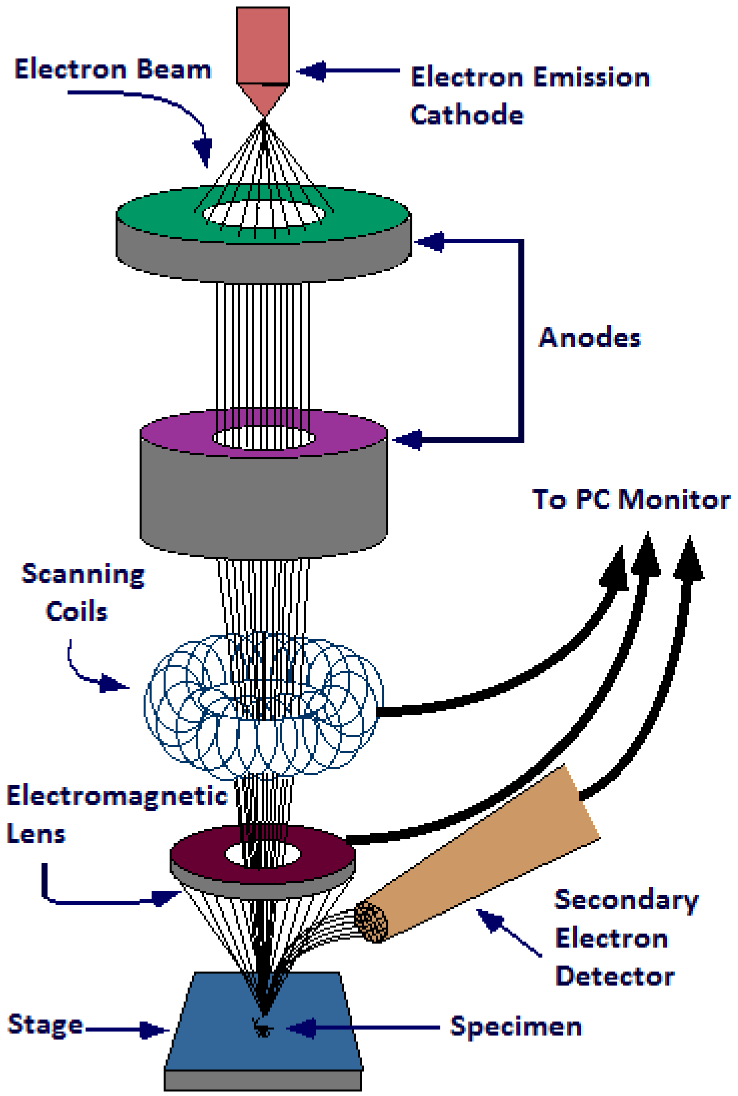

Figure 3.6: Simplified internal structure of FESEM.

The electron source in SEM is produced by two types of electron guns namely, thermionic and field emission guns. Thermionic gun is commonly used to apply electrical current to heat up the filament (e.g. tungsten). The electron can escape from the filament material when the heat is high enough. Nonetheless, thermionic gun has the disadvantages of low brightness and thermal drift during operation. Hence, field emission gun or cold cathode field emitter can be used to prevent these problems without heating up the filament. The field emission gun is normally a filament sharpened to a point or small tip. This sharp point is essential in concentrating the electric field to a very high level, yielding a huge electrical potential gradient which in turn pulls the electrons away from the filament material and accelerates it. Moreover, the difference between the conventional SEM and Field Emission Scanning Electron Microscopy (FESEM) is dependent on the type of electron gun used. Field Emission (FE) gun can achieve up to three orders of magnitude greater electron density. Thus, FESEM is better than SEM because it gives a clearer image with improved spatial resolution and less electrostatic distortions and damage.

A FE gun consists of a sharp tip (< 0.1 μm), commonly made of tungsten to serve as cathode. There are two anodes present in the FE gun in which the first one helps to limit the current while the second anode focuses and accelerates the electron beam. Electromagnetic lens are utilized to focus the electron beam by applying magnetic field in a horizontal radial direction. The scanning coil is then used to deflect the electron beam to the sample by controlling the current through radially oriented coils. The incident electron beam with energy of a few hundred eV to 50 keV interacts with the sample atoms and generates a number of signals. These signals are detected and measured by a detector and transformed into a digital image.

The detectable signals generated when the electron beam interacts with the sample atoms (electron or nuclei) in a FESEM. The incident electron beam collides with the electron in the sample atom giving rise to elastic and inelastic scattering. These elastic and inelastic scattering caused various types of electrons being emitted such as X-rays, Auger electrons, secondary electrons, and backscattered electrons. The angle and velocity of these secondary electrons relates to the surface structure of the object. This process is continued until the incident electron loses its energy. Secondary electrons emitted from 200 Å within the sample are the most common signal detected by the electron detector. Image of the samples will then be constructed and displayed on a pc monitor.

Drop casting is a suitable method for FESEM sample preparation. Solvent like ethanol is used to disperse the sample and then it will be drop casted onto a Si/SiO_2 substrate. It is critical to make sure that the sample is clean, dried and properly mounted on a sample holder before loading it on to the specimen stage.

The morphology of the prepared GO was characterized using an FEI Nova NanoSEM 400 field emission scanning electron microscope (FESEM; FEI, Hillsboro, OR).

3.3.2 Ultraviolet-Visible Absorption Spectroscopy

UV-Vis refers to absorption spectroscopy or reflectance spectroscopy in the ultraviolet-visible spectral region. The operation mechanism of UV-Vis is based on the interaction between light and matter. In this case, light is utilized in the visible and adjacent (near-UV and near-infrared (NIR)) ranges. The absorption or reflectance in the visible range will have an effect in the perceived colour of the chemicals involved. In this region of the electromagnetic (EM) spectrum, molecules undergo electronic transitions. Absorption spectroscopy measures transitions from the ground state to the excited state. This in turn results in the absorption of EM radiation by the samples. The EM radiation with different energy emitted at any particular wavelength is dependent on the temperature of the sample. It can be well explained with blackbody radiation, which indicates that the wavelength of maximum energy shift to lower wavelength as emitted energy increases with temperature.

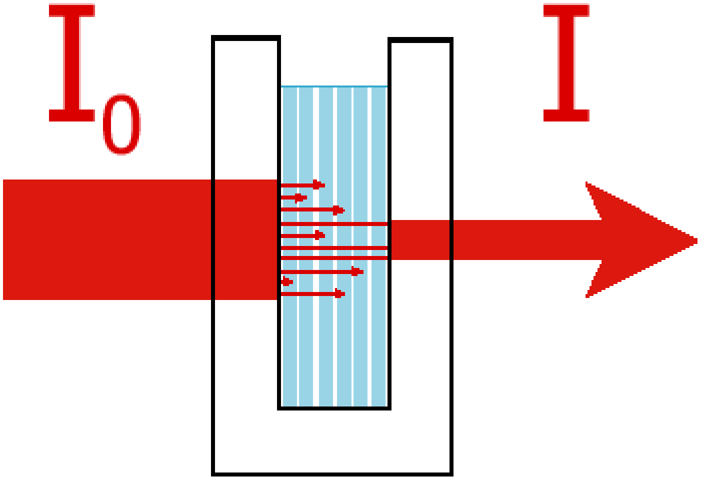

Figure 3.7: A monochromatic light I_0 passing through a sample cell. The light intensity, after having passed through the cell, is decreased to I because of adsorption.

As illustrated in **Figure 3.7**, when a beam of monochromatic light, I_0, passes through a solution, the optical transmittance T is defined as

$$T = I/I_0, \qquad (3.1)$$

where I and I_0 are the light intensities before and after passing through the sample cell, respectively. The percent transmittance,$\%T = 100T$, is often used. The absorbance (A), is defined by

$$A = \log\left(\frac{I_0}{I}\right) = \log(1/T) \qquad (3.2)$$

The Beer-Lambert law states that the absorbance is directly proportional to the concentration of the absorbing species (c, mol/L) in the solution and the path length (l, cm):

$$A = \mathcal{E}lc, \qquad (3.3)$$

where Ɛ is the molar extinction coefficient (L mol^{-1} cm^{-1}). Ɛ is a measure of the amount of light absorbed per unit of concentration.

Thus, for a fixed path length, UV-Vis spectroscopy can be used to determine the concentration of the absorber in a solution. It is important to know how quickly the absorbance varifies with concentration. This can be obtained from references (tables of molar extinction coefficients), or more accurately, determined from a calibration curve.

Ɛ is not constant and often varies with the wavelength (λ). According to Equation (3.3), at a fixed l and a given c, variation in Ɛ with λ results in the variation of A. The variation of A with λ is called a spectrum.

For a substance to have a UV-Vis absorbance, it must have an excited state. Note that not all substances can be excited to enter an excited state. Transition metal ions have such excited states to show absorption bands in the range of visible light (400-700 nm). For organic compounds, a variety of energy absorption is possible, depending on the nature of the bonds within a molecule. Electrons in organic molecules may be in strong sigma (σ) bonds, in weaker pi (π) bonds, or nonbonding (n). When energy is absorbed, all of these types of electrons can be excited to the antibonding states respresented with σ^* and π^*. Most $\sigma \rightarrow \sigma^*$ absorptions for individual bonds occur below 200 nm of UV light, whereas $\pi \rightarrow \pi^*$ and $n \rightarrow \pi^*$ absorptions occur in the near-UV-Vis region.

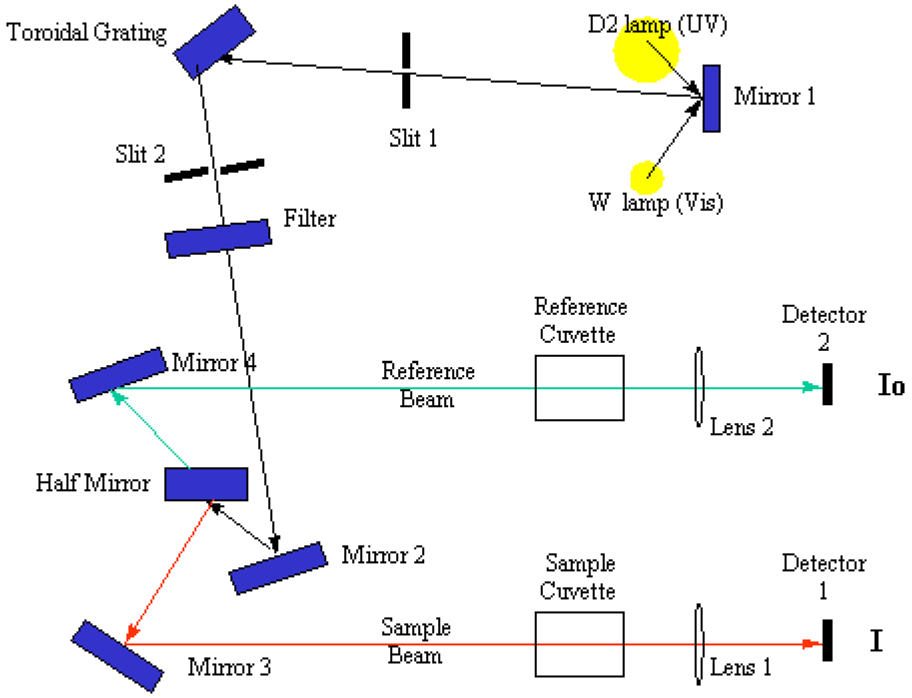

Figure 3.8: A UV-Vis optical system (Dios, 2000).

A schematic illustration of a UV-Vis spectroscopy system is shown in **Figure 3.8.** The key components of the system are namely, a light source (UV lamp), a diffraction grating unit, a filter, a half mirror, four normal mirrors, a sample cuvette, a reference cuvette, and two detectors. A beam of UV-Vis light from a UV lamp is separated into its component wavelengths by a diffraction grating unit, for instance a prism. Slit 1 helps in adjusting the amount of light entering the diffraction grating unit. Next, the monochromatic beam is split into two equal intensity beams by a half mirror, one for the sample and another one for the reference cell. This arrangement is essential to assure that the sample and the reference cells receive the same monochromatic beam. After that, the intensities of these light beams are measured by two electronic detectors and compared. The intensity of the beam coming from the sample cell is represented as I, whereas the intensity of the beam of the reference cell is defined as I_0. Over a short period of time, the spectrometer automatically scans all the component wavelengths, for example, 200-800 nm. The light that has passed through both sample and reference is incident on the photomultiplier tube or PbS photoconductive cell. Then, the detected light will be converted into an electrical signal in digital form after being synchronously rectified. The signal will then finally be displayed as spectrum in PC monitor.

UV-visible spectroscopy with a scan rate of 240 nm/mm (Evolution 300; Thermo Fisher Scientific, Pittsburgh, PA) was utilized for the investigation of the bond structures within the samples.

Figure 3.9: Real image of Thermo Fisher Scientific Evolution 300 UV-Vis spectrometer.

3.3.3 Micro-Raman

Micro-Raman spectroscopy is used for investigating the structural properties, including crystallinity, crystalline to amorphous phase transition or vice versa, and crystalline (or amorphous) phase distribution. Raman spectroscopy involves the study of the interaction of light and matter in which the light is inelastically scattered, a process named as the Raman effect.

In a Raman spectroscopy, photons of a single wavelength are focused onto a sample. In this case, a laser is most commonly used as a monochromatic source. The photons will then interact with the molecules and are either reflected, absorbed or scattered. In Raman spectroscopy, we focus on the study of scattered photons.

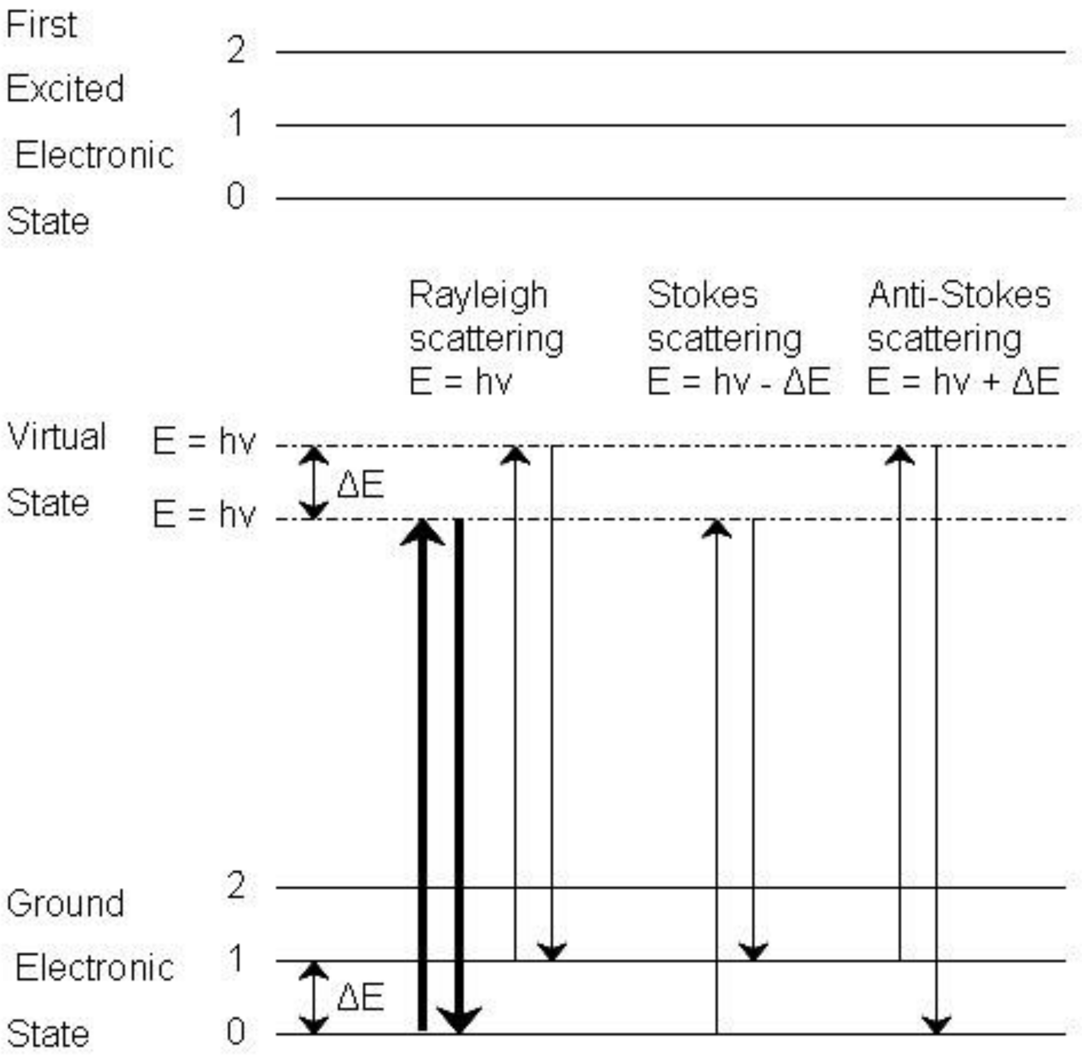

Figure 3.10: Energy level diagram showing the states involved in Raman signal (Courtney Payne & Barron, 2010a).

When a sample is irradiated with an intense monochromatic light source, most of the light is elastically scattered in the same wavelength as the light source by the sample. A small portion of the incident light is scattered at a wavelength being shifted from the excitation light source. The former is known as Rayleigh scattering, while the latter is attributed to Raman scattering. Micro-Raman spectroscopy actually measures the shift in frequency of the scattered light from the excitation light source.

In Raman scattering, the incident photon interacts with matter and its wavelength is either shifted to higher or lower energy level (blue or red shifted, respectively). Red shifted photons are more common, corresponded to "Stokes shift". What has happened is that the photon has interacted with the electron cloud of the bonds present in the functional groups, which eventually excited an electron into a virtual state. The electron then relaxed into a less excited vibrational or rotational state. This causes the photon to lose some of its energy and is detected as Stokes Raman scattering. This loss of energy is directly related to the functional group, the structure of the molecule to which it is attached, the types of atoms in that molecule and its environment. This will then give us information about the structural properties of the materials.

The standard Raman instrument is composed of three major components. Firstly, the instrument must have an illumination system which is usually composed of one or more lasers. The next major component is the sample illumination system, in which it determines the phase of material under investigation. Another necessary piece of a Raman system is the spectrometer. The spectrometer is normally placed 90 ° away from the incident illumination and may include a series of filters or a monochromator. An example of a micro-Raman setup can be seen in **Figure 3.10**. A micro-Raman spectrometer normally uses a microscope to magnify its spatial resolution.

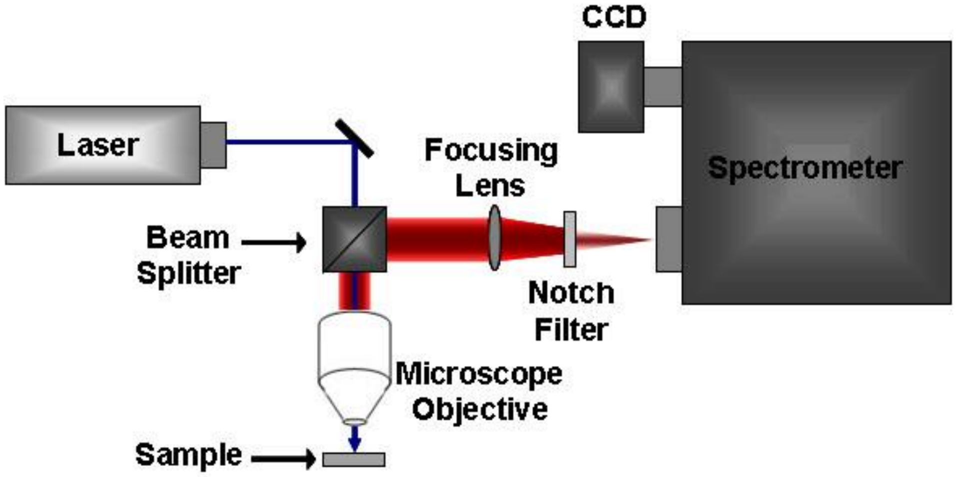

Figure 3.11: Schematic diagram of a micro-Raman spectrometer (Courtney Payne & Barron, 2010b).

The Raman spectrometer portion of the micro-Raman spectrometer is an optical instrument used to measure the intensity of light relative to its Stokes shift from the wavelength of the exciting laser light. This shift is represented in wavenumbers. A beam of light, collected from the sample, will then enter the device. It is separated into its Stokes shifted frequencies by a diffraction grating. The separated light will then be focused onto a charge-coupled device (CCD) array detector. The intensity of each frequency is measured by an individual pixel on the array. Finally, the CCD is connected to a computer and the result is a spectrum which displays the intensity of the inelastically scattered light measured in wavenumbers relative to the wavelength of the exciting laser.

Raman spectroscopy was performed on a Renishaw inVia Raman microscope excited at 514 nm.

Figure 3.12: Real image of Renishaw inVia Raman microscope.

3.3.4 X-ray Photoelectron Spectroscopy

XPS was developed as a surface analysis technique in the mid of 1960s as a method to measure the elemental composition, chemical stoichiometry, chemical state, and electronic state of the elements that contained in a material. XPS spectra are obtained when a material is irradiated with a beam of X-rays and at the same time, the kinetic energy and number of electrons that escape from the top 1 to 10 nm of the material are measured and analyzed. By analyzing the kinetic energy, the bonding energy of the electrons are calculated, thus the material from which the electrons escape is identified. XPS requires ultra-high vacuum (UHV) conditions to operate in order to detect electrons efficiently and also to avoid surface contamination or reaction.

Photoionization refers to the physical process in which an incident x-ray photon with energy of hv (where h is Planck's constant (6.62×10^{-34} J s) and v is the frequency (Hz) of the radiation) ejects one or more electrons from an atom, ion, or molecule. The ejected electrons, known as photoelectrons, carry information of their preionized states. The process of photoionization can be written as:

$$A + hv \rightarrow A^+ + e^-. \qquad (3.4)$$

The left-hand side is an atom of no charge, and a photon of energy hv; the right-hand side is an ionized atom plus an ejected electron. From the energy viewpoint, the energies before and after the striking of the photon on the nucleus should be equal (conservation of energy), or:

$$E(A) + hv = E(A^+) + E(e^-). \qquad (3.5)$$

Since the energy of the ejected electron $E(e^-)$ is present solely as kinetic energy (E_K), Equation 3.5 can be rearranged to give the following expression for E_K:

$$E_K = hv - [E(A^+) - E(A)]. \qquad (3.6)$$

The final term within the square brackets is actually the difference in energy between the ionized and neutral atoms. In fact, that is what we call the binding energy (E_B) of the electron. Hence, Equation 3.6 can be rewritten as:

$$E_K = hv - E_B. \qquad (3.7)$$

E_B is a direct measure of the energy required to remove only the electron concerned from its initial level to the vacuum level. E_B is unique for a given atom and a given orbital. The kinetic energy E_K of the photoelectron is the energy of the ejected electron after it leaves the “hold” of the atom. E_K varies when a different photon energy (hv) of the x-ray is used. E_K is therefore not an intrinsic material property. The$E_B$of the electron is that which identifies the electron specifically, both in terms of its parent element and atomic energy level.

As E_K is measurable for a given x-ray source, hv is known. Therefore it is easy to determineE_B, from which one can identify the atom (element) that a particular electron had escaped from because no two elements share the same set of electronic binding energies.

A typical XPS spectrum is a plot of the number of electrons detected versus the binding energy of the electrons detected. Each element gives a characteristic set of XPS peaks at specific binding energy values which directly identify each element that exist in or on the surface of the material being analyzed. These characteristic peaks correspond to the electron configuration of the electrons within the atoms, e.g., 1s, 2s, 2p, 3s, etc. The number of detected electrons in each of the characteristic peaks corresponds to the amount of element within the area irradiated. To generate atomic percentage values, each raw XPS signal must be corrected by dividing its signal intensity (number of electrons detected) by a "relative sensitivity factor" (RSF) and normalized over all of the elements detected.

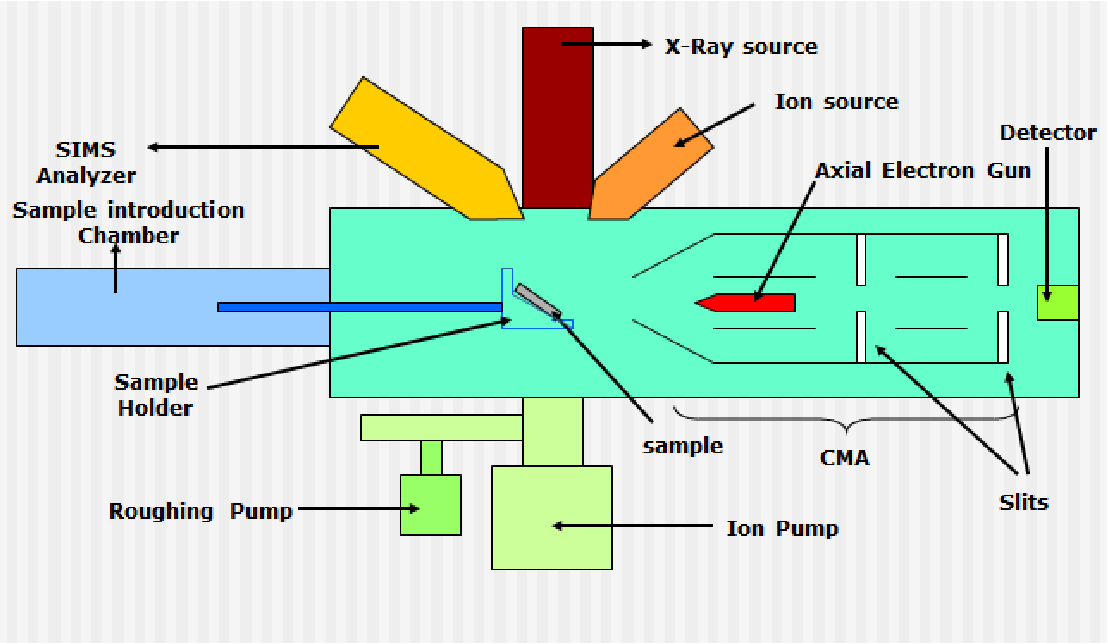

Figure 3.13: Diagram of the side view of XPS System (Torres, 2006).

The main components of a XPS system consist of X-ray source, argon ion gun, neutralizer, vacuum system, electronic controls, and computer system. In order to operate XPS system, photoelectrons are emitted from surface of the sample by a monoenergetic X-ray beam. The X-ray photons will then penetrate about a micrometer into the sample. The XPS spectrum contains information only about the top 1 to 10 nm of the sample. Ultra-high vacuum (UHV) environment is essential to eliminate excessive surface contamination. Cylindrical Mirror Analyzer (CMA) will then measure the E_K of the emitted electrons. After that, a spectrum is plotted by the computer based on the analyzer signal. E_B can then be determined from the peak positions and the identified elements present in the sample.

XPS measurement of the nanocomposites was performed by using synchrotron light at beamline no. 3.2 of Siam Photon Laboratory, Synchrotron Light Research Institute, Thailand. The XPS result was operated in the conditions of maximum photon energy 600 eV and kinetic energy step 0.1 eV.

3.3.5 X-ray Diffraction

XRD is a rapid analytical technique primarily used in the characterization of the crystal structure of a material. It can provide information on the average spacing, d between layers or rows of atoms, orientation of a single crystal or grains, crystal size, crystal shape, and internal stress of small crystalline regions (Coscia et al., 2003). As XRD is only sensitive to crystalline structures, it can be utilized on both homogeneous and inhomogeneous samples, which is suitable for the structural characterization of nanomaterials.

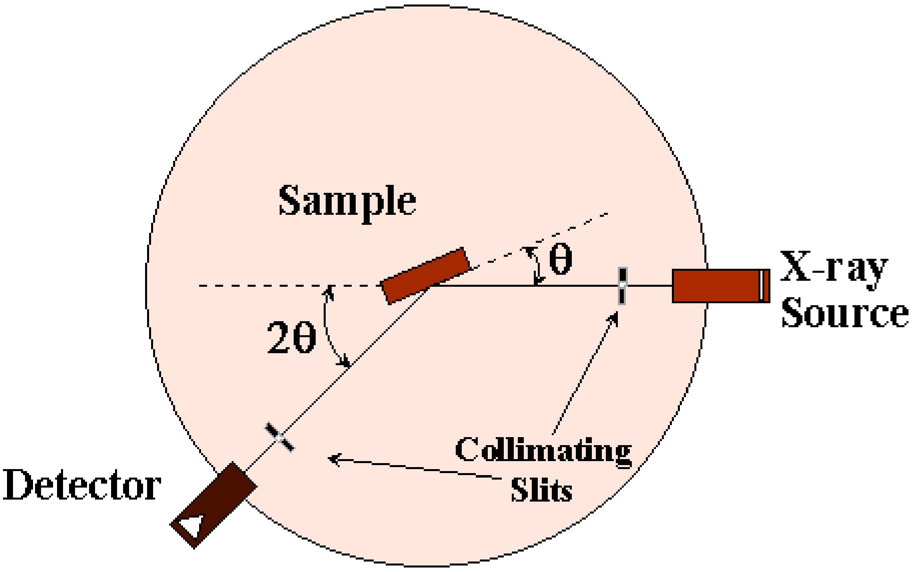

Figure 3.14: Schematic diagram of the XRD (Ali, 1999).

X-ray diffraction works based on the constructive interference of monochromatic X-rays and a crystalline sample. The X-rays are generated in a cathode ray tube by accelerating electron towards a Cu anode plate, filtered to produce monochromatic radiation, collimated to concentrate, and directed toward the sample. It should be noted that diffraction only occurs when Bragg's law is satisfied, meaning that diffraction of waves only occurs at certain angles called Bragg angles, where the wave patterns of the beam leaving the atomic planes are in phase (constructive interference). Bragg's law developed by Bragg in 1914 and can be expressed as $n\lambda = 2dsin\theta$, where n is an integer in order of diffraction, λ is the wavelength of incident X-ray beam, d is the spacing between atomic layers in crystal and θ is the angle of incidence and reflection of incident ray. Intensity of the diffracted X-ray beam is measured as the number of current pulses per unit time by an electronic X-ray detector. By scanning the sample through a range of 2θ angles, all possible diffraction directions of the lattice are attained due to the random orientation of the material. Conversion of the diffraction peaks to d-spacing allows identification of the element because each element has a set of unique d-spacing. Typically, this is achieved by comparison of the measured d-spacing with standard reference patterns.

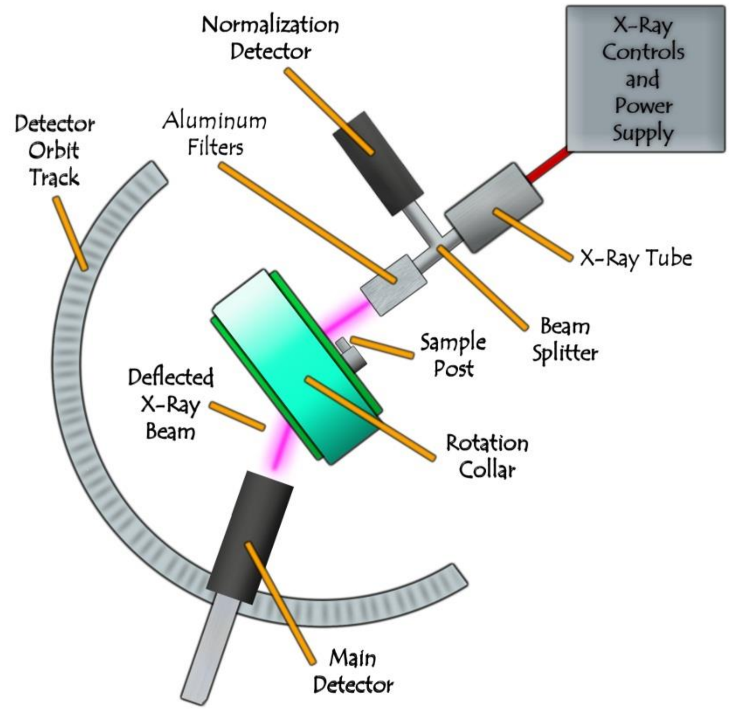

Figure 3.15: Basic features of the XRD (JGoodson, 2005).

X-ray diffractometer consists of three basic components namely, an X-ray tube, a sample holder, and an X-ray detector. Firstly, X-rays are generated in a cathode ray tube by heating a filament to produce electrons. The electrons are then accelerated toward a target by applying voltage, and the target material is bombarded with these electrons. When electrons have sufficient energy to dislodge inner shell electrons of the target material, characteristic X-ray spectra are produced. These spectra consist of several components, the most common being K_α and K_β. K_α can be classified into

$K_{\alpha1}$ and $K_{\alpha2}$. $K_{\alpha1}$ has a slightly shorter wavelength and twice the intensity as $K_{\alpha2}$. The specific wavelengths are characteristic of the target material (Cu, Fe, Mo, Cr). Filtering, by foils or crystal monochrometers, is essential to produce monochromatic X-rays needed for diffraction. $K_{\alpha1}$ and $K_{\alpha2}$ are sufficiently close in wavelength such that a weighted average of the two is used. Copper is normally used as the target material for single-crystal diffraction, with CuK_{α} radiation = 1.5418Å. These X-rays are collimated and directed onto the sample. During the measurement, the X-ray detector is mechanically rotated in an angle of 2θ accompanied by a rotation of sample holder in an angle of θ, while the angle of incident beam to sample holder always keeps at θ. Thus, the angle of incident beam is always equal to the angle of diffracted beam. When Bragg's law is satisfied in measuring a crystalline sample, constructive interference is formed and the X-rays are diffracted at maximum intensity. This results in the diffraction peak in XRD pattern. A detector will record and process this X-ray signal. The signal will then be converted to a count rate which is then output to a device such as a printer or computer monitor.

The atomic structure of the samples was investigated by X-ray diffraction (XRD, D5000, Siemen) (XRD) using copper $K\alpha$ radiation (λ = 1.5418 Å) at a scan rate of 0.02 degrees s^{-1}.

Figure 3.16: Real image of Siemens Diffractometer D5000.

3.3.6 Transmission Electron Microscopy

TEM plays a crucial role in the characterization of the structural properties and crystallinity of the RGO/TiO_2 nanocomposites. Atomic structure of the nanoparticles can be directly investigated by employing High Resolution Transmission Electron Microscopy (HRTEM). A high resolution of ~1 Å is theoretically obtained in a HRTEM due to the shortening in de Broglie wavelength of the high energetic electron beam. This is particularly useful in the determination of the crystalline or amorphous structures and structure defects such as lattice dislocation within the nanoparticles. It can also be used to identify the atomic lattice spacing, crystalline plane, preferred orientation and growth direction of the nanoparticles.

TEM uses high energy electrons (can be up to 300 kV accelerating voltage) which are accelerated to nearly the speed of light. The electron beam in this case behaves like a wavefront with wavelength about a million times shorter than lightwaves. Electrons are scattered when an electron beam passes through a thin-section specimen of a material. A sophisticated system of electromagnetic lenses will then focuses the scattered electrons into an image or a diffraction pattern, or a nano-analytical spectrum, depending on the mode of operation.

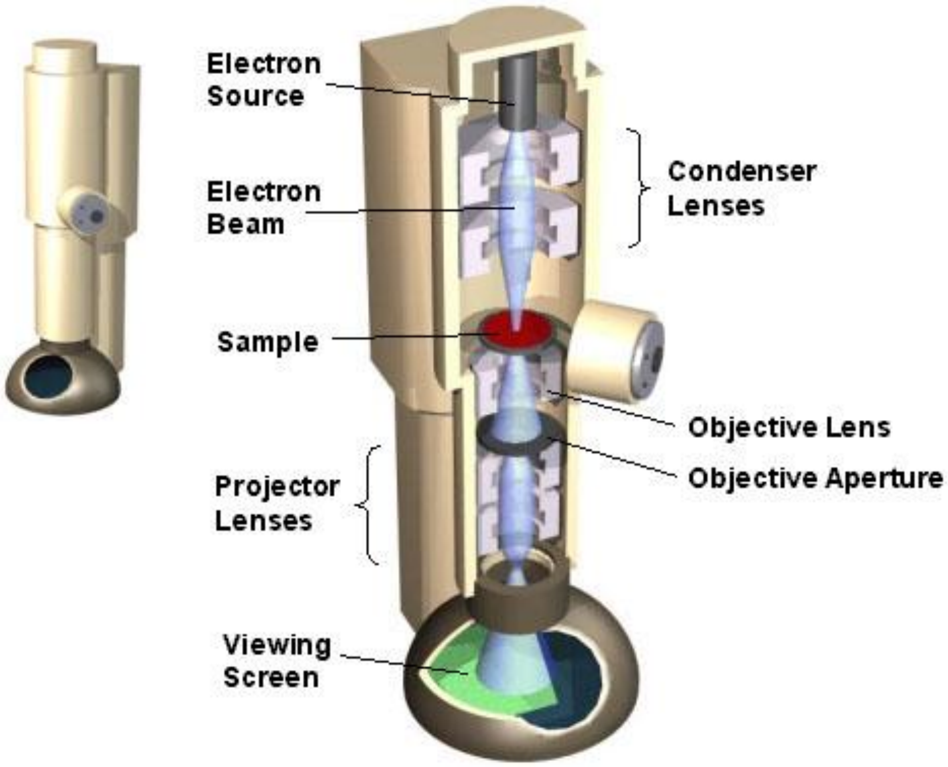

Figure 3.17: Schematic diagram of the main components of a TEM ("General: Characterization Techniques," 2012).

Figure 3.17 is a schematic diagram of the main components of a TEM. Similar to SEM, TEM is constructed with an electron gun, usually field emission gun for high resolution. This electron gun emits the electrons to travel through the vacuum situated in the column of the microscope. TEM uses electromagnetic lenses to focus the electrons into a very thin beam. The electron beam is focused by two condenser lenses into a coherent beam, and further restricted from deviation by a condenser aperture. The focused electron beams then strike the specimen and are transmitted through the specimen. Depending on the density of the material present, some of the electrons are scattered and disappear from the beam. The transmitted electrons are focused by the objective lens into an image which is then passed through the intermediate and projector lenses, and then projected on the fluorescent screen. The objective and selected area apertures are used for TEM image and diffraction pattern projections, respectively. For the TEM image projection mode, the objective aperture acts to block the high angle diffracted electrons, while, for the diffraction pattern projection mode, the selected area aperture acts to assist the examination of the diffraction of electrons. A "shadow image" of the specimen with its different parts displayed in varied darkness according to their density was then created. The image can be studied directly by the operator or photographed with a camera.

TEM was performed with a transmission electron microscopy (CM12; Philips) operated at 100 kV, which allowed an image of the nanoparticles and graphene flakes to be acquired.

3.3.7 Thermogravimetric Analysis

TGA is a technique in which the mass of a substance is measured as a function of temperature or time as the sample specimen is subjected to a controlled temperature program in a controlled atmosphere. Measurements are primarily used to determine the composition of materials and to predict their thermal stability at temperatures up to 1000 ° C. This technique can also be used to characterize materials that exhibit weight loss or gain due to decomposition, oxidation, or dehydration. Thus, TGA is able to provide information about the moisture and volatile content of materials, thermal stability, decomposition kinetics, oxidative stability, composition of multicomponent systems, and effect of reactive or corrosive atmospheres on materials.

In this case, TGA is utilized to study the thermal stability of the synthesized materials. Thermal stability is defined by the resistance of a material to permanent change in the properties caused solely by heat. When selecting materials, it is crucial to know the thermal stability of each material being considered. For polymeric materials, as an example, the thermal stability is often indicated by the onset temperature of thermal degradation. Below the onset degradation temperature, a polymeric material may soften upon heating, but its molecular structure does not change by heating. The onset degradation temperatures for polymers can be conveniently determined by TGA because a polymer usually starts to show weight loss at the moment it starts to degrade. This is because the thermal degradation of a polymer results in the production of small molecules (e.g., monomers) that are volatile. These onset degradation temperatures are the highest temperatures to be applied for these polymers.

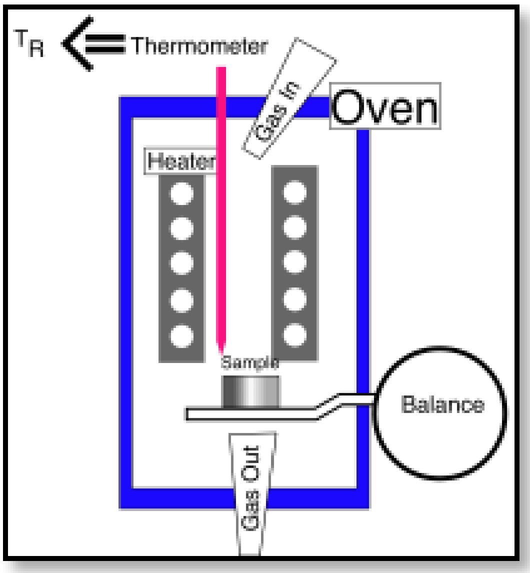

Figure 3.18: Schematic principle of TGA measurement (Adalsteinsson, 2008).

The principle of TGA is simple. As shown in **Figure 3.18**, TGA uses a balance, where on one side of the balance the specimen is placed on a pan and the pan is suspended in the oven or furnace. The other side of the balance holds additional weights to offset the mass of the apparatus. In a heating process at a selected heating rate, the balance is zeroed and the sample pan is heated according to a predetermined thermal cycle. The balance operates on a null-balance principle. At the zero or "null" position, equal amounts of light shine on the two photodiodes. If the balance moves out of the null position, an unequal amount of light shines on the two photodiodes. Current is then applied to the meter movement to return the balance to the null position. The amount of current applied is proportional to the weight loss or gain.

The chemical stability was investigated using thermogravimetric analysis (TGA) (Q500; TA Instruments, New Castle, DE) that was fitted to a nitrogen purge gas, and heated at a rate of 20 ℃ min^{-1}.

3.3.8 Photoluminescence Emission Spectrum

When light of sufficient energy is incident on a material, photons are absorbed and electronic excitations are created. These excitations eventually relax and the electrons return to the ground state. If radiative relaxation occurs, the emitted light is called PL. This light can be collected and analyzed to give information about the photoexcited material. The PL emission spectrum provides the transition energies, which can be utilized to determine electronic energy levels. The PL intensity gives a direct measure of the relative rates of radiative and nonradiative recombination.

PL is very much dependant on the nature of the optical excitation. The excitation energy selects the initial photoexcited state and governs the penetration depth of the incident light. The PL signal also often depends on the density of photoexcited electrons. In order to control this parameter, the intensity of the incident beam can be adjusted accordingly. When the type or quality of material under investigation varies spatially, the PL signal will then vary with excitation position. Futhermore, pulsed optical excitation provides a powerful means to study transient phenomena. Short laser pulses yield virtually instantaneous excited populations, after which the PL signal can be monitored to determine recombination rates.

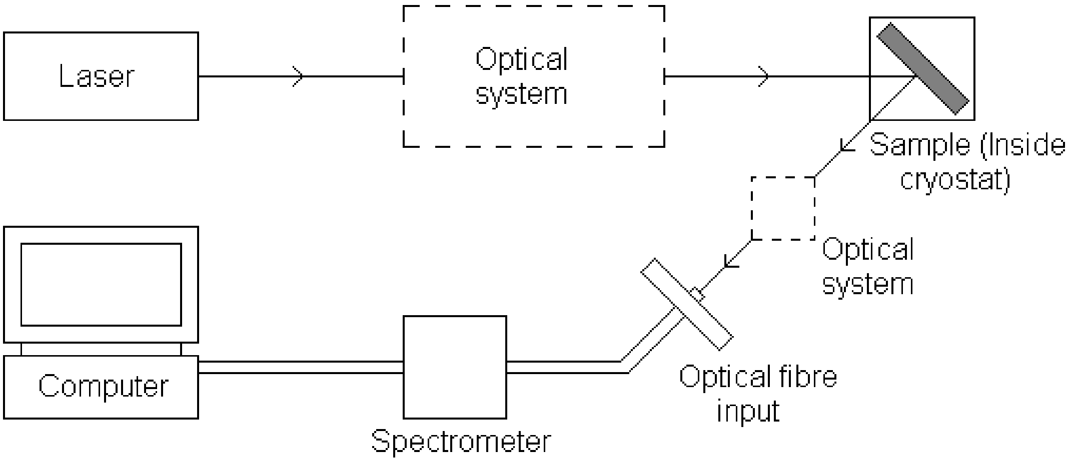

Figure 3.19: Typical experimental set-up for PL measurements (Powell, 2011).

PL is simple, versatile, and nondestructive. The instrumentation that is required for PL to work is modest. This includes an optical source and an optical power meter or spectrophotometer. A typical PL set-up is shown in **Figure 3.19**. First of all, a laser tuned to a wavelength close to the bandgap energy of the sample is directed onto the sample. The sample may be held in a cryostat to facilitate the measurements being taken under low temperatures. When the light from the laser beam hits the sample, photoluminescence occurs and light is emitted from the sample at wavelengths dependent on the composition of the sample. This sample is oriented such that the reflected laser beam and the PL emission propagate in different directions.

After that, the emitted light is directed into a fibre optic cable and then into a spectrometer. A filter may be placed in front of the fibre input to filter off any incident laser light. Inside the spectrometer, a diffraction grating diffracts different wavelengths in different directions towards an array of photo-detectors which measure the intensity of each wavelength component. The digital information is then interpreted by the computer, displaying a PL spectrum. The spectrum indicates the relative intensities of the light of various wavelengths entering the detector. The whole process must be carried out in the dark.

As the measurement does not rely on electrical excitation or detection, sample preparation is not that critical. This feature makes PL particularly suitable for material systems exhibiting poor conductivity or undeveloped contact/junction technology. The measurement of the continuous wave PL intensity and spectrum is fast and straightforward. On the other hand, investigating transient PL is more challenging, especially if recombination processes are fast. Instrumentation for time-resolved detection, such as single photon counting, can be quite expensive and complex. Even so, PL is one of the only techniques available for investigating fast transient behavior in materials.

PL curves were obtained by using Renishaw inVia PL microscope excited at 325 nm.

3.3.9 Cyclic Voltammetry

CV is one type of potentiodynamic electrochemical measurements in which the operating process is a potential-controlled reversible experiment. It scans the electric potential before turning to reverse direction after reaching the final potential and then scans back to the initial potential, as shown in **Figure 3.20**. When the voltage applied to the system changes with time, the current will change with time accordingly. This is shown in Figure 1b. Hence the curve of current and voltage, illustrated in Figure 1c, can be represented from the data, which can be obtained from Figure 1a and b.

CV is a very important analytical characterization tool in electrochemistry. Any process that includes the transfer of electron can be studied with this characterization. For example, the investigation of catalytic reactions, analyzing the stoichiometry of complex compounds, and determining of the photovoltaic materials' band gap. In this work, CV is used to study the application of the synthesized nanocomposites in the detection of mercury ions.

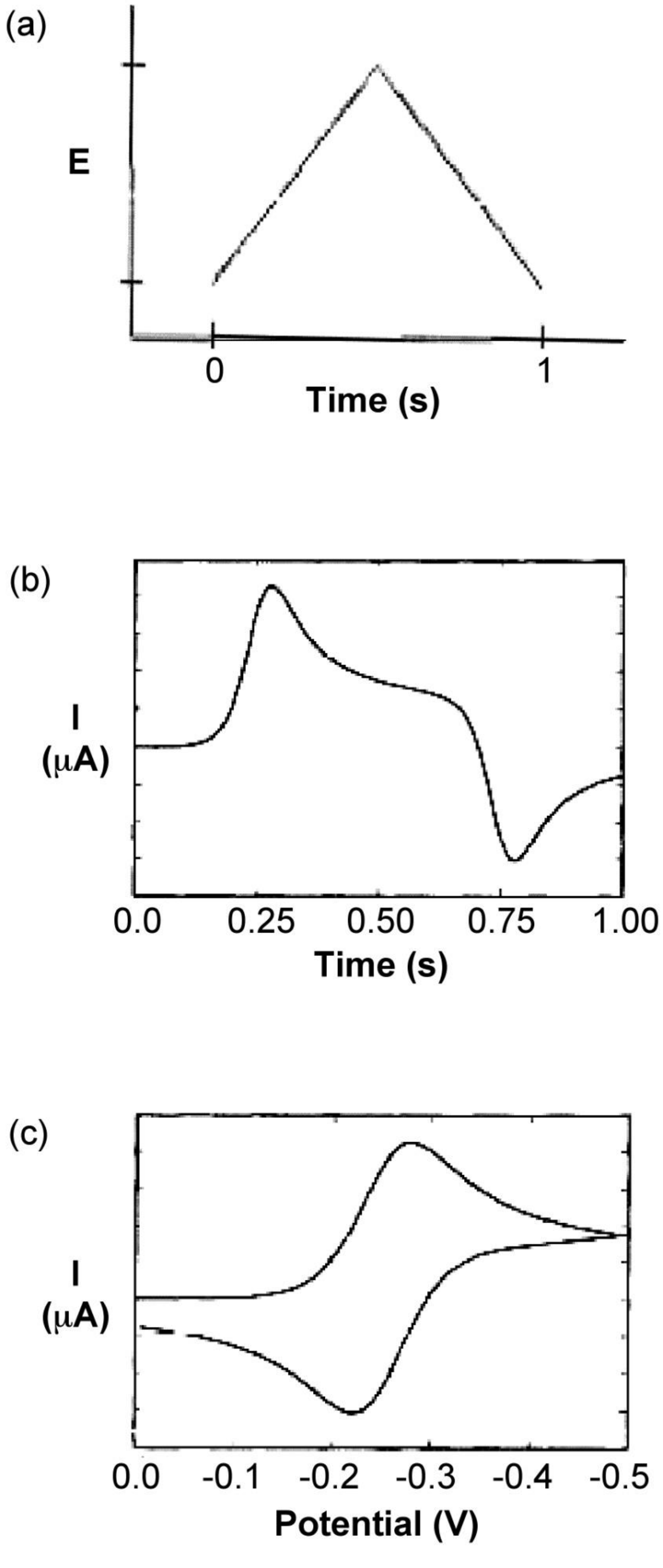

Figure 3.20: Diagram of (**a**) potential wave changes with time, (**b**) current response with time, (**c**) current-potential representations (Gosser, 1993).

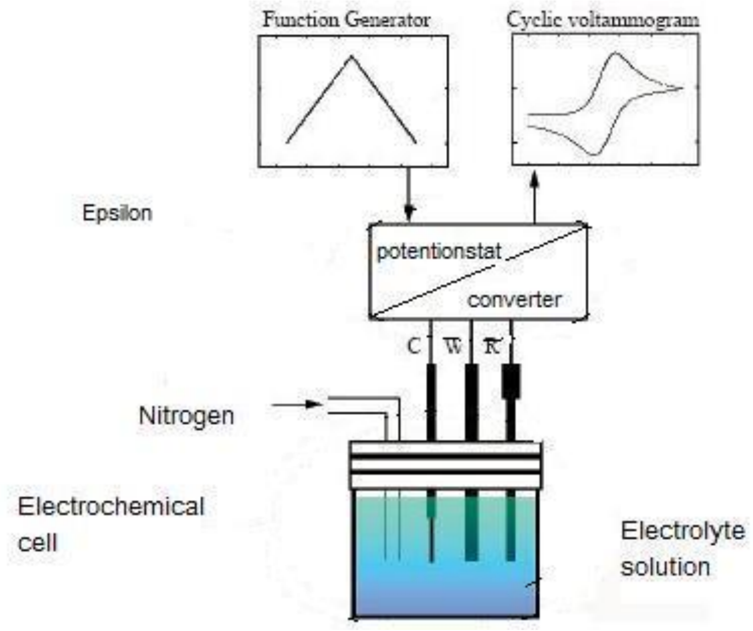

Figure 3.21: Components of CV systems (Gosser, 1993).

The CV systems basically consist of the following components. First of all, the epsilon includes potentiostat and current-voltage converter. The potentiostat helps to control the applied potential, and a current-to-voltage converter is required for measuring the current. Secondly, the input system is a function generator. Operators can be used to change the parameters such as the scan rate and scan range. The output part is a computer screen, showing the data and curves directly to the operators. Sometimes, the oxygen and water in the atmosphere will dissolve in the solution, and will be deoxidized or oxidized when voltage is applied. This will produce a less accurate data. To prevent this from happening, bubbling of an inert gas like nitrogen or argon gas is essential. The key component of the CV systems is the electrochemical cell. The electrochemical cell is connected to the epsilon part and it contains three electrodes, counter electrode (C in **Figure 3.21**), working electrode (W in **Figure 3.21**) and reference electrode (R in **Figure 3.21**). All of the electrodes must be immersed in an electrolyte solution for the CV system to function well.

A three-electrode cyclic voltammetry with a silver/silver chloride (Ag/AgCl) 3 M sodium chloride (NaCl) reference electrode and a platinum (Pt) counter electrode (CV-50W voltammetric analyzer; Bioanalytical Systems Inc, West Lafayette, IN) was utilized to perform the measurements.

3.4 Applications Methods

3.4.1 Electrochemical Performance

The working electrode was 3 mm in diameter and made from a glassy carbon electrode (GCE). Before modification, the bare GCE was polished with alumina slurry on microcloth pads (MetaServ 250, Buehler) and thoroughly rinsed with distilled water between each polishing step. The final cleaning step was successive washes with distilled water and anhydrous alcohol. The modified electrode was made by tapping the bare GCE onto the sample ten times successively (Bond & Marken, 1994). The cell electrolyte was formed by mixing 10 mL of 0.1 M of potassium chloride with 190 µL of 1.0 mM mercuric chloride ($HgCl_2$) analyte. Once all three electrodes were immersed into the supporting electrolyte solution, nitrogen gas was bubbled through the solution for 15 minutes to remove any dissolved oxygen before the voltammogram was recorded. The potential range was checked before any readings on the voltammogram were recorded. All the voltammetric experiments were referred at an ambient temperature of 25 °C ± 2 °C.

3.4.2 Photocatalytic Measurements

The photodegradation of MB dyes was observed based on the absorption spectroscopic technique. In a typical process, aqueous solution of the MB dyes (0.01 g/L, *i.e.*, 10 ppm, 10 mL) and the photocatalysts (P25, 180 TiO_2, 10 mg) were placed in a 20 mL glass vial. Under constant stirring, the glass vial was exposed to natural solar light irradiation with 120 μW/cm^2/nm sunlight intensity. The instrument used to measure the intensity of the sunlight is solar simulator Oriel Instrument (AM 1.5; Newport Corporation, Irvine, CA, USA). At given time intervals, the photoreacted solution was analyzed by recording variations of the absorption band maximum (663 nm) in the UV-visible spectra of MB, using a UV-visible spectrophotometer with a scan rate of 240 nm/mm (Thermo Scientific Evolution 300). The catalysts were removed from the solution by centrifugation prior to sample analysis. The above procedures were repeated for the 120 RGO/TiO_2, 150 RGO/TiO_2, and 180 RGO/TiO_2, using 80 mL of MB instead of 10 ml in order to reach the same initial absorbance value as P25 and 180 TiO_2.

3.4.3 Dark Adsorption Test

Dark adsorption test was adopted to compare the adsorptivity of P25, 180 TiO_2, 120 RGO/TiO_2, 150 RGO/TiO_2, and 180 RGO/TiO_2. In this test, 10 mg of catalyst (P25, 180 TiO_2, 120 RGO/TiO_2, 150 RGO/TiO_2, and 180 RGO/TiO_2) was dispersed 10 ppm of MB solution with stirring and kept in the dark for 10 min in order to reach adsorption–desorption equilibrium. 10 mL of MB was used for P25 and 180 TiO_2 while 80 mL was utilized for 120 RGO/TiO_2, 150 RGO/TiO_2, and 180 RGO/TiO_2. The dispersion was then centrifuged and the MB solution was taken to the UV-visible absorption measurement. From the difference in the absorbance before and after absorption, the amount of dyes adsorbed by the catalyst could be estimated.

3.4.4 Durability Test

For the durability test of RGO/TiO_2 catalyst in the photodegradation of MB under natural solar light, five consecutive cycles were tested. The used catalyst (120 RGO/TiO_2, 150 RGO/TiO_2, and 180 RGO/TiO_2) was dispersed in 30 mL of MB solution (10 ppm), giving the same initial absorbance value as the first cycle. Then the mixture underwent five consecutive cycles, each lasting for 5 h. After each cycle, the mixture was centrifuged and the catalyst was recovered. For the next cycle, fresh MB solution (10 ppm) was added to the catalyst.

CHAPTER 4 : RESULTS AND DISCUSSION

4.1 Introduction

In this chapter, the morphology of the as-prepared large area graphene oxide was characterized by using FESEM. The successful formation of RGO/TiO_2 nanocomposites was then confirmed with UV-Vis absorption spectroscopy, micro-Raman spectroscopy, and XPS. In order to study the effect of reaction temperature on the synthesis of RGO/TiO_2, XRD, TEM, and TGA were utilized. The effect of the hydrothermal temperature on the size distribution of RGO/TiO_2 nanocomposites was examined by TEM. TEM showed that the nanoparticles were uniformly distributed on the RGO nanosheet. XRD on the other hand, gave information on the degree of crystallinity of the nanocomposites formed at different reaction temperature. The stability of RGO/TiO_2 is also affected by the hydrothermal temperature which was then studied under TGA. It exhibited that the nanocomposites have enhanced thermal stability over the original components. Moreover, PL emission spectrum was utilized to study the electron-hole pair recombination of the nanocomposites. The electrochemical and photocatalytic performance of the prepared RGO/TiO_2 were measured respectively with cyclic voltammetry and UV-Vis spectrophotometer. A significant enhancement in the photodegradation rate of MB under natural solar light was observed with the as-prepared RGO/TiO_2, compared to the commercial P25 and pure TiO_2 that had been synthesized by using the same method. Besides, the nanocomposites exhibited high recyclability.

4.2 Field Emission Scanning Electron Microscopy

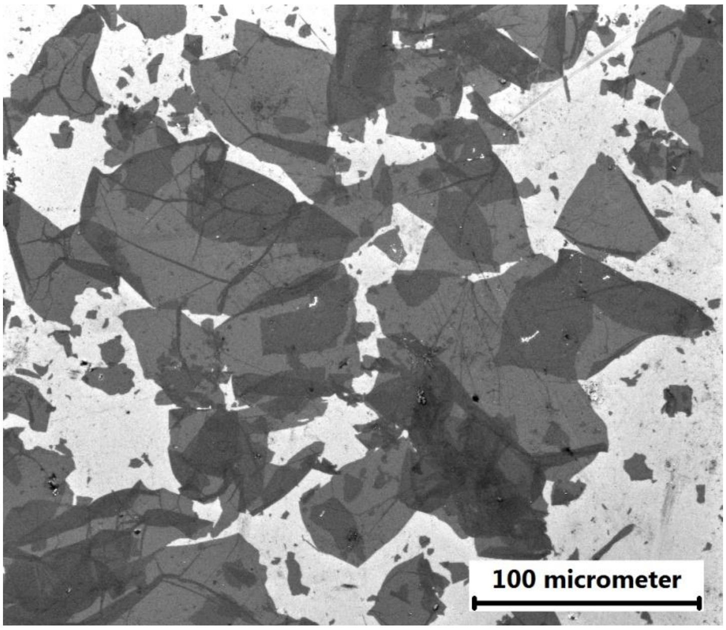

Figure 4.1: FESEM images of large area GO sheets.

A simplified Hummers' method was used to produce large area GO nanosheets. The large lateral dimension graphite flakes, were used as a starting material for the preparation of large-area GO. The resulting GO is shown in **Figure 4.1**. The large GO has an average area of 7000 μm^2 and a lateral dimension of up to 150 µm. The prepared GO was then utilized for the synthesis of RGO/TiO_2 nanocomposites.

4.3 Ultraviolet-Visible Absorption Spectroscopy

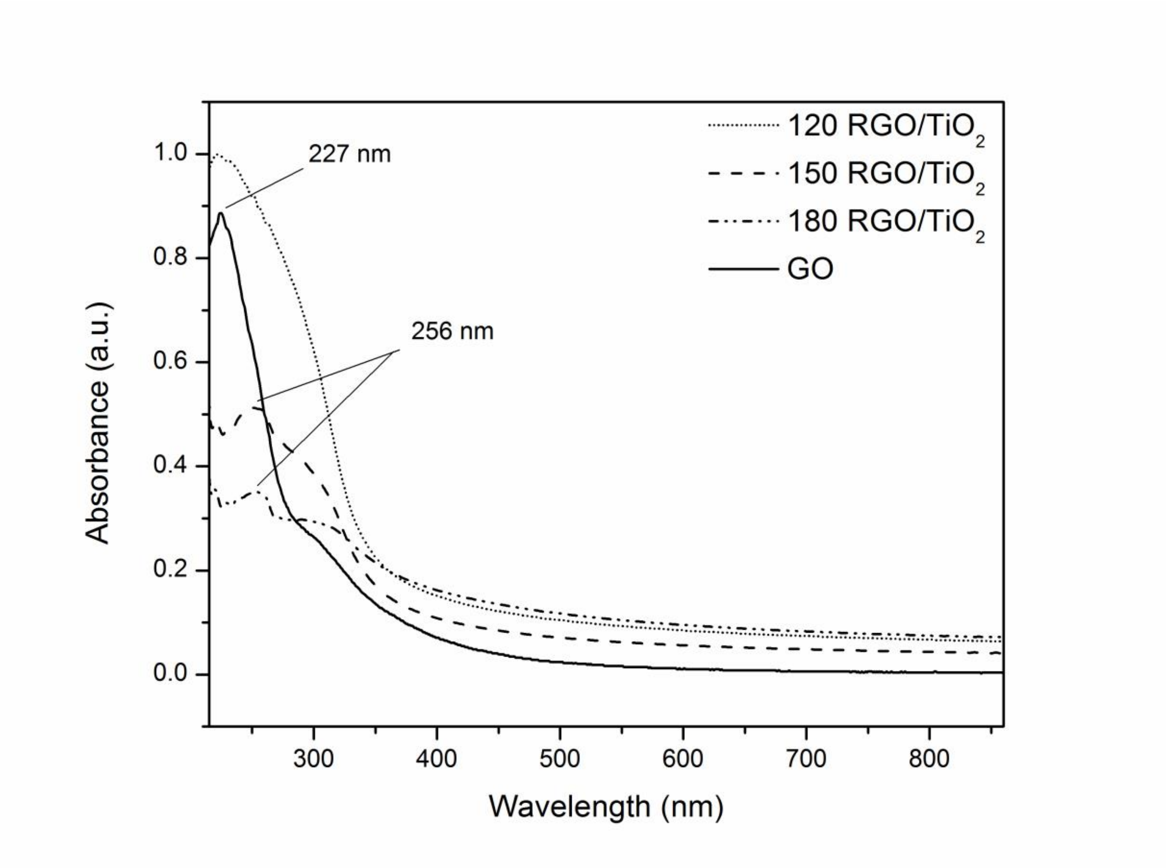

Figure 4.2: UV-Vis absorption spectra of RGO/TiO_2 and GO.

UV-Vis absorption spectroscopy measurements for RGO/TiO_2 nanocomposites are shown in **Figure 4.2** and indicate the degree of reduction in the increase of GO as the reaction temperature increased. For pure GO, there was a peak at about 227 nm and a shoulder at around 300 nm. The peak at 227 nm is assigned to the pi to anti-pi ($\pi \rightarrow \pi^*$) transition of the aromatic carbon–carbon (C-C) bonds and the shoulder at 300 nm to the n to anti-pi ($n \rightarrow \pi^*$) transitions of the carbon = oxygen (C=O) bonds (Paredes, Villar-Rodil, Martinez-Alonso, & Tascon, 2008). The 120 RGO/TiO_2 sample had a broad peak centered at 227 nm and a shoulder at approximately 300 nm. There was no evidence of a peak at 256 nm, which is a characteristic of graphene and is attributed to the aromatic carbon = carbon (C=C) bonds. For the 150 RGO/TiO_2 and 180 RGO/TiO_2 samples, the peak at 227 nm right-shifted to 256 nm. This represents the partial restoration of the pi-conjugation network of the sample as a result of the hydrothermal and chemical reduction process. All the RGO/TiO_2 nanocomposite samples showed typical absorption of TiO2 with an absorption edge of around 360 nm, while 180 RGO/TiO_2 sample showed a higher absorption edge of around 375 nm.

4.4 Micro-Raman Spectroscopy

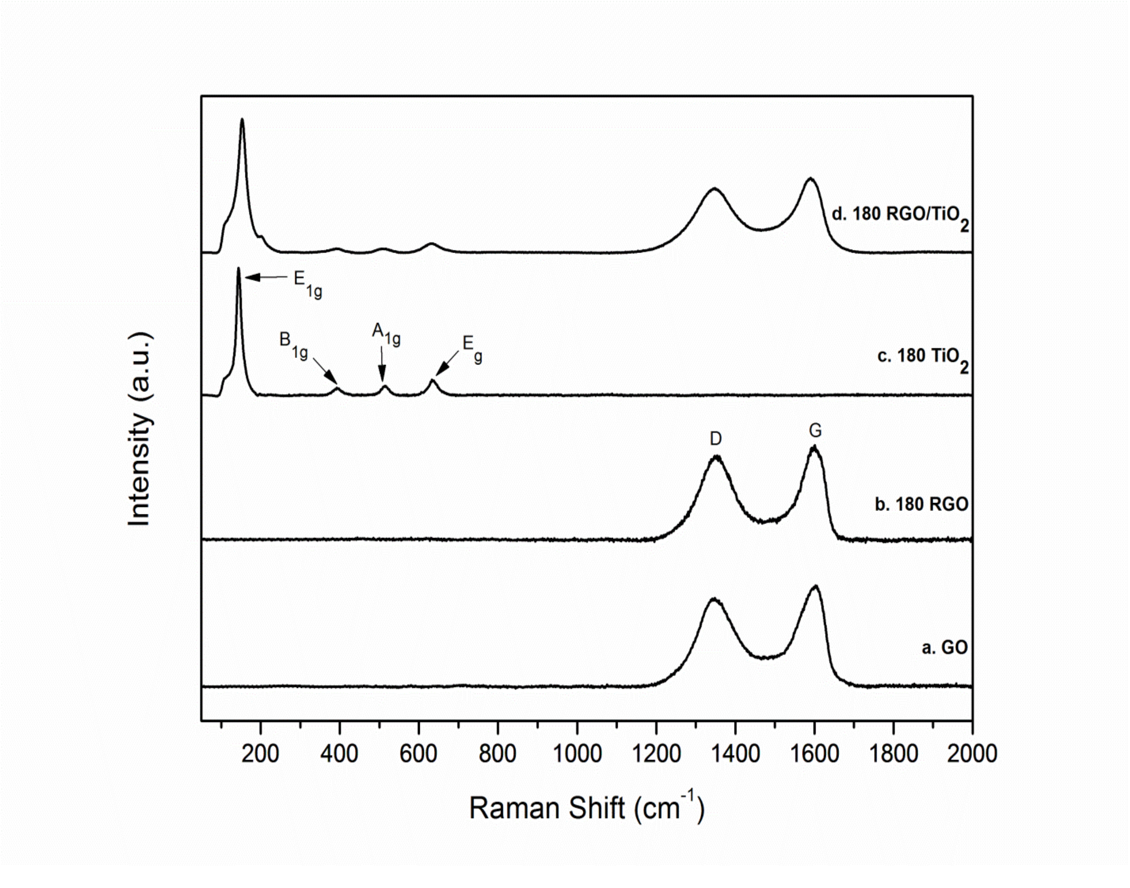

Figure 4.3: Micro-Raman spectra of GO, 180 RGO, 180 TiO_2, and 180 RGO/ TiO_2.

Micro-Raman spectroscopy is a powerful tool to characterize the structural and properties of graphene, particularly disorder and defect structures. The typical bands of graphene can be found at 1346 cm^{-1} and 1598 cm^{-1}, corresponding to the well-documented D and G bands. D band is associated with the vibrations of carbon atoms with sp^3 electronic configuration of disordered graphene, while G band is related to the in-plane vibration of sp^2-bonded carbon atoms. In the spectrum of GO [**Figure 4.3**], there exists a high D band plus a broadened and slightly shifted G band. These phenomena are due to the significant decrease in size of the in-plane sp^2 domains after the chemical oxidation and exfoliation process. RGO on the other hand, exhibited a slight increase in the D/G band intensity ratio as compared to that in the GO spectrum. This change suggests a decline in the average size of the in-plane sp^2 domain upon chemical reduction of the exfoliated GO sheets. It is reasonable to consider that the reduction of GO sheets causes fragmentation along the reactive sites and yields new graphitic domains, which led to the RGO sheets having smaller size but more numerous in number as compared to GO before reduction. The small size of RGO sheets will result in large number of edges and these edges will act as defects, consistent with the increase in the D band intensity (J. Wang, Hernandez, Lotya, Coleman, & Blau, 2009). In the spectrum of TiO_2, the four peaks observed at the low frequency region are assigned to the E_{1g} (149 cm^{-1}), B_{1g} (398 cm^{-1}), A_{1g} (516 cm^{-1}), and E_g (637 cm^{-1}) modes of anatase phase respectively (Cao et al., 2010; Eder & Windle, 2008). The G and D bands in the Raman spectrum of RGO/TiO_2 are similar to those of RGO, showing that the introduction of TiO_2 nanoparticles did not affect the structure of the RGO sheets. Compared with GO, the RGO/ TiO_2 nanocomposite displays an increased D/G intensity ratio, suggesting a decrease in the average size of the sp^2 domains upon reduction of the exfoliated GO (Stankovich et al., 2007; Tuinstra & Koenig, 1970).

4.5 X-ray Photoelectron Spectroscopy

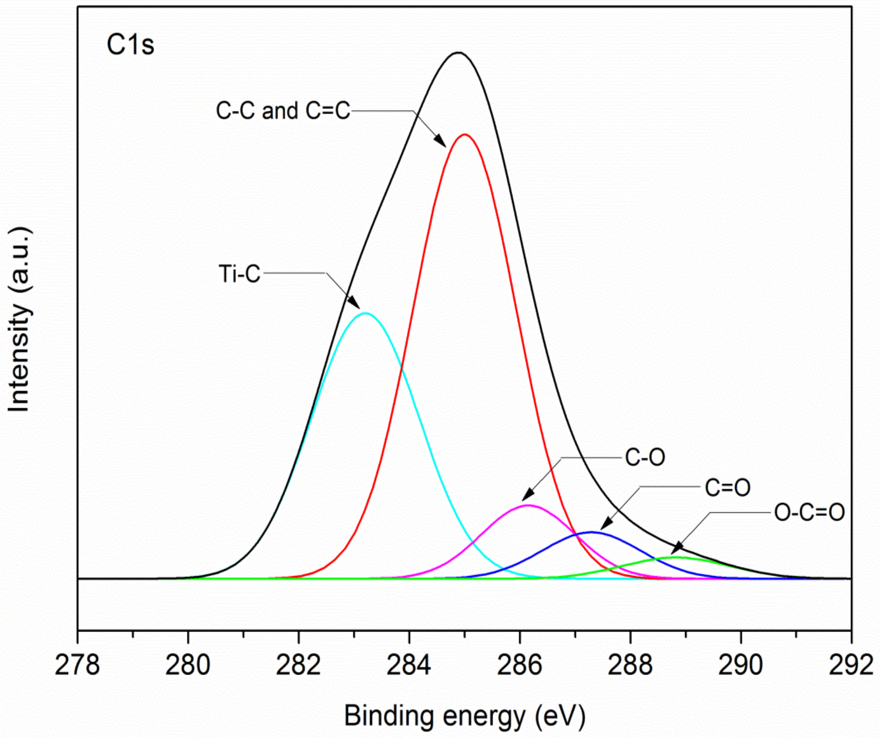

Figure 4.4: XPS of 180 RGO/TiO_2.

The deconvoluted C(1s) XPS of the RGO/TiO_2 was exhibited in **Figure 4.4**. The deconvoluted peak centered at 285.0 eV is assigned to the C-C and C=C bonds. In addition, the peaks centered at 286.2, 287.3 and 288.5 eV are attributed respectively to the C-O, C=O, and O-C=O bonds (Akhavan, Abdolahad, Abdi, & Mohajerzadeh, 2009; L.-C. Chen, Ho, Guo, Huang, & Pan, 2009). On the other hand, the deconvoluted peak centered at 283.2 eV is due to the formation of Ti-C bond (Akhavan, Azimirad, Safa, & Larijani, 2010; Akhavan & Ghaderi, 2009). This result indicates that hydrothermal process led to the formation of Ti-C chemical bond between the carbon of the RGO and the titanium of the TiO_2 nanoparticles.

4.6 X-ray Diffraction Analysis

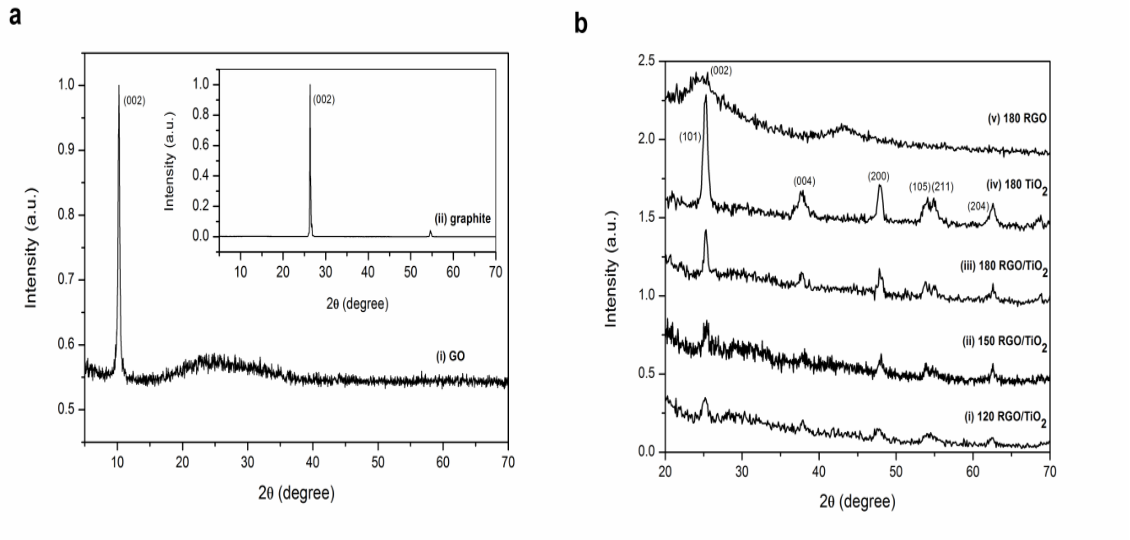

Figure 4.5: XRD patterns of (**a**) graphite and GO and (**b**) RGO, TiO_2, and RGO/TiO_2.

Figure 4.5(a) and (**b**) showed the XRD patterns of the graphite, GO, RGO, pure TiO_2, and RGO/TiO_2 nanocomposites. The dominant diffraction peak centered at around eleven degrees in the XRD pattern of GO corresponded to reflection from the (002) plane (McAllister et al., 2007; L. Zhang et al., 2010), while for raw graphite this reflection occurred at around 26 degrees. There was also a difference in the intensity of the 002 reflection of graphite and GO. For graphite, the 002 reflection was very intense with the value of 58728.50. GO on the hand, showed a weak 002 reflection with the reading of 383.33. These values were taken directly from XRD, before making any relevant normalization of the graphs. For the pure RGO sample, the (002) reflection peak was broad and was centered at around 25 degrees. The broad diffraction peak of RGO indicates poor ordering of the sheets along the stacking direction, which implies the sample was comprised mainly from single or only a few layers of RGO (Murugan, Muraliganth, & Manthiram, 2009). The band at 43 degrees corresponded to the turbostratic band of disordered carbon materials (Z. W. Xu, Huang, Min, & Chen, 2010).

No diffraction peak attributable to reflections from graphite crystal planes was observed, which suggests the stacking of the RGO sheets remained disordered and were not stacked together to form a detectable graphite structure. In addition to the peaks attributable to carbon-based compounds, the XRD spectrum contained peaks which have been assigned to reflections from the anatase phase of tetragonal TiO2 with lattice constants of a = 3.7892 Å, b = 3.7892 Å, c = 9.5370 Å, and β = 90.0000 (JCPDS 71-1167). The diffraction peaks can be indexed as reflections from the (101), (004), (200), (105), (211), and (204) planes, respectively. There was no evidence for the other phases of TiO_2 being present. Comparing the 120 RGO/TiO_2 and the 180 RGO/TiO_2 samples, there was an increase in peak intensities of the peaks attributed to the reflections from TiO_2, which suggests the formation of larger TiO2 crystallites and enhancement of the TiO_2 crystallization process (G. Wang, 2007). Full width at half maximum (FWHM) of the TiO_2 (101) reflection for the 120 RGO/TiO_2, 150 RGO/TiO_2, and 180 RGO/TiO_2 samples was 1.1595 degrees, 0.9832 degrees, and 0.6378 degrees, respectively. Since the FWHM is inversely proportional to the nanocrystal size (Scherrer equation), this result further confirms the hypothesis that higher hydrothermal temperatures produce greater TiO_2 crystallization. The presence of graphene cannot be confirmed in the XRD spectra for the RGO/TiO_2 samples because there was no peak in the XRD spectrum that can be attributed to graphene. The most likely explanation is that the relatively weak and broad characteristic peak of graphene at 24.5 degrees was masked by the strong (101) TiO_2 reflections at 25.4 degrees (Y. J. Xu, Zhuang, & Fu, 2010).

4.7 Transmission Electron Micrograph

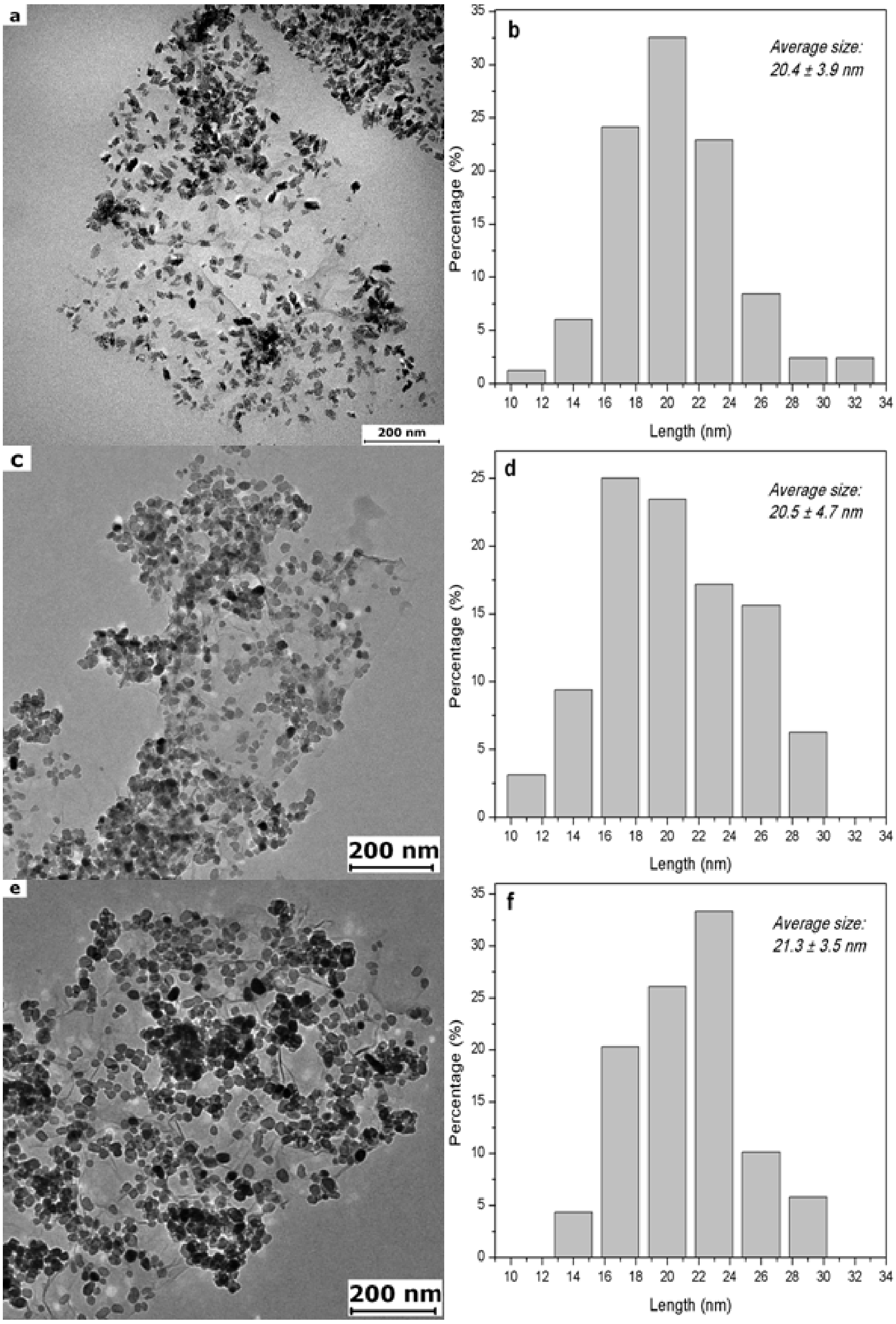

Figure 4.6: (**a**, **c** and **e**) TEM and (**b**, **d** and **f**) histogram of RGO/TiO_2 nanocomposites at (**a** and **b**) 120 ℃, (**c** and **d**) 150 ℃, and (**e** and **f**) 180 ℃.

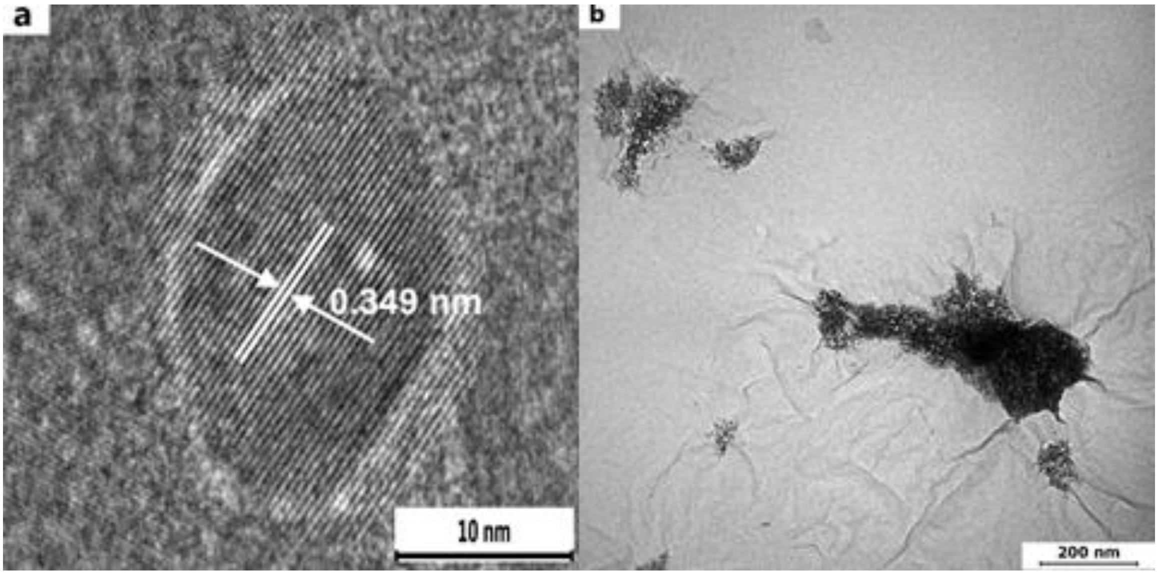

Figure 4.7: (**a)** HRTEM of RGO/TiO_2 nanocomposite. **Figure** (**b**) TEM of RGO/TiO_2 nanocomposite synthesized without TEA.

TEM of the samples are shown in **Figure 4.6** along with the size distributions of the TiO_2 nanoparticles. The nanoparticles were distributed uniformly on the basal plane of RGO nanosheets. The nanoparticles appeared to have a rounder shape in the 180 RGO/TiO_2 sample when compared to the 120 RGO/TiO_2 sample. The average size of the nanoparticles for the 120 RGO/TiO_2, 150 RGO/TiO_2, and 180 RGO/TiO_2 was 20.4 ± 3.9 nm, 20.5 ± 4.7 nm and 21.3 ± 3.5 nm, respectively. The histograms of the size distribution of the nanoparticles in the nanocomposites are exhibited on the right hand side of **Figure 4.6**. The size distribution of TiO_2 nanoparticles was narrower when the hydrothermal temperature increased. This trend agrees with the observation of more crystallized, round shaped, and homogeneous particles at 180 ℃, compared to the less crystallized, amorphous, and heterogeneous particles at 120 ℃. The HRTEM image of the selected area displayed in **Figure 4.7**(**a**) indicates a well-defined crystallinity of TiO_2 with lattice spacing of 0.349 nm, which corresponds to the (101) planes of anatase. The role of TEA in the formation of the nanocrystals can be clearly seen in **Figure**

4.7(**b**) which shows a transmission electron micrograph of the RGO/TiO_2 sample synthesized under the same conditions at 180 ℃ but without the presence of TEA. The TiO_2 nanoparticles agglomerated and did not distribute homogenously on the RGO sheet. This implies that TEA acts as capping agent allowing the formation of TiO_2 with a narrow size distribution.

4.8 Thermogravimetric Analysis

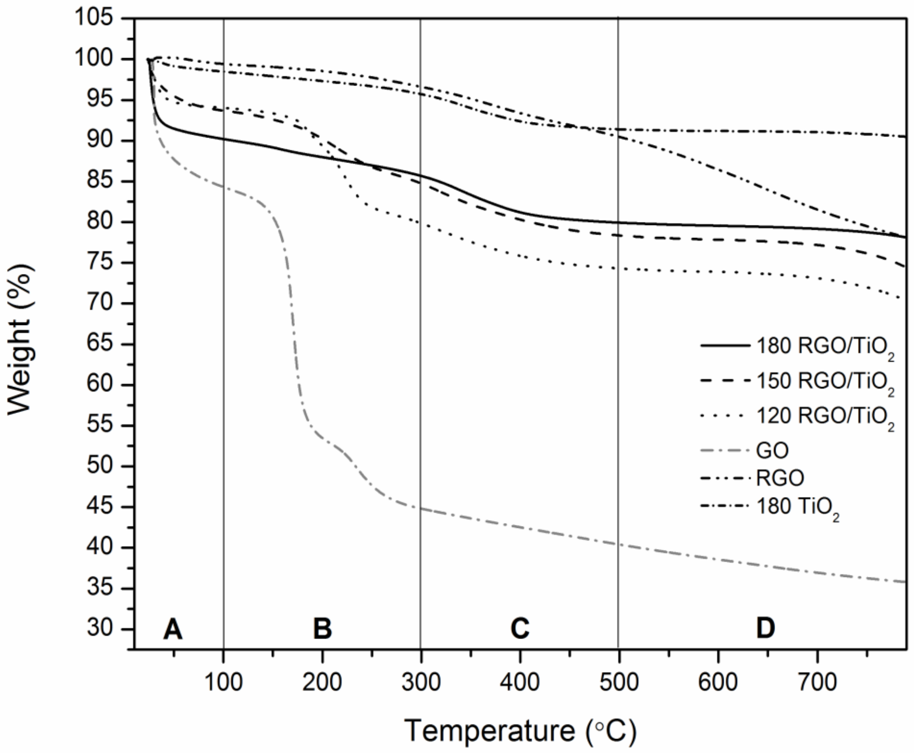

Figure 4.8: TGA curves of GO, RGO, TiO_2 and RGO/TiO_2.

The successful decoration of TiO_2 nanoparticles on RGO is also reflected in the thermogravimetric analysis (TGA) curves [**Figure 4.8**]. The TGA curves for all the nanocomposites had four distinct regions (A, B, C, and D). In the region up to 100 ℃

(region A), the sample weight loss was caused by the resorption of physisorbed water. Between 150 ℃–300 ℃ (region B), the weight loss was a result of the decomposition of labile oxygen groups like carboxylate, anhydride, or lactone groups. Region C occurred between 300 ℃–500 ℃ and was associated with the removal of more stable oxygen groups such as phenol, carbonyl, and quinine. Above 500 ℃ (region D), high temperature pyrolysis of carbon skeleton occurred (J. F. Shen et al., 2011). GO displayed a drastic weight loss (40% of its original weight) in region B caused by the decomposition of labile oxygen-containing functional groups such as epoxy and hydroxyl groups. There was a similar loss of weight for the RGO, but the change was not so big. This result indicates that most of the GO oxygen-containing functional groups were reduced during the hydrothermal process, thereby increasing the thermal stability of the RGO (J. F. Shen et al., 2011). For the nanocomposites in region B, the percentage of weight loss decreased with hydrothermal temperature. Specifically, the 120 RGO/TiO_2, 150 RGO/TiO_2, and 180 RGO/TiO_2 samples lost 14.1%, 7.9%, and 3.5% of their weight, respectively. This result indicates that the 180 RGO/TiO_2 sample had the least amount of labile oxygen-containing functional groups attached to the surface. It also further indicates that a low hydrothermal temperature (120 ℃) was unable to reduce the oxygenous groups of GO in the nanocomposites efficiently.

4.9 Schematic Formation Mechanism

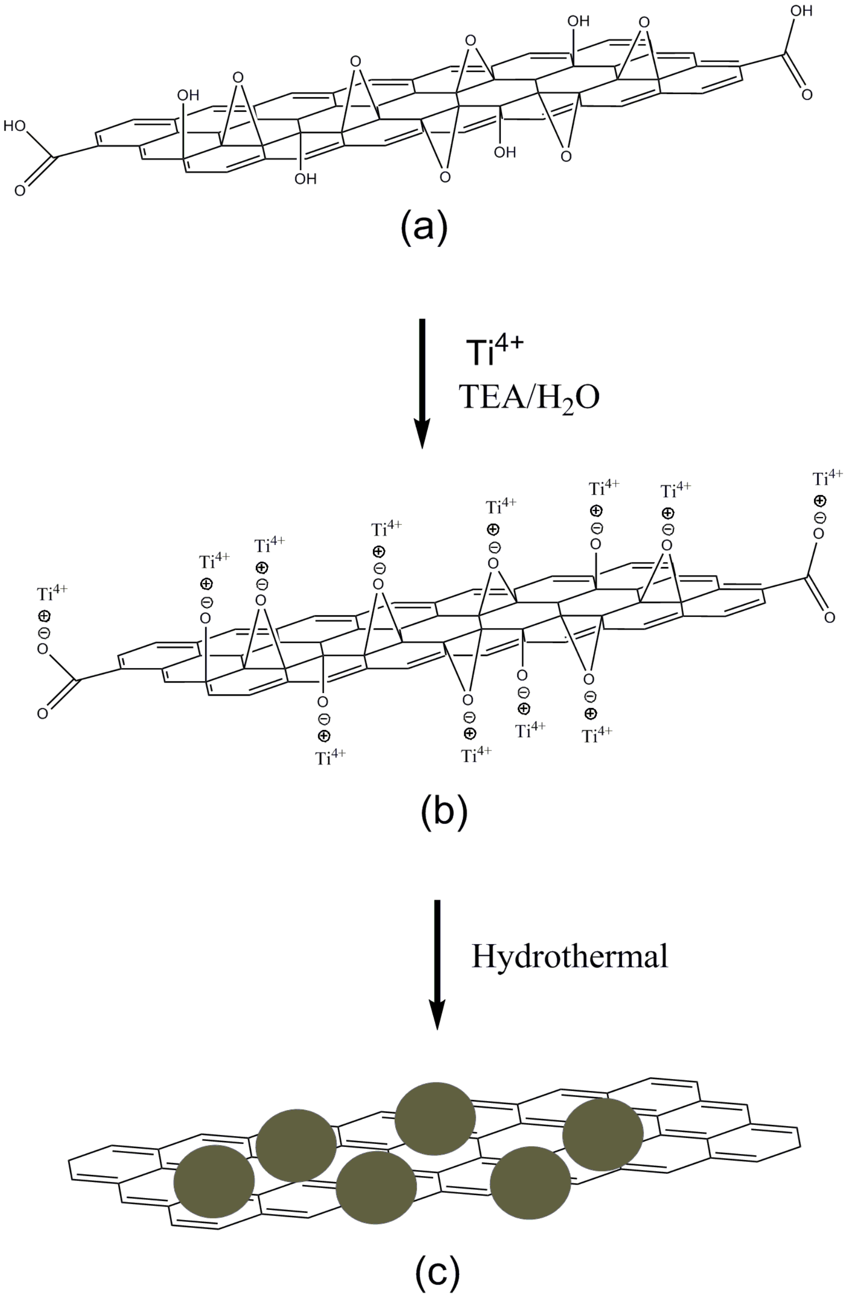

Figure 4.9: Schematic formation mechanism of RGO/TiO_2 nanocomposite. (**a**) GO, (**b**) electrostatic interaction between oxide functional groups of GO and Ti^{4+} in the presence of TEA and (**c**) graphene decorated with TiO_2 nanoparticles (filled circles) after the hydrothermal treatment.

A plausible schematic formation of RGO/TiO_2 is illustrated in **Figure 4.9**. GO was mixed with Ti^{4+} in the presence of TEA. This provided a platform for electrostatic interaction between the negatively-charged oxide functional groups of GO and the positively-charged Ti^{4+} [**Figure 4.9**(**b**)]. Nucleation occurred at the sites, which resulted in the growth of TiO_2 nanoparticles on the two-dimensional graphene nanosheets during the hydrothermal process [**Figure 4.9**(**c**)]. The narrow size distribution of the TiO_2 nanoparticles embedded on the graphene nanosheets may be due to the critical control of the TEA molecules. GO was reduced to graphene due to the simultaneous presence of Ti^{4+}, TEA, and hydrothermal treatment.

4.10 Electrochemical Performance

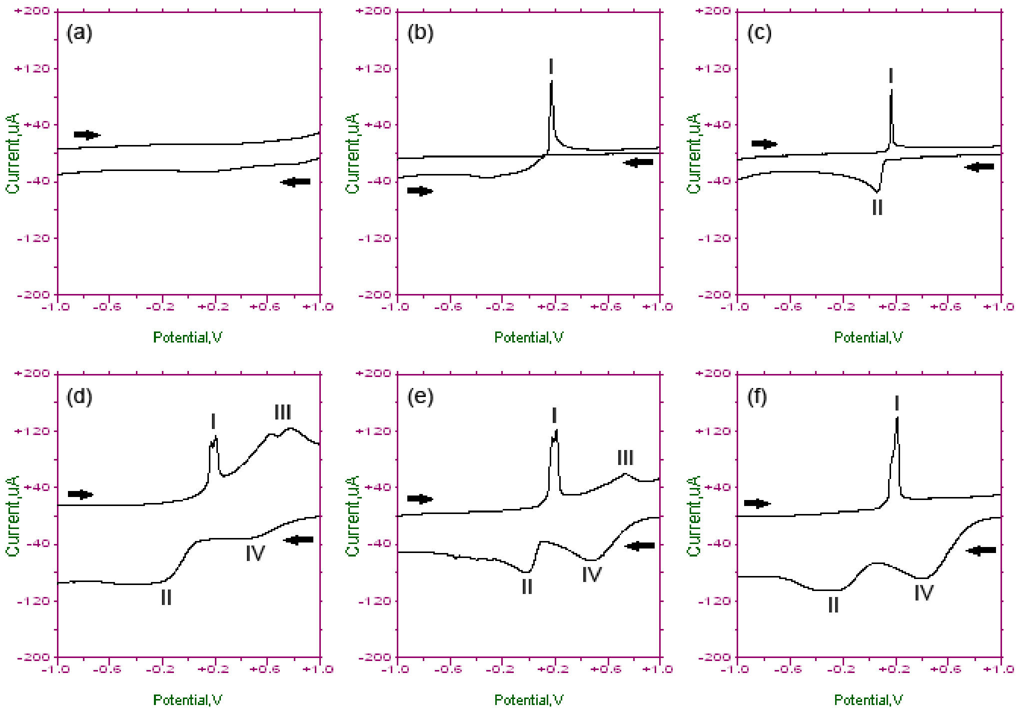

Figure 4.10: Electrochemical analysis of (**a**) bare GCE in KCl supporting electrolyte, (**b**) bare GCE, (**c**) RGO-modified GCE, (**d**) 150 RGO/TiO_2-modified GCE, (**e**) 180 RGO/TiO_2-modified GCE and, (**f**) 120 RGO/TiO_2-modified GCE in KCl supporting electrolyte and Hg^{2+} ionic solution.

Figure 4.10 displays the electrochemical performance of the samples examined by cyclic voltammetry with a scan rate of 50 mV s^{-1}. The background current behavior for bare GCE in KCl supporting electrolyte with no Hg ions was almost flat and there were no oxidizing and reducing reactions [**Figure 4.10(a**)]. On the other hand, the results for the bare GCE using the KCl electrolyte containing mercury (II) ions (Hg^{2+}) in KCl, resulted in a distinctive oxidizing peak current observed between +0.1 V and +0.2 V [peak I; **Figure 4.10**(**b**)]. The RGO modified GCE in KCl supporting electrolyte added with Hg^{2+} has an additional reductive peak between -0.2 and +0.2 V [peak II; **Figure 4.10**(**c**)]. The entire hydrothermally prepared RGO/TiO_2 modified GCE had improved electrochemical performance, signifying an increase in sensitivity to the detection of Hg^{2+} [**Figure 4.10**(**d**)-(**f**)]. The 150 RGO/TiO_2-modified GCE exhibited additional oxidization reactions between +0.4 and +1.0 V [peak III] of all the samples. There are two distinct peaks. This oxidization reaction is in addition to the oxidative [peak I] seen in the RGO GCE [**Figure 4.10**(**d**)]. The sample also has a trough-like reductive peak [peak II], which is shifted to a lower voltage by ~0.2 V, and there is a reductive shoulder between +0.2 and +0.8 V [peak IV]. 180 RGO/TiO_2-modified GCE also shows similar oxidative [peaks I and III], and reductive [peaks II and IV; **Figure 4.10**(**e**)]. For 120 RGO/TiO_2-modified GCE, the two reductive [peak II – which shifted by about 0.2 V to the left – and peak IV] were enhanced by approximately 40 µA [**Figure 4.10**(**f**)] when compared to 180 RGO/TiO_2-modified GCE. The peaks are most likely to arise through the stepwise reduction of $Hg^{2+} + e^{-} \leftrightarrows Hg^{+}$ and $Hg^{+} + e^{-} \leftrightarrows Hg^{0}$. The oxidative peak [peak II] that was so pronounced in 150 RGO/TiO_2-modified GCE [**Figure 4.10**(**d**)] and 180 RGO/TiO_2-modified GCE [**Figure 4.10**(**e**)] was missing in 120 RGO/TiO_2-modified GCE. Among all the samples, 120 RGO/TiO_2-modified GCE possessed the best reducing reaction, which possibly makes it an efficient redox-recyclable material for the extraction of heavy element ions from wastewater.

4.11 Photoluminescence Emission Spectrum

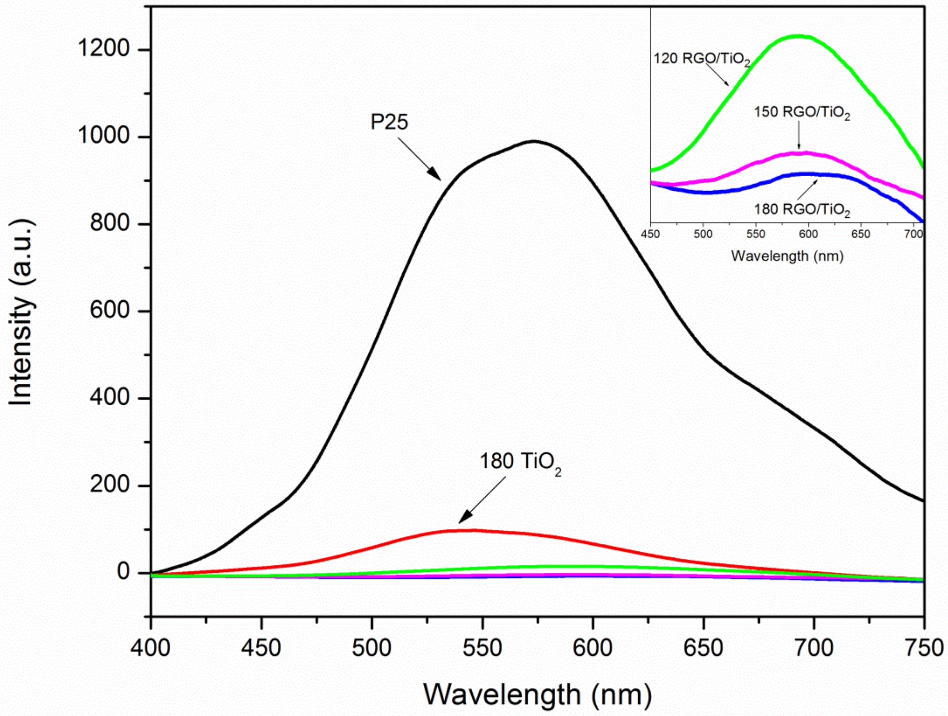

Figure 4.11: PL curves of P25, pure TiO_2, 120 RGO/TiO_2, 150 RGO/TiO_2, and 180 RGO/TiO_2. The inset is the amplificatory image of the area in the range of 450 to 710 nm of 120 RGO/TiO_2, 150 RGO/TiO_2, and 180 RGO/TiO_2.

The PL emission spectrum has been utilized extensively to study the surface structure and excited state of semiconductor (Yao, Li, Ciston, Lueptow, & Gray, 2008; Y. Yu et al., 2005). With electron-hole pair recombination after a photocatalyst is irradiated, the semiconductor emits photons, resulting in photoluminescence. This phenomenon is due to the reverse radiative deactivation from the excited-state of Ti species. **Figure 4.11** shows PL spectra of P25, pure TiO_2, and RGO/TiO_2 composites prepared at three different hydrothermal temperatures. P25 showed the broadest PL emission band, followed by 180 TiO_2. RGO/TiO_2 nanocomposites on the other hand, exhibited an abrupt emission quenching of TiO_2, representing that electrons transferred from excited TiO_2 to graphene. The inset is the amplificatory image of the area in the range of 400 to 710 nm, implicating that the quenching extent is in relation to the hydrothermal temperature used. Increasing the hydrothermal temperature from 120 ℃ to 180 ℃ decreases the emitting intensity gradually. This result indicates that the recombination of photoinduced electrons and holes was suppressed for RGO/TiO_2. It shows that a typical charge separation at the surface junction. Electrons tend to flow from the higher to lower Fermi level to adjust the Fermi energy levels (Woan et al., 2009). As the calculated work function of graphene is 4.42 eV and the conduction band position of anatase is about -4.21 eV (Czerw et al., 2002) with a bandgap of about 3.2 eV (using vacuum level as a reference) (Y Xu & Schoonen, 2000), graphene can accept the photoexcited electrons from TiO_2, thus hinders the electron-hole recombination. It has been reported that heating treatment leads to the formation of titanium-carbon (Ti-C) bonds between graphene and TiO_2 (Akhavan et al., 2010; Akhavan & Ghaderi, 2009). Hence, increasing the reaction temperature promotes the bonding of TiO_2 on graphene with Ti-C bond, leading to better adhesion. Better linkage between the two materials must facilitate the electrons transfer, causing an abatement of emission.

4.12 Photocatalytic Measurements

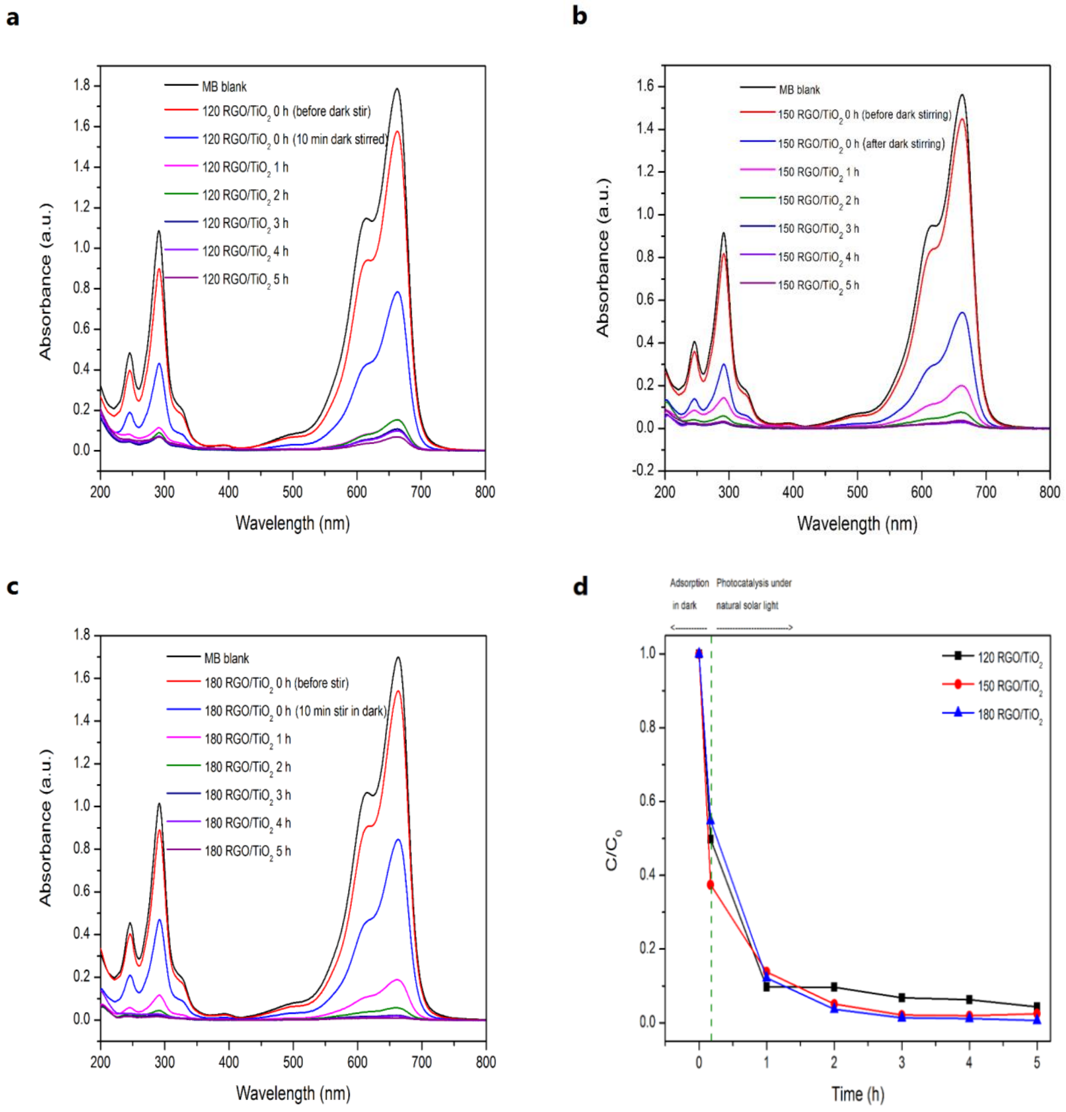

Figure 4.12: UV-Vis absorption spectra showing the degradation of MB by (**a**) 120 RGO/TiO_2 (**b**) 150 RGO/TiO_2, and (**c**) 180 RGO/TiO_2 with one hour interval. **Figure** (**d**) First cycle of MB photodegradation by 120 RGO/TiO_2, 150 RGO/TiO_2, and 180 RGO/TiO_2 with reaction time of 5 h under irradiation of 120 µW/cm^2/nm natural solar light intensity.

To compare the photocataytic activities of the three RGO/TiO_2 nanocomposites with different reaction times, a series of photodegradation experiments were carried out by using MB as a model pollutant under natural solar light with 120 µW/cm^2/nm sunlight intensity. The concentration of MB (C) is proportional to the maximum absorbance at 663 nm (A). Therefore, we analyzed the change of concentration (C/C_0) from the variation of absorbance (A/A_0), where C_0 and A_0 are the initial concentration and absorbance of MB respectively. In **Figure 4.12** (**d**), the RGO/TiO_2 photocatalysts captured about half of the amount of the MB molecules (5 mg L^{-1}) from solution after 10 min stirring in the dark. All the three nanocomposites show great adsorptivity to MB molecules, about eight times more powerful than P25 and pure TiO_2. The adsorption was proposed to be noncovalent and driven by the π-π stacking between MB and aromatic regions of graphene, which was similar to the conjugation between aromatic molecules and CNT (Z. Liu, Robinson, Sun, & Dai, 2008; H. Zhang et al., 2010). Among the three samples, the adsorption in the darkness exhibited an increasing trend in the order of 180 RGO/TiO_2, 120 RGO/TiO_2, and 150 RGO/TiO_2.

Furthermore, the UV-Vis absorption spectra [**Figure 4.12** (**d**)] show the absorbance peaks of MB for all samples decrease with the increase of reaction time. 150 RGO/TiO_2 and 180 RGO/TiO_2 displayed higher photocatalytic activity than 120 RGO/TiO_2. Under natural solar light irradiation, about 80% of the initial dyes were decomposed by all three RGO/TiO_2 after 1 h. After 3 hours of irradiation, the concentration of MB in solution dropped near to zero for 150 RGO/TiO_2 and 180 RGO/TiO_2. On the other hand, 120 RGO/TiO_2 showed a rather slow photocatalytic activity in which extra two hours were needed for the concentration of MB in solution to decline near to zero. The enhanced photocatalytic activity results from the uniform distribution of TiO_2 nanoparticles and the unique properties of graphene. Graphene acts as an electron-acceptor material by hindering the electron-hole pair recombination efficiently. It also behaves as a photosensibilizer by enhancing the utilization of visible light in photocatalysis. The photodegradation of MB by 120 RGO/TiO_2 seems to be unstable and lower than the 150 and 180 RGO/TiO_2, which may be attributed to the poor binding between graphene and TiO_2.

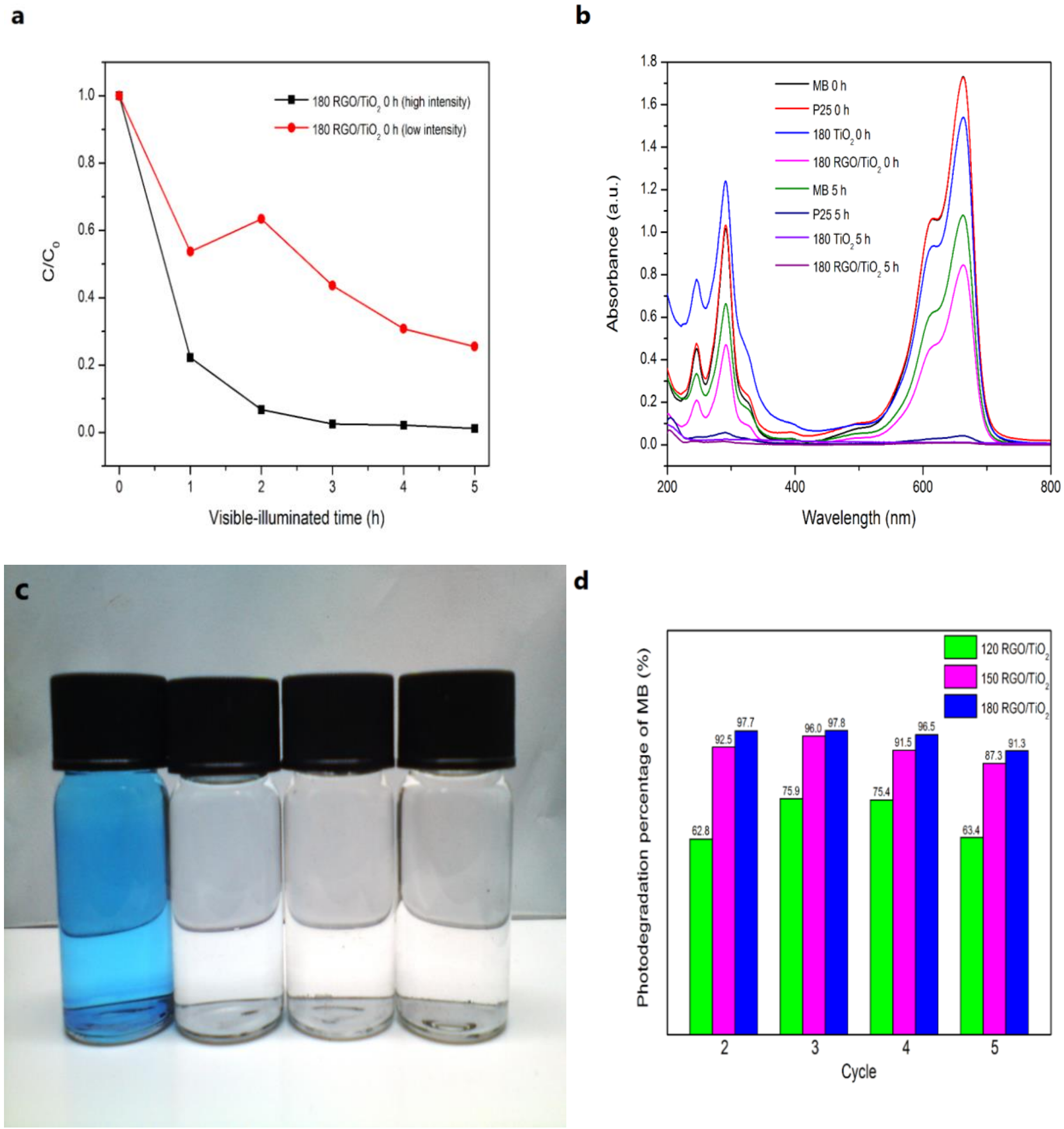

Figure 4.13: UV-Vis absorption spectra showing the degradation of MB by (**a**) 180 RGO/TiO_2 under different sun intensity (low = 15 μW/cm^2/nm and high = 120 μW/cm^2/nm), (**b**) different photocatalysts; P25, TiO_2, and 180 RGO/TiO_2. **Figure** (**c**) Pictures of the corresponding MB solution of P25, TiO_2, and 180 RGO/TiO_2 after 5h irradiation of natural sunlight. **Figure** (**d**) Cycling runs in the photodegradation of MB in the presence of 120, 150, and 180 RGO/TiO_2 under natural sunlight.

The photocatalytic test had also been carried out under both low (15 μW/cm^2/nm) and high (120 μW/cm^2/nm) intensity of sunlight irradiation [**Figure 4.13** (**a**)]. The photocatalytic process under low sunlight intensity irradiation was unstable and even after five hours of irradiation, there was about 25.5% of MB molecules not being degraded. The results of the high intensity sunlight irradiation on the other hand, showed that the degradation was stable and five hours of irradiation had successfully degraded 98.8% of MB. The “stable’ term here means that the the MB concentration was continuously in a decreasing trend throughout the entire photocatalysis process. The “unstable” term, on the other hand, indicates that the concentration of MB is fluctuating in up and down trend. Hence, we can say that photodegradation process had taken place and the decline in absorbance value was not merely due to adsorption of MB molecules on the catalyst surface. Besides that, it also indicates that photocatalytic process is dependent on the sunlight intensity.

From the above results, we can see that photocatalytic efficiency is affected by several factors, namely the method used, the presence of graphene, and the reaction temperature. Anatase crystalline TiO_2 nanoparticles prepared by hydrothermal approach with the addition of TEA increased the photocatalytic activity by facilitating the access of MB molecules to the reactive sites of TiO_2. Therefore, a higher photodegradation of MB was observed for 180 TiO_2 as compared to P25. On the other hand, the presence of graphene in the composites acts as an electron transfer channel to hinder the recombination of the photo-generated electron holes, leading to improved photo-conversion efficiency (D. H. Wang et al., 2009; X. Y. Zhang, Li, & Cui, 2009). Higher hydrothermal temperature produces RGO/TiO_2 nanocomposites with narrower size distribution, more crystallized, round shape, and homogeneous particles. As heating treatment leads to the formation of Ti-C bonds between graphene and TiO_2 (Akhavan & Ghaderi, 2009), increasing the reaction temperature also promotes the bonding of TiO_2 on graphene with Ti-C bond, leading to better adhesion.

Besides, during the photocatalytic activity of pure TiO_2 under sunlight irradiation, the reduced graphene oxide was able to act as electron acceptors to effectively reduce the rate of recombination of the photoexcited pairs and therefore increase the quantum efficiency of the photocatalytic process, as previously indicated by William et al. (Williams et al., 2008). In this regard, we have shown that higher hydrothermal temperature gives higher degree of reduction of the graphene oxide. The more reduced graphene oxide has better conductivity, causing greater accumulation of the photoexcited electrons on it. This then results in higher photocatalytic performance under solar light irradiation, which is in agreement with the reports of Akhavan et al (Akhavan & Ghaderi, 2009).

The durability test of the RGO/TiO_2 catalyst for the degradation of MB under natural solar light was also checked. The photodecomposition of MB was monitored for five consecutive cycles, each for five hours. After each cycle, RGO/TiO_2 was centrifuged and recovered. Fresh MB was then added for the next cycle. There was no significant decrease in photodegradation rate up to four consecutive cycles, indicating the good stability the prepared RGO/TiO_2 photocatalyst. The decline in photocatalytic activity was only displayed by RGO/TiO_2 at the fifth cycle.

CHAPTER 5 : CONCLUSION AND FUTURE WORKS

5.1 Conclusion

TiO_2 (with particle size ~20 nm) decorated RGO with high uniformity was successfully synthesized via a simple, single stage hydrothermal process using TEA as the co-reducing agent and capping agent. The TiO_2 nanoparticles are formed at the same time as the GO is reduced to graphene. The TEA used in the process has two roles. It acts as a reducing agent for the GO as well as capping agent allowing the formation of TiO_2 nanoparticles with a narrow size distribution. This method does not require ultrasonication to obtain a well-dispersed suspension of GO and TiO_2. This simplified method has great advantage over other published methods of producing graphene-decorated TiO_2 nanoparticles. The method allows control of the particle size distribution through alteration of the hydrothermal temperature.

UV-Visible absorption spectroscopy results showed that the GO reduction degree was higher as the hydrothermal temperature increased. This was deduced by the right-shifting of the peak at 227 nm to 256 nm (for the 150 RGO/TiO_2 and 180 RGO/TiO_2 samples), which represents the partial restoration of pi-conjugation network. The G and D bands in the Raman spectrum of RGO/TiO_2 were similar to those of RGO, showing that the introduction of TiO_2 nanoparticles did not affect the structure of the RGO sheets. Hence, this means that restacking of the RGO sheets did not take place. As compared with GO, the RGO/TiO_2 nanocomposite displays an increased D/G intensity ratio, suggesting a decrease in the average size of the sp^2 domains upon reduction of the exfoliated GO. The presence of Ti-C bond as indicated by the XPS results implies that hydrothermal process is capable of forming a chemical bond between the carbon of the RGO and the titanium of the TiO_2 nanoparticles. In addition, hydrothermal temperature also has an effect in the crystallization of the TiO_2 nanoparticles. The XRD results showed that the FWHM value decreased from 120 RGO/TiO_2 to 180 RGO/TiO_2, confirming that higher hydrothermal temperature produced greater TiO_2 crystallization.

Besides that, the TEM images of the samples exhibited uniform distribution of TiO_2 nanoparticles on the basal plane of RGO nanosheets. The size distribution of the TiO_2 nanoparticles was narrower when the hydrothermal temperature increased. The nanoparticles appeared to be more crystallized, round shaped, and homogeneous in the 180 RGO/TiO_2 sample as compared to the less crystallized, amorphous, and heterogeneous in the 120 RGO/TiO_2 sample. When most of the GO oxygen-containing functional groups were being reduced in the hydrothermal reaction, the thermal stability of the RGO will then be increased, as shown by the TGA curves. The PL spectra displayed that by increasing the hydrothermal temperature from 120 ℃ to 180 ℃, the emitting intensity declined gradually, indicating that the recombination of photoinduced electrons and holes was suppressed for the RGO/TiO_2 nanocomposites. This further implied that RGO was able to accept the photoexcited electrons from TiO_2, thus hindered the electron-holes recombination.

All of the above properties enabled the nanocomposites to be tailored to a specific application, as demonstrated by the detection of mercury ions in the electrochemical cell where the redox peaks in the cyclic voltammetric depended on the hydrothermal reactor temperature [(**Chapter 4.10**)]. The entire hydrothermally prepared RGO/TiO_2-modified GCE had improved electrochemical performance, signifying an increase in sensitivity to the detection of mercury ions, suggesting the possibility using them for detection of the heavy metal. Among all the samples, the 120 RGO/TiO_2-modified GCE possessed the best reducing reaction, which possibly makes it an efficient redox-recyclable material for the extraction of heavy element ions from wastewater.

Moreover, the RGO/TiO_2 nanocomposites prepared had a great potential to be applied as high performance photocatalysts. The nanocomposites produced possessed great adsorptivity of dyes, low electron-hole pair recombination, high recyclability, narrow size distribution, and uniformly distributed TiO_2 nanoparticles. On the basis of these advantages, RGO/TiO_2 demonstrated significant advancement over bare P25 and pure TiO_2 in the photodegradation of MB dye under natural sunlight. Reaction temperature plays a crucial role in controlling the structure and properties of the RGO/TiO_2 composites. Increasing the hydrothermal temperature allows the formation of more homogeneous products with more quenching of photoluminescence. Thus, 180 RGO/TiO_2 gave the best performance in the degradation of methylene blue dye.

5.2 *Future Works*

Having completed this thesis, it should be noted that there are still ample opportunities for further research in this exciting field of study. The results of this work can be applied by the researchers. TiO_2 nanoparticles had been successfully decorated on the basal plane of the RGO sheets. The successful synthesis of the RGO/TiO_2 nanocomposites via hydrothermal process is encouraging to extend this method for synthesizing other TiO_2 nanostructures, such as nanoflowers, nanowires, and etc.

Moreover, this synthesis method can be easily extended to the fabrication of other classes of graphene based nanocomposites. The graphene based nanocomposites can then be evaluated for their compatibility to be applied in various applications such as photocatalysis, photovoltaic, biomedical applications, functionalized hybrid materials, sensors, and etcetera.

Hence, this work is anticipated to open a new possibility in the investigation of TiO_2-carbon or graphene based nanocomposites and promote their practical application in addressing various environmental issues.

REFERENCES

Acosta-Torres, L. S., #243, pez-Mar, #237, n, L. M., #250, . . . o, V. M. (2011). Biocompatible Metal-Oxide Nanoparticles: Nanotechnology Improvement of Conventional Prosthetic Acrylic Resins. *Journal of Nanomaterials, 2011*. doi: 10.1155/2011/941561

Adalsteinsson, T. (2008). Principles for Thermogravimetric Analysis (TGA). Retrieved June 08, 2013, from http://webpages.scu.edu/ftp/adalsteinsson/GroupSite/Methods/DSCinfo/page30/page30.html

Akhavan, O., Abdolahad, M., Abdi, Y., & Mohajerzadeh, S. (2009). Synthesis of titania/carbon nanotube heterojunction arrays for photoinactivation of E. coli in visible light irradiation. *Carbon, 47*(14), 3280-3287. doi: 10.1016/j.carbon.2009.07.046

Akhavan, O., Azimirad, R., Safa, S., & Larijani, M. M. (2010). Visible light photo-induced antibacterial activity of CNT-doped TiO2 thin films with various CNT contents. *J Mater Chem, 20*(35), 7386-7392.

Akhavan, O., & Ghaderi, E. (2009). Photocatalytic Reduction of Graphene Oxide Nanosheets on TiO2 Thin Film for Photoinactivation of Bacteria in Solar Light Irradiation. *Journal of Physical Chemistry C, 113*(47), 20214-20220. doi: 10.1021/jp906325q

Aleiner, I. L., & Efetov, K. B. (2006). Effect of disorder on transport in graphene. *Physical Review Letters, 97*, 236801-236804.

Ali, M. (1999). 3.0 General Experimental Techniques. Retrieved June 08, 2013, from http://www.study-on-line.co.uk/whoami/thesis/chap3.html

Andrei, M. (2011). New spin makes graphene magnetic. Retrieved June 08, 2013, from http://www.zmescience.com/science/physics/graphene-transistor-16042011/

Balandin, A. A., Ghosh, S., Bao, W., Calizo, I., Teweldebrhan, D., Miao, F., & Lau, C. N. (2008). Superior Thermal Conductivity of Single-Layer Graphene. *Nano Letters, 8*(3), 902-907. doi: 10.1021/nl0731872

Bekyarova, E., Itkis, M. E., Ramesh, P., Berger, C., Sprinkle, M., de Heer, W. A., & Haddon, R. C. (2009). Chemical Modifications of Epitaxial Graphene: Spontaneous Grafting of Aryl Groups. *Journal of the American Chemical Society, 131*, 1336.

Berger, C., Song, Z., Li, X., Wu, X., Brown, N., Naud, C., . . . de Heer, W. A. (2006). Electronic Confinement and Coherence in Patterned Epitaxial Graphene. *Science, 312*(5777), 1191-1196. doi: 10.1126/science.1125925

Bessekhouad, Y., Robert, D., & Weber, J. V. (2004). Bi2S3/TiO2 and CdS/TiO2 heterojunctions as an available configuration for photocatalytic degradation of organic pollutant. *Journal of Photochemistry and Photobiology A: Chemistry, 163*(3), 569-580. doi: 10.1016/j.jphotochem.2004.02.006

Bond, A. M., & Marken, F. (1994). Mechanistic aspects of the electron and ion transport processes across the electrode solid solvent (electrolyte) interface of microcrystalline decamethylferrocene attached mechanically to a graphite electrode. *Journal of Electroanalytical Chemistry, 372*(1-2), 125-135. doi: 10.1016/0022-0728(93)03257-p

Byrappa, K., & Yoshimura, M. (2001). Handbook of Hydrothermal Technology. *William Andrew Publishing, New York*.

Cao, H., Zhu, Y., Tan, X., Kang, H., Yang, X., & Li, C. (2010). Fabrication of TiO2/CdS composite fiber via an electrospinning method. *New Journal of Chemistry, 34*(6), 1116-1119.

Carp, O., Huisman, C. L., & Reller, A. (2004). Photoinduced reactivity of titanium dioxide. *Progress in Solid State Chemistry, 32*(1–2), 33-177. doi: 10.1016/j.progsolidstchem.2004.08.001

Chang BYS, Huang NM, An'amt MN, Marlinda AR, Norazriena Y, Muhamad MR, . . . CH, C. (2012). Facile hydrothermal preparation of titanium dioxide decorated reduced graphene oxide nanocomposite. *International Journal of Nanomedicine, 7*(1), 3379-3387. doi: http://dx.doi.org/10.2147/IJNS28189

Chen, L.-C., Ho, Y.-C., Guo, W.-S., Huang, C.-M., & Pan, T.-C. (2009). Enhanced visible light-induced photoelectrocatalytic degradation of phenol by carbon nanotube-doped TiO2 electrodes. *Electrochimica Acta, 54*(15), 3884-3891. doi: 10.1016/j.electacta.2009.02.001

Chen, L., Tian, J., Qiu, H., Yin, Y., Wang, X., Dai, J., . . . Chu, L. (2009). Preparation of TiO2 nanofilm via sol-gel process and its photocatalytic activity for degradation of methyl orange. *Ceramics International, 35*(8), 3275-3280. doi: 10.1016/j.ceramint.2009.05.021

Chen, X., & Mao, S. S. (2007). Titanium Dioxide Nanomaterials: Synthesis, Properties, Modifications, and Applications. *Chemical Reviews, 107*(7), 2891-2959. doi: 10.1021/cr0500535

Chi-Hwan Han, Dae-Woong Hong, Sang-Do Han, Jihye Gwak, & Singh, K. C. (2007). Catalytic combustion type hydrogen gas sensor using TiO2 and UV-LED. *Sensors and Actuators B: Chemical, 125*, 224-228.

Coscia, U., Ambrosone, G., Lettieri, S., Maddalena, P., Rava, P., & Minarini, C. (2003). Power density effects on the growth of microcrystalline silicon–carbon alloys by PECVD. *Thin Solid Films, 427*(1–2), 284-288. doi: 10.1016/s0040-6090(02)01145-8

Courtney Payne, & Barron, A. R. (2010a). Raman and Surface-Enhanced Raman Spectroscopy. Retrieved June 08, 2013, from http://cnx.org/content/m34528/latest/

Courtney Payne, & Barron, A. R. (2010b). Surface-Enhanced Raman Spectroscopy for the Study of Surface Chemistry. Retrieved June 08, 2013, from http://cnx.org/content/m34522/latest/?collection=col10699/latest

Czerw, R., Foley, B., Tekleab, D., Rubio, A., Ajayan, P. M., & Carroll, D. L. (2002). Substrate-interface interactions between carbon nanotubes and the supporting substrate. *Physical Review B, 66*(3), 033408.

Desai, V. S., & Kowshik, M. (2009). Antimicrobial Activity of Titanium Dioxide Nanoparticles Synthesized by Sol-Gel Technique. *Research Journal of Microbiology, 4*, 97-103.

Dhas, V., Muduli, S., Agarkar, S., Rana, A., Hannoyer, B., Banerjee, R., & Ogale, S. (2011). Enhanced DSSC performance with high surface area thin anatase TiO(2) nanoleaves. *Solar Energy, 85*(6), 1213-1219. doi: 10.1016/j.solener.2011.02.029

Dios, A. C. d. (2000). Introduction to the U-2001 UV/Visible Spectrophotometer. Retrieved June 08, 2013, from http://bouman.chem.georgetown.edu/S00/handout/spectrometer.htm

DiVincenzo, D. P., & Mele, E. J. (1984). Self-consistent effective-mass theory for intralayer screening in graphite intercalation compounds. *Physical Review B, 29*(4), 1685-1694.

Dong, W., Sun, Y., Lee, C. W., Hua, W., Lu, X., Shi, Y., . . . Zhao, D. (2007). Controllable and Repeatable Synthesis of Thermally Stable Anatase

Nanocrystal−Silica Composites with Highly Ordered Hexagonal Mesostructures. *Journal of the American Chemical Society, 129*(45), 13894-13904. doi: 10.1021/ja073804o

Eder, D., & Windle, A. H. (2008). Carbon–Inorganic Hybrid Materials: The Carbon-Nanotube/TiO2 Interface. *Advanced Materials, 20*(9), 1787-1793. doi: 10.1002/adma.200702835

Eizenberg, M., & Blakely, J. M. (1979). Carbon monolayer phase condensation on Ni(111). *Surface Science, 82*(1), 228-236. doi: 10.1016/0039-6028(79)90330-3

Fan, W., Lai, Q., Zhang, Q., & Wang, Y. (2011). Nanocomposites of TiO2 and Reduced Graphene Oxide as Efficient Photocatalysts for Hydrogen Evolution. *The Journal of Physical Chemistry C, 115*(21), 10694-10701. doi: 10.1021/jp2008804

Fasolino, A., Los, J. H., & Katsnelson, M. I. (2007). Intrinsic ripples in graphene. *Nat Mater, 6*(11), 858-861.

Forbeaux, I., Themlin, J. M., & Debever, J. M. (1998). Heteroepitaxial graphite on 6H-SiC(0001): Interface formation through conduction-band electronic structure. *Physical Review B, 58*(24), 16396-16406.

Formenti, M., Juillet, F., Meriaudeau, P., & Teichner, S. J. (1971). Heterogeneous photocatalysis for partial oxidation of paraffins. *Chem. Technol., 1*, 680.

Fox, M. A., & Dulay, M. T. (1993). *Chem. Rev., 93*, 341.

Fujishima, A., & Honda, K. (1972). Electrochemical Photolysis of Water at a Semiconductor Electrode. *Nature, 238*(5358), 37-38.

Fujishima, A., Rao, T. N., & Tryk, D. A. (2000). Titanium dioxide photocatalysis. *Journal of Photochemistry and Photobiology C: Photochemistry Reviews, 1*(1), 1-21. doi: 10.1016/s1389-5567(00)00002-2

Gaya, U. I., & Abdullah, A. H. (2008). Heterogeneous photocatalytic degradation of organic contaminants over titanium dioxide: A review of fundamentals, progress and problems. *Journal of Photochemistry and Photobiology C: Photochemistry Reviews, 9*(1), 1-12. doi: 10.1016/j.jphotochemrev.2007.12.003

General: Characterization Techniques. (2012). Retrieved June 08, 2013, from http://nanocomposix.com/kb/general/characterization-techniques

Gerrity, D., H. Ryu, J. Crittenden, & Abbaszadegan, M. (2008). Photocatalytic inactivation of viruses using titanium dioxide nanoparticles and low-pressure UV light. *Journal of environmental science and health Part A, 43*, 1264-1270.

Gosser, D. K. (1993). *Cyclic Voltammetry: Simulation and Analysis of Reaction Mechanisms*. New York: Wiley-VCH.

Grätzel, M. (2001). Sol-Gel Processed TiO2 Films for Photovoltaic Applications. *Journal of Sol-Gel Science and Technology, 22*(1), 7-13. doi: 10.1023/a:1011273700573

Guo, J., Zhu, S., Chen, Z., Li, Y., Yu, Z., Liu, Q., . . . Zhang, D. (2011). Sonochemical synthesis of TiO2 nanoparticles on graphene for use as photocatalyst. *Ultrasonics Sonochemistry, 18*(5), 1082-1090. doi: 10.1016/j.ultsonch.2011.03.021

Helz, G. R., Zepp, R. G., & Crosby, D. G. (1994). *Aquatic and surface photochemistry*: Lewis Publishers.

Hernandez, Y., Nicolosi, V., Lotya, M., Blighe, F. M., Sun, Z., De, S., . . . Coleman, J. N. (2008). High-yield production of graphene by liquid-phase exfoliation of graphite. *Nat Nano, 3*(9), 563-568.

Herrmann, J.-M. (1999). Heterogeneous photocatalysis: fundamentals and applications to the removal of various types of aqueous pollutants. *Catalysis Today, 53*(1), 115-129. doi: 10.1016/s0920-5861(99)00107-8

Herrmann, J. M. (1999). Water treatment by heterogeneous photocatalysis. In F. Jansen & R. A. v. Santen (Eds.), *Environmental Catalysis, Catalytic Science Series* (Vol. 1, pp. 171-194). London: Imperial College Press.

Herrmann, J. M., Guillard, C., & Pichat, P. (1993). Heterogeneous photocatalysis : an emerging technology for water treatment. *Catalysis Today, 17*(1–2), 7-20. doi: 10.1016/0920-5861(93)80003-j

HN, L., NM, H., SS, L., I, H., & CH, C. (2011). Fabrication and characterization of graphene hydrogel via hydrothermal approach as a scaffold for preliminary study of cell growth. *International Journal of Nanomedicine, 6*(1), 1817-1823.

Hoffmann, M. R., Martin, S. T., Choi, W., & Bahnemann, D. W. (1995). Environmental Applications of Semiconductor Photocatalysis. *Chemical Reviews, 95*(1), 69-96. doi: 10.1021/cr00033a004

Huang NM, L. H., Chia CH, Yarmo MA, Muhamad MR. (2011). Simple room-temperature preparation of high-yield large-area graphene oxide. *Int J Nanomedicine, 6*(1), 3443-3448.

Huang, Z., P.C. Maness, D.M. Blake, E.J. Wolfrum, S.L. Smolinski, & Jacoby, W. A. (1999). Bactericidal mode of titanium dioxide photocatalysis. *Journal of Photochemistry and Photobiology A Chemistry, 130*, 163-170.

Inagaki, M., Kojin, F., Tryba, B., & Toyoda, M. (2005). Carbon Coated Anatase: The Role of the Carbon Layer for Photocatalytic Performance. *Carbon, 43*, 1652.

Inagaki, M., Nonaka, R., Tryba, B., & Morawski, A. W. (2006). Dependence of photocatalytic activity of anatase powders on their crystallinity. *Chemosphere, 64*(3), 437-445. doi: 10.1016/j.chemosphere.2005.11.052

Ishigami, M., Chen, J. H., Cullen, W. G., Fuhrer, M. S., & Williams, E. D. (2007). Atomic structure of graphene on SiO2. *Nano Letters, 7*, 1643-1648.

Jannik, C. M., Geim, A. K., Katsnelson, M. I., Novoselov, M. I., Booth, T. J., & Roth, S. (2007). The structure of suspended graphene sheets. *Nature, 446*, 60-63.

JGoodson. (2005). Retrieved Sept 30, 2012, from http://www.sinc.sunysb.edu/Stu/jgoodson/physics.html

Kim, K. S., Zhao, Y., Jang, H., Lee, S. Y., Kim, J. M., Kim, K. S., . . . Hong, B. H. (2009). Large-scale pattern growth of graphene films for stretchable transparent electrodes. *Nature, 457*(7230), 706-710.

Kim, S., Hwang, S.-J., & Choi, W. (2005). Visible Light Active Platinum-Ion-Doped TiO2 Photocatalyst. *The Journal of Physical Chemistry B, 109*(51), 24260-24267. doi: 10.1021/jp055278y

Kolen'ko, Y. V., Maximov, V. D., Garshev, A. V., Meskin, P. E., Oleynikov, N. N., & Churagulov, B. R. (2004). Hydrothermal synthesis of nanocrystalline and mesoporous titania from aqueous complex titanyl oxalate acid solutions. *Chemical Physics Letters, 388*(4-6), 411-415. doi: 10.1016/j.cplett.2004.03.042

Kominami, H., Murakami, S.-y., Kato, J.-i., Kera, Y., & Ohtani, B. (2002). Correlation between Some Physical Properties of Titanium Dioxide Particles and Their Photocatalytic Activity for Some Probe Reactions in Aqueous Systems. *The Journal of Physical Chemistry B, 106*(40), 10501-10507. doi: 10.1021/jp0147224

Konatham, D., & Striolo, A. (2008). Molecular design of stable graphene nanosheets dispersions. *Nano Letters, 8*, 4630-4641.

Kong, B.-S., Geng, J., & Jung, H.-T. (2009). Layer-by-layer assembly of graphene and gold nanoparticles by vacuum filtration and spontaneous reduction of gold ions. *Chemical Communications*(16), 2174-2176.

Lachheb, H., Puzenat, E., Houas, A., Ksibi, M., Elaloui, E., Guillard, C., & Herrmann, J.-M. (2002). Photocatalytic degradation of various types of dyes (Alizarin S, Crocein Orange G, Methyl Red, Congo Red, Methylene Blue) in water by UV-irradiated titania. *Applied Catalysis B: Environmental, 39*(1), 75-90. doi: 10.1016/s0926-3373(02)00078-4

Lambert, T. N., Chavez, C. A., Hernandez-Sanchez, B., Lu, P., Bell, N. S., Ambrosini, A., . . . Huber, D. L. (2009). Synthesis and Characterization of Titania-Graphene Nanocomposites. *Journal of Physical Chemistry C, 113*(46), 19812-19823. doi: 10.1021/jp905456f

Lee, S., Cho, I.-S., Lee, J. H., Kim, D. H., Kim, D. W., Kim, J. Y., . . . Hong, K. S. (2010). Two-step sol-gel method-based TiO_2 nanoparticles with uniform morphology and size for efficient photo-energy conversion devices. *Chemistry of Materials, 22*, 1958-1965.

Legrini, O., Oliveros, E., & Braun, A. M. (1993). Photochemical processes for water treatment. *Chemical Reviews, 93*(2), 671-698. doi: 10.1021/cr00018a003

Li, D., Muller, M. B., Gilje, S., Kaner, R. B., & Wallace, G. G. (2008). Processable aqueous dispersions of graphene nanosheets. *Nat Nano, 3*(2), 101-105.

Li, F. B., & Li, X. Z. (2002). Photocatalytic properties of gold/gold ion-modified titanium dioxide for wastewater treatment. *Applied Catalysis A: General, 228*(1–2), 15-27. doi: 10.1016/s0926-860x(01)00953-x

Li, F. B., Li, X. Z., & Hou, M. F. (2004). Photocatalytic degradation of 2-mercaptobenzothiazole in aqueous La3+–TiO2 suspension for odor control. *Applied Catalysis B: Environmental, 48*(3), 185-194. doi: 10.1016/j.apcatb.2003.10.003

Li, Q., Mahendra, S., Lyon, D. Y., Brunet, L., Liga, M. V., Li, D., & Alvarez, P. J. J. (2008). Antimicrobial nanomaterials for water disinfection and microbial control: Potential applications and implications. *Water Research, 42*(18), 4591-4602. doi: 10.1016/j.watres.2008.08.015

Liang, Y. Y., Wang, H. L., Casalongue, H. S., Chen, Z., & Dai, H. J. (2010). TiO2 Nanocrystals Grown on Graphene as Advanced Photocatalytic Hybrid Materials. *Nano Research, 3*(10), 701-705. doi: 10.1007/s12274-010-0033-5

Lightcap, I. V., Kosel, T. H., & Kamat, P. V. (2010). Anchoring Semiconductor and Metal Nanoparticles on a Two-Dimensional Catalyst Mat. Storing and Shuttling Electrons with Reduced Graphene Oxide. *Nano Letters, 10*(2), 577-583. doi: 10.1021/nl9035109

Linsebigler, A. L., Lu, G., & Yates, J. T. (1995). Photocatalysis on TiO2 Surfaces: Principles, Mechanisms, and Selected Results. *Chemical Reviews, 95*(3), 735-758. doi: 10.1021/cr00035a013

Liu, G., Chen, Z., Dong, C., Zhao, Y., Li, F., Lu, G. Q., & Cheng, H.-M. (2006). Visible Light Photocatalyst: Iodine-Doped Mesoporous Titania with a Bicrystalline Framework. *The Journal of Physical Chemistry B, 110*(42), 20823-20828. doi: 10.1021/jp062946m

Liu, Y.-J., Wang, Z.-M., Aizawa, M., Peng, W.-Q., & Hirotsu, T. (2009). Nanoporous composite of carbon nanosheets and functional titania nanoparticles formed by reassembling of exfoliated graphite oxides with colloidal titania. *Materials Letters, 63*(2), 260-262. doi: 10.1016/j.matlet.2008.10.023

Liu, Z., Robinson, J. T., Sun, X. M., & Dai, H. J. (2008). *Journal of the American Chemical Society, 130*, 10876.

McAllister, M. J., Li, J. L., Adamson, D. H., Schniepp, H. C., Abdala, A. A., Liu, J., . . . Aksay, I. A. (2007). Single sheet functionalized graphene by oxidation and thermal expansion of graphite. *Chemistry of Materials, 19*(18), 4396-4404. doi: 10.1021/cm0630800

Meng, X. B., Geng, D. S., Liu, J. A., Li, R. Y., & Sun, X. L. (2011). Controllable synthesis of graphene-based titanium dioxide nanocomposites by atomic layer deposition. *Nanotechnology, 22*(16). doi: 10.1088/0957-4484/22/16/165602

Meyer, J. C., Geim, A. K., Katsnelson, M. I., Novoselov, K. S., Booth, T. J., & Roth, S. (2007). The structure of suspended graphene sheets. *Nature, 446*, 60-63.

Mills, A., & Le Hunte, S. (1997). An overview of semiconductor photocatalysis. *Journal of Photochemistry and Photobiology A: Chemistry, 108*(1), 1-35. doi: 10.1016/s1010-6030(97)00118-4

Mills, B. (2010). Titanium-dioxide-sample. Retrieved June 08, 2013, from http://commons.wikimedia.org/wiki/File:Titanium-dioxide-sample.jpg

Mitoraj, D., Janczyk, A., Strus, M., Kisch, H., Stochel, G., Heczko, P. B., & Macyk, W. (2007). Visible light inactivation of bacteria and fungi by modified titanium dioxide. *Photochemical & Photobiological Sciences, 6*(6), 642-648.

Mouras, S., Hamm, A., Djurado, D., & J.-C., C. (1987). Synthesis of first stage graphite intercalation compounds with fluorides. *Revue de chimie minérale, 24*, 572-582.

Muller, H. D., & Steinbach, F. (1970). Decomposition of Isopropyl Alcohol photosensitized by Zinc Oxide. *Nature, 225*(5234), 728-729.

Murugan, A. V., Muraliganth, T., & Manthiram, A. (2009). Rapid, Facile Microwave-Solvothermal Synthesis of Graphene Nanosheets and Their Polyaniline Nanocomposites for Energy Strorage. *Chemistry of Materials, 21*(21), 5004-5006. doi: 10.1021/cm902413c

Nair, R. R., Blake, P., Grigorenko, A. N., Novoselov, K. S., Booth, T. J., Stauber, T., . . . Geim, A. K. (2008). Fine Structure Constant Defines Visual Transparency of Graphene. *Science, 320*, 1308.

Ni, M., Leung, M. K. H., Leung, D. Y. C., & Sumathy, K. (2007). A review and recent developments in photocatalytic water-splitting using for hydrogen production. *Renewable and Sustainable Energy Reviews, 11*(3), 401-425. doi: 10.1016/j.rser.2005.01.009

Ni, Z. H., Wang, H. M., Kasim, J., Fan, H. M., Yu, T., Wu, Y. H., . . . Shen, Z. X. (2007). Graphene thickness determination using reflection and contrast spectroscopy. *Nano Letters, 7*, 2758-2763.

Novoselov, K. S., Geim, A. K., Morozov, S. V., Jiang, D., Katsnelson, M. I., Griegorieva, I. V., . . . Firsov, A. A. (2005). Two-dimensional gas of massless Dirac fermions in graphene. *Nature, 438*, 197-200.

Novoselov, K. S., Geim, A. K., Morozov, S. V., Jiang, D., Zhang, Y., Dubonos, S. V., . . . Firsov, A. A. (2004). Electric field effect in atomically thin carbon films. *Science, 306*, 666-669.

O'Regan, B., & Gratzel, M. (1991). A low-cost, high-efficiency solar cell based on dye-sensitized colloidal TiO2 films. *Nature, 353*(6346), 737-740.

Ohno, T., Sarukawa, K., & Matsumura, M. (2002). Crystal faces of rutile and anatase TiO2 particles and their roles in photocatalytic reactions. *New Journal of Chemistry, 26*(9), 1167-1170.

Ollis, D. F., & Al-Ekabi, H. (1993). *Photocatalytic purification and treatment of water and air: proceedings of the 1st International Conference on TiO2 Photocatalytic Purification and Treatment of Water and Air, London, Ontario, Canada, 8-13 November, 1992*: Elsevier.

Paek, S.-M., Yoo, E., & Honma, I. (2008). Enhanced Cyclic Performance and Lithium Storage Capacity of SnO2/Graphene Nanoporous Electrodes with Three-Dimensionally Delaminated Flexible Structure. *Nano Letters, 9*(1), 72-75. doi: 10.1021/nl802484w

Paredes, J. I., Villar-Rodil, S., Martinez-Alonso, A., & Tascon, J. M. D. (2008). Graphene oxide dispersions in organic solvents. *Langmuir, 24*(null), 10560.

Park, J.-A., Moon, J., Lee, S.-J., Kim, S. H., Zyung, T., & Chu, H. Y. (2010). Structure and CO gas sensing properties of electrospun TiO2 nanofibers. *Materials Letters, 64*(3), 255-257. doi: 10.1016/j.matlet.2009.10.052

Pookmanee, P., Rujijanagul, G., Ananta, S., Heimann, R. B., & Phanichphant, S. (2004). Effect of sintering temperature on microstructure of hydrothermally prepared bismuth sodium titanate ceramics. *Journal of the European Ceramic Society, 24*(2), 517-520. doi: 10.1016/s0955-2219(03)00197-3

Powell, R. (2011). Photoluminescence. Retrieved June 08, 2013, from http://www2.warwick.ac.uk/fac/sci/physics/current/postgraduate/regs/mpags/ex5/techniques/optical/pl/

Rahman, M. R. M., Tajabadi, F., Shooshtari, L., & Taghavinia, N. (2011). Nanoparticulate Hollow TiO(2) Fibers as Light Scatterers in Dye-Sensitized Solar Cells: Layer-by-Layer Self-Assembly Parameters and Mechanism. *Chemphyschem, 12*(5), 966-973. doi: 10.1002/cphc.201000950

Reina, A., Jia, X., Ho, J., Nezich, D., Son, H., Bulovic, V., . . . Kong, J. (2008). Large Area, Few-Layer Graphene Films on Arbitrary Substrates by Chemical Vapor Deposition. *Nano Letters, 9*(1), 30-35. doi: 10.1021/nl801827v

Saito, R., Fujita, M., Dresselhaus, G., & Dresselhaus, M. S. (1992). Electronic structure of graphene tubules based on C60. *Physical Review B (Condensed Matter), 46*(3), 1804-1811.

Sato, S., & White, J. M. (1980). Photodecomposition of water over Pt/TiO2 catalysts. *Chemical Physics Letters*, *72*(1), 83-86. doi: 10.1016/0009-2614(80)80246-6

Schedin, F., Geim, A. K., Morozov, S. V., Hill, E. W., Blake, P., Katsnelson, M. I., & Novoselov, K. S. (2007). Detection of individual gas molecules adsorbed on graphene. *Nature Materials, 6*, 652-655.

Scheuermann, G. M., Rumi, L., Steurer, P., Bannwarth, W., & Mulhaupt, R. (2009). Palladium nanoparticles on graphite oxide and its functionalized graphene derivatives as highly active catalysts for the Suzuki-Miyaura coupling reaction. *Journal of the American Chemical Society*, *131*, 8262-8270.

Schiavello, M. (1988). *Photocatalysis and Environment: Trends and Applications*: Springer.

Schniepp, H. C., Li, J.-L., McAllister, M. J., Sai, H., Herrera-Alonso, M., Adamson, D. H., . . . Aksay, I. A. (2006). Functionalized Single Graphene Sheets Derived from Splitting Graphite Oxide. *The Journal of Physical Chemistry B, 110*(17), 8535-8539. doi: 10.1021/jp060936f

Sclafani, A., Palmisano, L., & Schiavello, M. (1990). Influence of the preparation methods of titanium dioxide on the photocatalytic degradation of phenol in aqueous dispersion. *The Journal of Physical Chemistry*, *94*(2), 829-832. doi: 10.1021/j100365a058

Scolan, E., & Sanchez, C. (1998). Synthesis and Characterization of Surface-Protected Nanocrystalline Titania Particles. *Chemistry of Materials, 10*(10), 3217-3223. doi: 10.1021/cm980322q

Seery, M. (2009). Metal Oxide Photocatalysis. Retrieved June 08, 2013, from http://photochemistryportal.net/home/index.php/2009/09/30/metal-oxide-photocatalysis/

Serpone, N., Lawless, D., Khairutdinov, R., & Pelizzetti, E. (1995). Subnanosecond Relaxation Dynamics in TiO2 Colloidal Sols (Particle Sizes Rp = 1.0-13.4 nm). Relevance to Heterogeneous Photocatalysis. *The Journal of Physical Chemistry, 99*(45), 16655-16661. doi: 10.1021/j100045a027

Serpone, N., & Pelizzetti, E. (1989). *Photocatalysis: fundamentals and applications*: Wiley.

Shanmugam, S., Gabashvili, A., Jacob, D. S., Yu, J. C., & Gedanken, A. (2006). Synthesis and Characterization of TiO2@C Core−Shell Composite Nanoparticles and Evaluation of Their Photocatalytic Activities. *Chemistry of Materials, 18*(9), 2275-2282. doi: 10.1021/cm052790n

Shen, J., Yan, B., Shi, M., Ma, H., Li, N., & Ye, M. (2011). One step hydrothermal synthesis of TiO2-reduced graphene oxide sheets. *Journal of Materials Chemistry, 21*(10), 3415-3421.

Shen, J. F., Hu, Y. Z., Shi, M., Li, N., Ma, H. W., & Ye, M. X. (2010). One Step Synthesis of Graphene Oxide-Magnetic Nanoparticle Composite. *Journal of Physical Chemistry C, 114*(3), 1498-1503. doi: 10.1021/jp909756r

Shen, J. F., Yan, B., Shi, M., Ma, H. W., Li, N., & Ye, M. X. (2011). One step hydrothermal synthesis of TiO2-reduced graphene oxide sheets. *Journal of Materials Chemistry, 21*(10), 3415-3421. doi: 10.1039/c0jm03542d

Sikong, L., Kongreong, B., Kantachote, D., & Sutthisripok, W. (2010). Photocatalytic Activity and Antibacterial Behavior of Fe³⁺-Doped TiO₂/SnO₂ Nanoparticles. *Energy Research Journal, 1*(2), 120-125. doi: 10.3844/erjsp.2010.120.125

Singh, V., Joung, D., Zhai, L., Das, S., Khondaker, S. I., & Seal, S. (2011). Graphene based materials: Past, present and future. *Progress in Materials Science, 56*(8), 1178-1271. doi: 10.1016/j.pmatsci.2011.03.003

So, W. W., Park, S. B., Kim, K. J., & Moon, S. J. (1997). Phase Transformation Behavior at Low Temperature in Hydrothermal Treatment of Stable and Unstable Titania Sol. *Journal of Colloid and Interface Science, 191*(2), 398-406. doi: 10.1006/jcis.1997.4969

Sobana, N., Muruganadham, M., & Swaminathan, M. (2006). Nano-Ag particles doped TiO2 for efficient photodegradation of Direct azo dyes. *Journal of Molecular Catalysis A: Chemical, 258*(1–2), 124-132. doi: 10.1016/j.molcata.2006.05.013

Srinivasan, C., & Somasundaram, N. (2003). Bactericidal and detoxification effects of irradiated semiconductor catalyst, TiO2. *Current Science, 85*, 1431-1438.

Stankovich, S., Dikin, D. A., Dommett, G. H. B., Kohlhaas, K. M., Zimney, E. J., Stach, E. A., . . . Ruoff, R. S. (2006). Graphene-based composite materials. *Nature, 442*(7100), 282-286.

Stankovich, S., Dikin, D. A., Piner, R. D., Kohlhaas, K. A., Kleinhammes, A., Jia, Y., . . . Ruoff, R. S. (2007). Synthesis of graphene-based nanosheets via chemical reduction of exfoliated graphite oxide. *Carbon, 45*(7), 1558-1565. doi: 10.1016/j.carbon.2007.02.034

Steinbach, F. (1969). Influence of Metal Support and Ultraviolet Irradiation on the Catalytic Activity of Nickel Oxide. *Nature, 221*(5181), 657-658.

Su, C., Hong, B. Y., & Tseng, C. M. (2004). Sol–gel preparation and photocatalysis of titanium dioxide. *Catalysis Today, 96*(3), 119-126. doi: 10.1016/j.cattod.2004.06.132

Su, C., Tseng, C. M., Chen, L. F., You, B. H., Hsu, B. C., & Chen, S. S. (2006). Sol–hydrothermal preparation and photocatalysis of titanium dioxide. *Thin Solid Films, 498*(1–2), 259-265.

Subramanian, V., Wolf, E. E., & Kamat, P. V. (2002). Influence of Metal/Metal Ion Concentration on the Photocatalytic Activity of TiO2−Au Composite Nanoparticles. *Langmuir, 19*(2), 469-474. doi: 10.1021/la026478t

Sutter, P. W., Flege, J.-I., & Sutter, E. A. (2008). Epitaxial graphene on ruthenium. *Nat Mater, 7*(5), 406-411.

Sykes, E. C. H. (2009). Surface assembly: graphene goes undercover. *Nature Chemistry, 1*, 175 - 176.

Tada, H., Yamamoto, M., & Ito, S. (1999). Promoting Effect of MgOx Submonolayer Coverage of TiO2 on the Photoinduced Oxidation of Anionic Surfactants. *Langmuir, 15*(11), 3699-3702. doi: 10.1021/la9816712

Torres, D. E. (2006). X-Ray Photoelectron Spectroscopy (XPS). Retrieved June 08, 2013, from https://docs.google.com/viewer?a=v&q=cache:VCHhmqNkOb8J:nanohub.org/resources/2110/download/x-ray%2520photoelectron%2520spectroscopy%2520(xps).ppt+&hl=en&gl=my&pid=bl&srcid=ADGEESi0tvbdpYlkx1G8g27zTiBM1ursMczhNRmAOfuL2b7c5ke5ektsu8yhPWZjyWAwRzlAWQ2-3ctj-G8DqzwMTBqAMdZ-NLg0naldXlXnfTgr4hfgIzwEoaAd-4mnZPv_D_F0t7B5&sig=AHIEtbS7jnDobMASjrLWJH3rit_-4W9nDA

Trapalis, C. C., Keivanidis, P., Kordas, G., Zaharescu, M., Crisan, M., Szatvanyi, A., & Gartner, M. (2003). TiO2(Fe3+) nanostructured thin films with antibacterial properties. *Thin Solid Films, 433*(1-2), 186-190. doi: 10.1016/s0040-6090(03)00331-6

Tuinstra, F., & Koenig, J. L. (1970). Raman Spectrum of Graphite. *The Journal of Chemical Physics, 53*(3), 1126-1130.

W.S. Hong, J.H. Park, & Han, G. Y. (2009). Optimization of conditions for hydrogen production from anodized TiO2 nanotube-based photoelectrochemical cells. *Journal of Nanoscience and Nanotechnology, 9*, 7293-7297.

Wallace, P. R. (1947). The Band Theory of Graphite. *Physical Review, 71*(9), 622-634.

Wang, C.-C., & Ying, J. Y. (1999). Sol−Gel Synthesis and Hydrothermal Processing of Anatase and Rutile Titania Nanocrystals. *Chemistry of Materials, 11*(11), 3113-3120. doi: 10.1021/cm990180f

Wang, D. H., Choi, D. W., Li, J., Yang, Z. G., Nie, Z. M., Kou, R., . . . Liu, J. (2009). Self-Assembled TiO2-Graphene Hybrid Nanostructures for Enhanced Li-Ion Insertion. *ACS Nano, 3*(4), 907-914. doi: 10.1021/nn900150y

Wang, G. (2007). Hydrothermal synthesis and photocatalytic activity of nanocrystalline TiO2 powders in ethanol-water mixed solutions. *Journal of Molecular Catalysis a-Chemical, 274*(1-2), 185-191. doi: 10.1016/j.molcata.2007.05.009

Wang, J., Hernandez, Y., Lotya, M., Coleman, J. N., & Blau, W. J. (2009). Broadband Nonlinear Optical Response of Graphene Dispersions. *Advanced Materials, 21*(23), 2430-2435.

Williams, G., Seger, B., & Kamat, P. V. (2008). TiO2-graphene nanocomposites. UV-assisted photocatalytic reduction of graphene oxide. *ACS Nano, 2*(7), 1487-1491. doi: 10.1021/nn800251f

Woan, K., Pyrgiotakis, G., & Sigmund, W. (2009). Photocatalytic Carbon-Nanotube–TiO2 Composites. *Advanced Materials, 21*(21), 2233-2239. doi: 10.1002/adma.200802738

Wu, M., Lin, G., Chen, D., Wang, G., He, D., Feng, S., & Xu, R. (2002). Sol-Hydrothermal Synthesis and Hydrothermally Structural Evolution of Nanocrystal Titanium Dioxide. *Chemistry of Materials, 14*(5), 1974-1980. doi: 10.1021/cm0102739

Wu, M., Long, J., Huang, A., Luo, Y., Feng, S., & Xu, R. (1999). Microemulsion-Mediated Hydrothermal Synthesis and Characterization of Nanosize Rutile and Anatase Particles. *Langmuir, 15*(26), 8822-8825. doi: 10.1021/la990514f

Xu, Y., Lv, K., Xiong, Z., Leng, W., Du, W., Liu, D., & Xue, X. (2007). Rate Enhancement and Rate Inhibition of Phenol Degradation over Irradiated Anatase and Rutile TiO2 on the Addition of NaF: New Insight into the Mechanism. *The Journal of Physical Chemistry C, 111*(51), 19024-19032. doi: 10.1021/jp076364w

Xu, Y. J., Zhuang, Y. B., & Fu, X. Z. (2010). New insight for enhanced photocatalytic activity of TiO2 by doping carbon nanotubes: A case study on degradation of benzene and methyl orange. *J. Phys. Chem. C, 114*(null), 2669-2676.

Xu, Z. W., Huang, Y. D., Min, C. Y., & Chen, L. (2010). Effect of gamma-ray radiation on the polyacrylonitrile based carbon fibers. *Radiation Physics and Chemistry, 79*(8), 839-843. doi: 10.1016/j.radphyschem.2010.03.002

Y Xu, & Schoonen, M. A. A. (2000). The absolute energy positions of conduction and valence bands of selected semiconducting minerals. *American Mineralogist, 85*(3-4), 543-556.

Yang, J., Mei, S., & Ferreira, J. M. F. (2001). Hydrothermal Synthesis of Nanosized Titania Powders: Influence of Tetraalkyl Ammonium Hydroxides on Particle Characteristics. *Journal of the American Ceramic Society, 84*(8), 1696-1702. doi: 10.1111/j.1151-2916.2001.tb00901.x

Yang, L., Luo, S., Liu, S., & Cai, Q. (2008). Graphitized Carbon Nanotubes Formed in TiO2 Nanotube Arrays: A Novel Functional Material with Tube-in-Tube Nanostructure. *The Journal of Physical Chemistry C, 112*(24), 8939-8943. doi: 10.1021/jp8020613

Yang, S., & Gao, L. (2005). Preparation of Titanium Dioxide Nanocrystallite with High Photocatalytic Activities. *Journal of the American Ceramic Society, 88*(4), 968-970. doi: 10.1111/j.1551-2916.2005.00151.x

Yang, X., Zhang, X., Ma, Y., Huang, Y., Wang, Y., & Chen, Y. (2009). Superparamagnetic graphene oxide-Fe_3O_4 nanoparticles hybrid for controlled targeted drug carriers. *Journal of Materials Chemistry, 19*, 2710-2714.

Yao, Y., Li, G. H., Ciston, S., Lueptow, R. M., & Gray, K. A. (2008). *Environ. Sci. Technol., 42*(null), 4952.

Yazawa, T., Machida, F., Kubo, N., & Jin, T. (2009). Photocatalytic activity of transparent porous glass supported TiO2. *Ceramics International, 35*(8), 3321-3325. doi: 10.1016/j.ceramint.2009.05.029

Yoo, E., Okata, T., Akita, T., Kohyama, M., Nakamura, J., & Honma, I. (2009). Enhanced electrocatalytic activity of Pt subnanoclusters on graphene nanosheet surface. *Nano Letters, 9*, 2255-2259.

Yu, H., Quan, X., Chen, S., & Zhao, H. (2007). TiO2−Multiwalled Carbon Nanotube Heterojunction Arrays and Their Charge Separation Capability. *The Journal of Physical Chemistry C, 111*(35), 12987-12991. doi: 10.1021/jp0728454

Yu, Y., Yu, J. C., Chan, C. Y., Che, Y. K., Zhao, J. C., Ding, L., . . . Wong, P. K. (2005). *Appl. Catal., B, 61*(null), 1.

Yuge, R., Zhang, M., Tomonari, M., Yoshitake, T., Iijima, S., & Yudasaka, M. (2008). Site identification of carboxyl groups on graphene edges with Pt derivatives. *ACS Nano, 2*, 1865-1870.

Zhang, A. P., & Sun, Y. P. (2004). Photocatalytic killing effect of TiO2 nanoparticles on Ls-174-t human carcinamo cells. *World J Gastroenterol, 10* 3191-3193.

Zhang, H., Lv, X. J., Li, Y. M., Wang, Y., & Li, J. H. (2010). P25-Graphene Composite as a High Performance Photocatalyst. *ACS Nano, 4*(1), 380-386. doi: 10.1021/nn901221k

Zhang, H. J., Xu, P. P., Du, G. D., Chen, Z. W., Oh, K., Pan, D. Y., & Jiao, Z. (2011). A facile one-step synthesis of TiO2/graphene composites for photodegradation of methyl orange. *Nano Research, 4*(3), 274-283. doi: 10.1007/s12274-010-0079-4

Zhang, L., Li, X., Huang, Y., Ma, Y. F., Wan, X. J., & Chen, Y. S. (2010). Controlled synthesis of few-layered graphene sheets on a large scale using chemical exfoliation. *Carbon, 48*(8), 2367-2371. doi: 10.1016/j.carbon.2010.02.035

Zhang, X. Y., Li, H. P., & Cui, X. L. (2009). Preparation and Photocatalytic Activity for Hydrogen Evolution of TiO2/Graphene Sheets Composite. *Chinese Journal of Inorganic Chemistry, 25*(11), 1903-1907.

Zhang, Y., Tan, Y.-W., Stormer, H. L., & Kim, P. (2005). Experimental observation of the quantum Hall effect and Berry's phase in graphene. *Nature, 438*, 201-204.

Zhang, Y. H., Tang, Z. R., Fu, X. Z., & Xu, Y. J. (2010). TiO2-Graphene Nanocomposites for Gas-Phase Photocatalytic Degradation of Volatile Aromatic Pollutant: Is TiO2-Graphene Truly Different from Other TiO2-Carbon Composite Materials? *ACS Nano, 4*(12), 7303-7314. doi: 10.1021/nn1024219

Zhao, J., Pei, S., Ren, W., Gao, L., & Cheng, H.-M. (2010). Efficient preparation of large-area graphene oxide sheets for transparent conductive films. *ACS Nano, 4*, 5245-5252.

Zhu, H. Y., Lan, Y., Gao, X. P., Ringer, S. P., Zheng, Z. F., Song, D. Y., & Zhao, J. C. (2005). Phase Transition between Nanostructures of Titanate and Titanium Dioxides via Simple Wet-Chemical Reactions. *Journal of the American Chemical Society, 127*(18), 6730-6736. doi: 10.1021/ja044689+

Zhu, J. (2008). Graphene production: New solutions to a new problem. *Nature Nanotechnology, 3*, 528-529.